2009

Exploration of Ternary Intermetallic Materials Using Tin and Gallium Flux

Edem Kodzo Okudzeto
Louisiana State University and Agricultural and Mechanical College

EXPLORATION OF TERNARY INTERMETALLIC MATERIALS USING TIN AND GALLIUM FLUX

A Dissertation

Submitted to the Graduate Faculty of the
Louisiana State University and
Agricultural and Mechanical College
in partial fulfillment of the
requirements for the degree of
Doctor of Philosophy
in
The Department of Chemistry

by
Edem K. Okudzeto
B.S., Morehouse College, 2004
December 2009

DEDICATION

I would like to dedicate this document to my cousin Guido Sohne, who passed away in May 2008. Two weeks shy of his thirty-firth birthday. You were a role model to me and helped spark my interest in science.

ACKNOWLEDGEMENTS

First and foremost I would like to thank God for his mercies and the blessings he has bestowed on me throughout my life especially during this period. I would never have made it without you.

I would like to thank my family especially my parents Sam and Priscilla Okudzeto for their prayers, money, guidance, wisdom and their words of encouragement. I would never have made it without your help. To my sibling Agnes, Sena, Kwaku, Eline and Esine thank you for being good role models for me. Without you I would never have done this. I thank you for listening to your little brother nag and your worlds of support. I would also like to thank my dear friend Mamle Quarmyne for all the support she has given me. She has stood by my side, encouraged me and made me believe in myself. Thank you!

To my Advisor professor Julia Y. Chan, I thank you for seeing the potential in me and helping me nurture it at all costs. Although we may have differed on several issues I thank you for the maturity and patience in all your endeavors. You have helped me in my professional development especially in my writing, for this I am extremely grateful. I thank you for the opportunities you put before me and the encouragement you gave me in pursuing them.

To the Chan group, we cried together, laughed together and shared so many things together. You have all helped in my professional and personal development. You became a second family to me. To Jung Y. Cho and Dixie P. Gautreaux, and we were the three musketries thanks for all the help. To my group sisters who have become real life sisters, Jasmine N. Millican and Kandace R. Thomas I thank you for opening your home to me and even sharing your mother with me. You made Baton Rouge feel like home, I always had a hot meal every holiday and for this I am very gratefully. To Evan L. Thomas you are a testament of what a true scientist should be, anything that you set your mind on you seemed to accomplish. I have the

uttermost respect for you. You helped me find my feet in the group and gently nudged me in the right direction.

To my committee members Professors George G. Stanley, Andrew W. Maverick, David P. Young, and John C. Flake I thank you for the bits of advise you have given me in this journey. I also thank you for helping me find the right path when I seem to stray.

A special thank you to my collaborators Professor David P. Young, Dr. Amar Karki, Dr. Monica Moldovan, Professor Rongying Jin, Professor Satoru Nakatsuji, Dr. Yusuke Nambu, Kentarou Kuga, Professor Fernande Grandjean and Professor Gary J. Long without you this work would never have been possible. I would also like to thank Dr. Frank Fronczek for sharing his knowledge on crystallography. You always had an open door policy and was easily approachable for this I am grateful.

TABLE OF CONTENTS

LIST OF TABLES

LIST OF FIGURES

ABSTRACT

The focus of this dissertation is the structure-property relationships of ternary intermetallic stannides and gallides. We are interested in these compounds because of the wide range of physical properties they possess. While investigating the *Ln*-Co-Sn system (*Ln* = lanthanide), we have synthesized single crystals that crystallize in the $Yb_3Rh_4Sn_{13}$, $Ho_7Co_6Sn_{23}$ and the $Tb_5Rh_6Sn_{18}$ structure types. We observe the formation of a particular structure type depending on the size of the lanthanide present. The aforementioned compounds all contain $CoSn_6$ trigonal prisms, which create voids occupied by *Ln* and Sn polyhedral units. We have also investigated the physical properties of these compounds to correlate the magnetic and transport phenomena observed. To determine the role of magnetic transition metals in lanthanide gallium compounds we have explored the *Ln*-Fe-Ga system and synthesized single crystals of Ln_4FeGa_{12} (*Ln* = Y, Tb, Dy, Ho and Er). The structure consists of iron octahedra and face sharing rare-earth cuboctahedra ($LnGa_3$). Magnetic susceptibility measurements performed on Yb_4FeGa_{12} show magnetic ordering in the Fe octahedra, a feature not observed in the isostructural analogues with Tb, Dy, Ho and Er. We have also synthesized single crystals of $YbCoGa_5$ using gallium flux. $YbCoGa_5$ adopts the $HoCoGa_5$ structure type which is made up of $CoGa_2$ and $YbGa_3$ structural units. The synthesis of $YbCoGa_5$ has filled a void in the $LnCoGa_5$ compounds by reported Yuri Grin. We have also studied the single crystal structures of $Ni_{1-x}Co_xGa_2S_4$ (x = 0, 0.2, 0.3, 0.5) and $Ni_{0.9}Mn_{0.1}Ga_2S_4$ to confirm composition and to study the role of doped Co and Mn in the two-dimensional antiferromagnet $NiGa_2S_4$.

CHAPTER 1. INTRODUCTION

1.1 Motivation

The focus of our research is to study structure-property relationships in highly correlated electron systems. These systems exhibit remarkable properties such as superconductivity, heavy fermion behavior, magnetoresistance and magnetic ordering. The study of such systems is motivated by the discovery of bulk superconductivity in the compound $CeCu_2Si_2$.[1] Before this discovery, it was assumed that superconductivity could not exist in compounds containing magnetic elements. However, the superconductivity in $CeCu_2Si_2$ is magnetically mediated and the "heavy mass" observed in this compound is responsible for this phenomenon. The coexistence of magnetism and superconductivity has also been studied in the heavy fermion compounds Ce_nMIn_{3n+2} (n = 1, 2, ∞; *M* = Co, Ir and Rh).[2-7] $CeCoIn_5$, $CeIrIn_5$ and Ce_2CoIn_8 superconduct under ambient pressure while the Rh analogues $CeRhIn_5$ and Ce_2RhIn_8 superconduct under external pressure.

Compounds that show heavy fermion behavior usually adopt specific structure types including $AuCu_3$, $BaAl_4$ $CaBe_2Ge_2$, $ThCr_2Si_2$, $HoCoGa_5$, Ho_2CoGa_8, $LaFe_4P_{12}$, and $Yb_3Rh_4Sn_{13}$ structure types.[8] $AuCu_3$ crystallizes in the cubic $Pm\bar{3}m$ space group and consists of $AuCu_3$ cuboctahedra. Several heavy fermion compounds also crystallize in variants of the $AuCu_3$ structure type.[8] Among these are the $HoCoGa_5$,[9] Ho_2CoGa_8,[9] $Yb_3Rh_4Sn_{13}$,[10] and the Y_4PdGa_{12}[11] structure types. In his article 'Fishing the Fermi Sea' Professor Canfield discusses targeting compounds that display exotic behavior by selecting specific elements to grow ternary phases.[12] For example, most heavy fermion compounds are formed by rare earth elements that display mixed valency such as Ce, Eu, Yb and U. Thus, by combining the synthesis of specific structure types with rare-earth elements that have a tendency to display mixed valency, it is possible to

narrow the field of discovery of new heavy fermions. Our expertise lies in the synthesis of high quality single crystals, which allow detailed studies of physical properties. We are interested in ternary intermetallic compounds that contain *Ln-M-X* (*Ln* = lanthanide, *M* = magnetic transition metals Fe and Co, and *X* = Sn or Ga). This study is motivated by the various *Ln-Ln*, *M-M* and *Ln-M* interactions observed in Co and Fe containing compounds.

1.2 Crystal Growth

One way of synthesizing intermetallic compounds is the use of an arc melter, radio frequency induction furnace, or traditional solid state routes. The products formed by these methods may be stable binaries or polycrystalline ternary compounds. The physical properties of some compounds are highly anisotropic ad hence the growth of single crystals are necessary for determination of intrinsic properties. There is a growing need for the synthesis of bulk single crystalline compounds that can be used in the discovery and applications of new materials.[13] Our groups' goal is to synthesize large singe crystals of ternary intermetallic compounds and to investigate their structure and physical properties. This is achieved by the use of molten metals (fluxes), which enables the diffusion of constituent elements and can result in the growth of large single crystals of intermetallic compounds.[14] In the syntheses reported in this dissertation, we employ Sn and Ga which melt at 504.9 K[15] and 302.8 K,[15] respectively. During our synthesis we weigh out constituent elements in specific stoichiometric amounts usually with the flux elements in excess. The elements are then placed in an alumina crucible, covered with quartz wool and sealed in an evacuated fused-silica tube. The sample is then placed in a furnace and treated with a specific heating profile. The sample is removed from the furnace above the melting point of the flux and inverted into a centrifuge. The quartz wool serves as a sieve and separates the molten flux from synthesized crystals. Excess flux is removed from the surface of the crystals

by etching in 6M HCl. Excess Ga flux can also be removed using hot water. Figure 1.1 shows photographs of some single crystals synthesized in our lab.

(a) (b) (c) (d)

Figure 1.1 Photographs of single crystals synthesized in our lab. (a) Tb_4FeGa_{12} (b) $Er_5Co_6Sn_{18}$ (c) $Gd_3Co_4Sn_{13}$ and (d) $YbCoGa_5$

The advantage of flux growth over arc melting and the use of an induction furnace is the possibility of tuning different parameters to achieve crystal formation. These parameters may include ramp temperature/rate and dwell temperature/time, as well as stoichiometric amounts of constituent elements. For example, during our exploration of the Yb-Co-Sn system, the major phase stabilized was binary $CoSn_2$. We discovered that by varying the amounts of the constituent elements from a 1:1:20 (Yb:Co:Sn) molar ratio to a 2:1:10 molar ratio, we were able to synthesize crystals of $Yb_3Co_4Sn_{12.79}$. Also, by increasing the dwell period from 24 h to 48 h, we were able to increase the percent yield of $Yb_3Co_4Sn_{12.79}$ crystals.

1.3 Mössbauer Spectroscopy

In addition to standard solid-state characterization techniques, such as powder and single crystal X-ray diffraction, we also employed Mössbauer spectroscopy in the characterization of some of the compounds studied in this dissertation. Mössbauer spectroscopy is based on the recoil-free resonant absorption of γ-rays by the nuclei of a target element.[16] In Mössbauer spectroscopy, the γ-ray source is traditionally a radioactive material containing a nuclide that decays to a nuclear excited state of the Mössbauer element. In ^{57}Fe Mössbauer spectroscopy, as

is shown in Figure 1.2, the parent nuclide is ^{57}Co, which decays into an excited state of ^{57}Fe that emits an^{57}Fe specific γ ray.[17] In Mössbauer spectroscopy, the energy scan is achieved through the Doppler shift of the γ-ray source, a shift that varies the γ-ray frequency and hence energy, by varying the source velocity relative to that of the absorber. In ^{57}Fe Mössbauer spectroscopy, the required velocity range is of the order of ± 10 mm/s. Figure 1.3(a) shows a schematic for measuring a Mössbauer spectrum and the resulting spectra (b).[18]

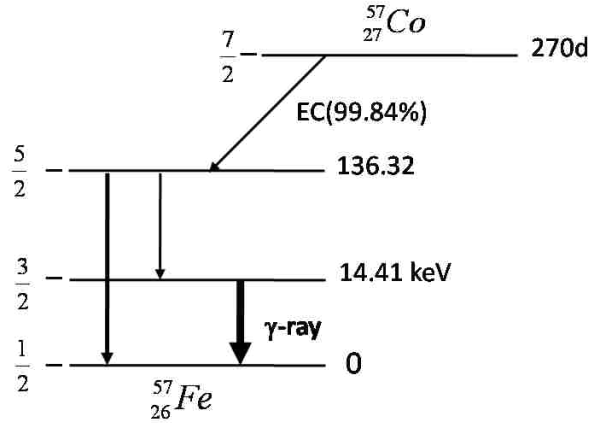

Figure 1.2 Nuclear decay scheme for the Mössbauer resonances in iron-57. Adapted from reference (13)

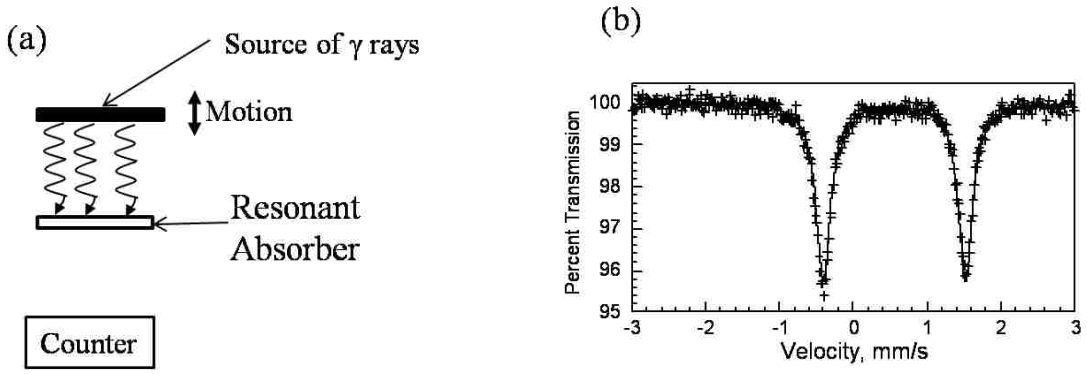

Figure 1.3 (a) Schematic for measuring a Mössbauer spectrum (b) A typical iron-57 quadrupole doublet Mössbauer spectrum. The isomer shift, δ, is the average of the velocity of the two absorption lines and the quadrupole splitting, ΔE_Q, is the difference in energy between the two lines, both expressed in mm/s. The isomer shift is given relative to α-iron powder.

The hyperfine interactions between the nucleus and its environment lead to three basic types of Mössbauer spectra for ^{57}Fe, the Mössbauer nuclide to which we restrict ourselves in this dissertation. The first hyperfine interaction is the isomer shift, which originates in the finite size of the nucleus and the impact of the electrons on the nucleus. The isomer shift moves the resonance line relative to zero velocity as shown in Figure. 1.3 (b) and is usually noted as δ and is measured relative to a zero velocity assigned to the center of the α-iron spectrum.

The isomer shift is sensitive to the iron oxidation state and coordination number. Hence, its measurement can used to determine oxidation state and to study mixed valence compounds and charge hopping.[16] The second type of hyperfine interaction is the electric quadrupole interaction, which originates in the interaction between the nuclear quadrupole moment, i.e., the non-sphericity of the ^{57}Fe nuclear charge distribution, and the electric field gradient at the nucleus.[16] The quadrupole interaction leads to a doublet, as is shown in Fig. 1.3 (b) and indicates that the charge distribution around the iron nuclide is not spherical. The quadrupole interaction is measured by the doublet splitting and is usually noted, ΔE_Q. The third hyperfine interaction is the magnetic Zeeman splitting, which originates in the interaction between the ^{57}Fe nuclear magnetic dipole moment and the magnetic field created internally by the electrons or applied externally. This interaction leads to a sextet whose overall splitting is proportional to the magnetic field experienced by iron, a field that is proportional to the iron magnetic moment. Hence, it is possible to estimate the iron magnetic moment from a measure of the sextet splitting.

1.4 Physical Properties

The electrical resistivity (ρ) of a substance can be defined as: $\rho = \frac{RA}{L}$, where R = electrical resistance, A = cross sectional area and L = length of material. The electrical resistivity of a

normal metal increases with an increase in temperature.[19] The quality of a material can be determined by the residual resistivity ratio, which is the resistivity at 293 K divided by resistivity at low temperature. Magnetoresistance (MR) is the change in electrical resistance in an applied field and is defined as MR (%) = $\frac{\rho_H - \rho_0}{\rho_0} \times 100$, where ρ_H is the resistivity in an applied field (H) and ρ_0 is the resistivity in the absence of a field.[19] The typical MR% of a normal metal is < 10 % at 4 T.[20]

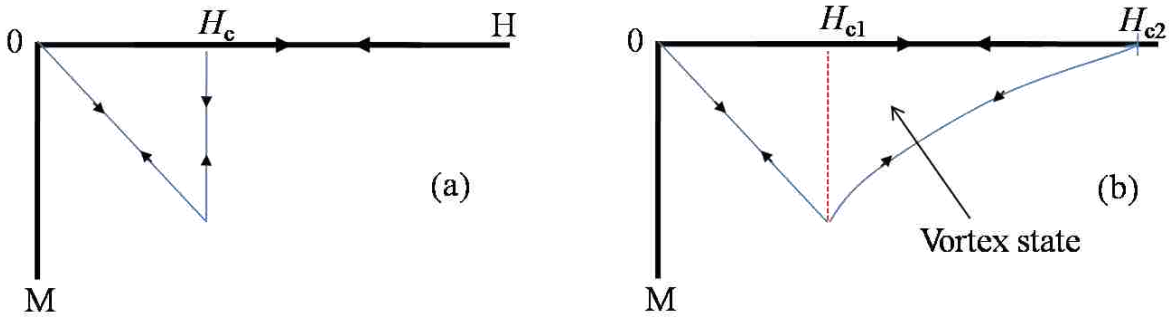

Figure 1.4 Field dependent magnetization M (H) of (a) a *Type I* superconductor, (b) a *Type II* superconductor.

Superconductivity is observed in a material when its resistivity drops to zero. The temperature at which this occurs is known as the critical temperature (T_c) of a superconductor. The superconducting state of a material can be destroyed by applying a magnetic field on the material until a critical field (H_c) is reached. Figure 1.4a shows the field dependent magnetization for a *Type I* superconductor (soft). At fields below H_c, magnetic lines of flux are screened from the superconducting sample. The field dependent magnetization of a *Type II* superconductor (hard) is shown in Figure 1.4b. Above H_{c1} a vortex state is created where magnetic lines of flux are able to penetrate the sample, and the superconducting state is destroyed above H_{c2}.

Magnetism in intermetallic compounds is associated with unpaired electrons. Depending on the orientation of these unpaired electrons we can have paramagnetism (random spins),

antiferromagnetism (antiparallel spins), ferromagnetism (parallel spins) or ferrimagnetism (antiparallel but spins differ in magnitude). The magnetic susceptibility (χ) of a material is defined as: $\chi = \frac{M}{H}$,[19] where M is magnetization and H is an applied magnetic field. Paramagnets obey the Curie law: $\chi = \frac{C}{T}$, where C is the Curie constant. Magnetic data above the ordering temperature (T_N or T_C) is fit using Curie-Weiss law.[19] Information obtained from this fit includes the value of the magnetic moment from a contributing magnetic sublattice and the type of magnetic effect present in the material. The effective magnetic moment of a sample (μ_{eff}) is defined as $\mu_{\text{eff}}^2 = \frac{3k_B C}{N\mu_B^2}$, where k_B is Boltzmann constant, N is Avogadro's number and is μ_B is Bohr magneton.[19] The type of magnetism present in a sample can also be determined using the Weiss constant (θ). If θ is close to zero, it implies that paramagnetic behavior is present in a sample. Likewise, if θ is either positive or negative, ferromagnetic or antiferromagnetic correlations are present, respectively.

The specific heat of a metal is described as $C_p = \gamma T + \alpha T^3$, where γ and α are the electronic and phonon contribution to the specific heat, respectively. At low temperatures, the electronic contribution to the specific heat is dominant and plotting C_p/T versus T^2 gives γ as the intercept. Gamma (γ) also known as the Sommerfeld coefficient is proportional to the effective mass of an electron. Typical heavy fermion materials have large γ values which are two orders of magnitude greater than a normal metal.[21] The maximum allowed phonon frequency in a crystal is known as the Debye frequency (ω_D), where ω_D is directly proportional to the Debye temperature (Θ_D) of a crystal (the temperature at which a crystal is in its highest vibrational mode). This is expressed as $\Theta_D = \frac{h\omega_D}{k_B}$, where h = Planck's constant, and k_B = Boltzmann's constant.[19]

1.5 References

(1) Steglich, F.; Aarts, J.; Bredl, C. D.; Lieke, W.; Meschede, D.; Franz, W.; Schäfer, H., *Phys. Rev. Lett.* **1979,** *43*, 1892.

(2) Mathur, N. D.; Grosche, F. M.; Julian, S. R.; Walker, I. R.; Freye, D. M.; Haselwimmer, R. K. W.; Lonzarich, G. G., *Nature* **1998,** *394*, 39.

(3) Petrovic, C.; Pagliuso, P. G.; Hundley, M. F.; Movshovich, R.; Sarrao, J. L.; Thompson, J. D.; Fisk, Z.; Monthoux, P., *J. Phys. Condes. Matter* **2001,** *13*, L337-L342.

(4) Petrovic, C.; Movshovich, R.; Jaime, M.; Pagliuso, P. G.; Hundley, M. F.; Sarrao, J. L.; Fisk, Z.; Thompson, J. D., *Europhys. Lett.* **2001,** *53*, 354-359.

(5) Nicklas, M.; Sidorov, V. A.; Borges, H. A.; Pagliuso, P. G.; Petrovic, C.; Fisk, Z.; Sarrao, J. L.; Thompson, J. D., *Phys. Rev. B* **2003,** *67*, 020506.

(6) Chen, G. F.; Ohara, S.; Hedo, M.; Uwatoko, Y.; Saito, K.; Sorai, M.; Sakamoto, I., *J. Phys. Soc. Jpn.* **2002,** *71*, 2836-2838.

(7) Thompson, J. D.; Movshovich, R.; Fisk, Z.; Bouquet, F.; Curro, N. J.; Fisher, R. A.; Hammel, P. C.; Hegger, H.; Hundley, M. F.; Jaime, M.; Pagliuso, P. G.; Petrovic, C.; Phillips, N. E.; Sarrao, J. L., *J. Magn. Magn. Mater.* **2001,** *226*, 5-10.

(8) Thomas, E. L.; Millican, J. N.; Okudzeto, E. K.; Chan, J. Y., *Comments Inorg. Chem.* **2006,** *27*, 1-39.

(9) Grin, Y. N.; Yarmolyuk, Y. P.; Gradyshevsky, E. I., *Kristallografiya* **1979,** *24*, 242-246.

(10) Hodeau, J. L.; Chenavas, J.; Marezio, M.; Remeika, J. P., *Solid State Commun.* **1980,** *36*, 839-845.

(11) Vasilenko, L. O.; Noga, A. S.; Grin, Y. N.; Koterlin, M. D.; Yarmolyuk, Y. P., *Russ. Metall.* **1988**, 216-220.

(12) Canfield, P. C., *Nat Phys* **2008,** *4*, 167-169.

(13) Feder, T., *Phys. Today* **2007,** *60*, 26-28.

(14) Kanatzidis, M. G.; Pottgen, R.; Jeitschko, W., *Angew. Chem. Int. Ed.* **2005,** *44*, 6996-7023.

(15) Lide, D., *CRC Handbook*. 79 ed.; CRC Press: New York, 1998.

(16) Long, G. J.; Editor, *Mössbauer Spectroscopy Applied to Inorganic Chemistry, Vol. 1*. 1984; p 667 pp.

(17) Gibb, T. C., *Principles of Mössbauer Spectroscopy* Chapman and Hall London, 1976.

(18) Cohen, R. L., *Applications of Mössbauer Spectroscopy*. Academic Press: New York, 1976; Vol. I.

(19) Kittel, C., *Introduction to Solid State Physics*. John Wiley & Sons: New York, 1996; p 628.

(20) Huffman, J. E.; Snodgrass, M. L.; Blatt, F. J., *Phys. Rev. B* **1981,** *23*, 483.

(21) Fisk, Z.; Hess, D. W.; Pethick, C. J.; Pines, D.; Smith, J. L.; Thompson, J. D.; Willis, J. O., *Science* **1988,** *239*, 33-42.

CHAPTER 2. CRYSTAL GROWTH, STRUCTURE, AND PHYSICAL PROPERTIES OF $Ln_3Co_4Sn_{13}$ (*Ln* = Pr, Nd, Sm, Gd and Tb), $Yb_3Co_4Sn_{12+x}$ (x = 0.79 and 0.90), $Ln_7Co_6Sn_{23}$ (*Ln* = Dy, and Ho), and $Ln_5Co_6Sn_{18}$ (*Ln* = Er, and Tm) [*]

2.1 Introduction

Remeika phases have been widely studied because they display remarkable physical properties such as superconductivity, magnetism and heavy fermion behavior.[1-10] These compounds crystallize in a group of related phases, named as (I-IV). Phase I, or the $Yb_3Rh_4Sn_{13}$ structure type is primitive cubic ($Pm\bar{3}n$) with a ~ 9.5 Å.[11] Phase II is tetragonal ($I4_1/acd$) $Sn_{1-x}Er_xEr_4Rh_6Sn_{18}$ structure with lattice parameters a ~ 13.7 Å and c ~ 27.4 Å.[12] Phase III, also known as Phase II′, crystallizes in the cubic ($Fm\bar{3}m$) $Tb_5Rh_6Sn_{18}$ structure with a ~ 13 Å.[13] Phase IV, which is a distorted form of Phase I (Phase I′), adopts the cubic $Pr_3Rh_4Sn_{13}$ structure type ($Pm\bar{3}n$) with a ~ 9.5 Å.[1] The different phases are similar in that they contain MSn_6 (*M* = Co, Rh, Ir, Ru, and Os) trigonal prisms and rare earth polyhedral units.[14] The formation of a particular phase depends on the size and the oxidation state of the rare-earth and the transition metal in the compound.[12, 15, 16] The cubic $Pm\bar{3}n$ structure is formed for rare earth compounds with larger atomic radii (Ce, Pr, Nd, Sm, Eu, Gd), [10, 17-22] while the tetragonal $I4_1/acd$ Phase II and cubic $Fm\bar{3}m$ Phase III compounds are formed for the smaller rare-earth metals (Dy, Ho, Er, Tm).[18, 22, 23] Compounds that crystallize in the cubic $Pm\bar{3}n$ ($Ln_3M_4Sn_{13}$) structure type (*M* = Rh, Ir, Co) are $Ln_3Rh_4Sn_{13}$ (*Ln* = La-Nd, Sm-Gd; Yb),[10, 18, 22] $Ln_3Ir_4Sn_{13}$ (*Ln* = La-Nd, Sm-Gd and Ca), [10, 18] and $Ln_3Co_4Sn_{13}$ (*Ln* = La-Nd, Sm, Gd, Tb and Yb).[17-21] The smaller rare earth analogues $LnRh_xSn_y$ (*Ln* = Ho-Tm, Lu, Y and Sc),[22, 23] $LnIr_xSn_y$ (*Ln* = Er-Yb; Sc) and $LnCo_xSn_y$

---

[*] Portions of this chapter reprinted by permission from Taylor & Francis. Thomas, E.L.; Millican, J. N.; Okudzeto, E. K.; Chan, J. Y; "Crystal Growth and the Search for Heavy Fermion Intermetallics" *Comments Inorg. Chem.* **2006,** 27, 1-39

[*]Portions of this chapter reprinted by permission of Elsevier: Okudzeto, E.K; Thomas, E.L.; Moldovan, M.; Young D.P. and Chan J.Y; "Magnetic properties of the stannides $Ln_7Co_6Sn_{23}$ (*Ln* =Dy, Ho), and $Ln_5Co_6Sn_{18}$ (*Ln* = Er, Tm)" *Physica B.* **2008. 403,** 1628-1629

(*Ln* = Dy -Tm, Lu and Sc)[23] adopt the tetragonal Phase II structure, and the cubic Phase III ($Fm\bar{3}m$) structure type is adopted by $LnRh_xSn_y$ (*Ln* = Tb-Tm; Yb) and $LnIr_xSn_y$ (*Ln* = Gd-Yb; and Y). [16, 18, 23]

Several Phase I compounds display notable physical properties at low temperatures such as heavy fermion behavior and/or magnetic ordering.[3, 7, 9, 10, 15, 17, 20-22, 24-27] Heavy fermion materials are intermetallic compounds that exhibit a screening effect between their conduction electrons and the magnetic moment of their *f* electrons. Heavy fermions materials have large Sommerfeld or electronic specific heat coefficients (γ), which are about 10-1000 times that of ordinary metals[28] (Cu γ ~ 1 mJ $mol^{-1} K^{-2}$).

Among the heavy fermion compounds within this structure type is $Ce_3Ru_4Sn_{13}$, which consists of mixed valent Ce (Ce^{3+} and Ce^{4+}) and shows enhanced mass behavior with γ = 592 mJ mol^{-1}-Ce K^{-2}).[7, 26] $Ce_3Pt_4In_{13}$ is a heavy fermion with γ ~ 1 J mol^{-1}-Ce K^{-2} and orders antiferromagnetically at T_N = 0.95 K.[29] $Ce_3Ir_4Sn_{13}$ is also a heavy fermion with two anomalies at 0.6 K and 2.0 K with γ ~ 670 mJ mol^{-1}-Ce K^{-2}.[8] Recently, Thomas *et al.* reported the structure and physical properties of $Ce_3Co_4Sn_{13}$, which has an enhanced γ ~ 4280 mJ mol^{-1}-Ce K^{-2} at its transition peak temperature 0.6 K, one of the largest Sommerfeld coefficients reported. [20] Superconductivity has also been observed in several other Phase I compounds $Yb_3Rh_4Sn_{13}$ (T_c = 8.2 - 8.6 K),[25] $Ca_3Rh_4Sn_{13}$ (T_c = 8.6 K), [25] $La_3Pt_4In_{13}$ (T_c = 3.3 K),[29] $La_3Co_4Sn_{13}$ (T_c = 2.85 K),[20] $Lu_3Ru_4Ge_{13}$ (T_c = 2.3 K), and $Y_3Ru_4Sn_{13}$ (T_c = 1.8 K).[7]

Mudryk et al. reported the physical properties of polycrystalline $Yb_3Co_{4.3}Sn_{12.7}$, which were grown by arc melting the constituent elements in a 15:20:65 ratio.[27] The structural model of $Yb_3Co_{4.3}Sn_{12.7}$ was determined by Rietveld analysis. Resistivity measurements show that $Yb_3Co_{4.3}Sn_{12.7}$ crosses over into a superconducting state below 3.4 K and T_c diminishes upon the application of an external magnetic field and H_c is estimated to be 2.5 T.[27] The calculated

specific heat coefficient (γ) of $Yb_3Co_{4.3}Sn_{12.7}$ is 46(4) mJ mol^{-1} K^{-2} and a Debye temperature of 207(5) K which is similar to that of elemental Sn (190 K).

Several Phase II compounds show superconductivity and/or reentrant superconductivity; among the superconducting compounds are $TbOs_{1.5}Sn_{2.6}$ and $HoOs_{1.5}Sn_{2.6}$ with T_c = 1.4 K for both compounds.[30] Reentrant superconductors are materials that have a magnetic transition T_M at a temperature lower than T_c. At T_M the superconductivity of the material disappears and an ordered magnetic state is observed.[22] The reentrant superconductors in Phase II are Sn_{1-x} $Er_xEr_4Rh_6Sn_{18}$ with T_c = 0.97 K and T_N = 0.57 K,[31] Sn_{1-x} $Er_xEr_4Os_6Sn_{18}$ with T_c =1.3 K and T_N = 0.5 K, and Sn_{1-x} $Tm_xTm_4Os_6Sn_{18}$ with T_c = 1.1 K and T_N = 0.6 K.[30]

During our search for ternary phases in the *Ln*-Co-Sn system we have grown single crystals of $Ln_3Co_4Sn_{13}$ (*Ln* = Pr, Nd, Sm, Gd, Tb) and have reported the structural and magnetic properties of theses compounds.[21] Our investigation of compounds in the *Ln*-Co-Sn system resulted in the crystal growth of $Ln_5Co_6Sn_{18}$ (*Ln* = Er, Tm) and $Ln_7Co_6Sn_{23}$ (*Ln* = Dy, Ho). Sn_{1-x} $Er_xEr_4Co_6Sn_{18}$ (*Ln* = Er, Tm) have been previously synthesized by Espinosa *et al.*,[23, 32] and X-ray powder diffraction data show that these compounds adopt the $I4_1/acd$ space group with lattice parameters a = 13.529 Å and c = 9.522 Å.[18] However the full structure determination is necessary to correlate trends in this family of compounds. $Ln_7Co_6Sn_{23}$ (*Ln* = Dy, Ho) compounds crystallize with the $Ho_7Co_6Sn_{23}$ structure type,[33] and the magnetic susceptibility for $Ln_7Co_6Sn_{23}$ (*Ln* = Y, Tb, Dy, Ho, Er) show paramagnetic behavior between 78 K to 298 K.[34]

This chapter highlights the full structure determination of single crystals of $Ln_3Co_4Sn_{13}$ (*Ln* = Pr, Nd, Sm, Gd, Tb and Yb), $Ln_7Co_6Sn_{23}$ (*Ln* = Ho, Dy), $Ln_5Co_6Sn_{18}$ (*Ln* = Er, Tm). A comparison between the structures of $Ln_3Co_4Sn_{13}$ (*Ln* = Pr, Nd, Sm, Gd, Tb), $Ln_7Co_6Sn_{23}$ (*Ln* = Ho, Dy) and $Ln_5Co_6Sn_{18}$ (*Ln* = Er, Tm) as well as the magnetic and transport behavior of the

$Ln_3Co_4Sn_{13}$ (*Ln* = Pr, Nd, Sm, Gd, Tb), $Ln_7Co_6Sn_{23}$ (*Ln* = Ho, Dy), $Ln_5Co_6Sn_{18}$ (*Ln* = Er, Tm) and $Yb_3Co_4Sn_{12+x}$ (x = 0.79 and 0.90).

2.2 Experimental

2.2.1 Synthesis

Single crystals of $Ln_3Co_4Sn_{13}$ (*Ln* = Pr, Nd, Sm, Gd, Tb), $Ln_7Co_6Sn_{23}$ (*Ln* = Dy and Ho), and $Ln_5Co_6Sn_{18}$ (*Ln* = Er, Tm) were synthesized using the respective rare-earth metal ingots of Pr, Nd, Sm, Gd, Tb Dy, Ho, Er, and Tm (99.9 %), Co powder (99.998 %), and Sn shot (99.8 %) which were all purchased from Alfa Aesar and used as received. The constituent elements were combined in a 1:1:20 (*Ln*: Co: Sn) mole ratio, covered with quartz wool, and sealed into an evacuated, fused-silica tube. The samples were then heated to 1323 K for 24 h and slowly cooled to 573 K at a rate of 5 K/h. Single crystals of $Yb_3Co_4Sn_{12.79}$ were grown in Sn flux using the constituent elements (Yb (99.9 %), Co (99.998 %), and Sn (99.99 %), all obtained from Alfa Aesar and were used as received. The elements were combined in a 2:1:10 (Yb:Co:Sn) mole ratio, covered with quartz wool and sealed into an evacuated fused-silica tube. The sample was then heated to 1323 K for 48 h, and slowly cooled to 550 K at a rate of 5 K/h. Excess flux was separated from the crystals by centrifugation, and when necessary, topical flux was removed by etching the recovered crystals in concentrated HCl. Single crystals obtained for $Ln_3Co_4Sn_{13}$ (*Ln* = Pr, Nd, Sm, Gd, Tb) and were cuboidal-shaped with maximum dimensions of about 2 mm^3.[21] The crystals obtained for $Ln_7Co_6Sn_{23}$ (*Ln* = Dy and Ho) and $Ln_5Co_6Sn_{18}$ (*Ln* = Er, Tm) were irregularly shaped, with dimensions up to 2 mm^3. Initial phase identifications of $Ln_7Co_6Sn_{23}$ (*Ln* = Dy and Ho) and $Ln_5Co_6Sn_{18}$ (*Ln* = Er, Tm) were made by comparing their powder X-ray diffraction (XRD) patterns with that of $Sn_{1-x}Er_xEr_4Rh_6Sn_{18}$[12] and $Ho_7Co_6Sn_{23}$.[34]

Single crystals of $Yb_3Co_4Sn_{12+x}$ (x = 0.79 and 0.90) were grown in Sn flux using the constituent elements Yb (99.9 %), Co (99.998 %), and Sn (99.99 %), all obtained from Alfa

Aesar and used as received. The elements were combined in a 2:1:10 (Yb:Co:Sn) mole ratio, covered with quartz wool and sealed into an evacuated fused-silica tube. The composition of x in single crystals of $Yb_3Co_4Sn_{12+x}$ varies with dwell period as discussed in the single crystal structure determination section. The x = 0.79 sample was heated to 1323 K for 48 h, and slowly cooled to 550 K at a rate of 5 K/h. Varying the dwell period from 48 to 24 h resulted in the synthesis of crystals with x = 0.90. The excess flux was separated from the crystals by centrifugation, and when necessary topical flux was removed by treating the recovered crystals with concentrated HCl. The crystals obtained for $Yb_3Co_4Sn_{12+x}$ (x = 0.79 and 0.90) were irregularly shaped with maximum dimensions of 2 mm^3. Multiple crystals of $Ln_3Co_4Sn_{13}$ (*Ln* = Pr, Nd, Sm, Gd and Tb), $Ln_7Co_6Sn_{23}$ (*Ln* = Dy, Ho), $Ln_5Co_6Sn_{18}$ (*Ln* = Er, Tm) and $Yb_3Co_4Sn_{12+x}$ (x = 0.79 and 0.90) were selected for characterization using single crystal X-ray diffraction.

2.2.2 Single Crystal X-ray Diffraction

Crystal fragments with dimensions of ~ 0.05 x 0.05 x 0.08 mm^3 were mechanically selected for the structural analysis of $Ln_3Co_4Sn_{13}$ (*Ln* = Pr, Nd, Sm, Gd, Tb). For the structure analysis of $Ln_7Co_6Sn_{23}$ (*Ln* = Dy, Ho) and $Ln_5Co_6Sn_{18}$ (*Ln* = Er, Tm), the dimensions ranged from 0.05 x 0.08 x 0.08 mm^3 to 0.05 x 0.05 x 0.08 mm^3. For the structure analysis of $Yb_3Co_4Sn_{12+x}$ (x = 0.79 and 0.90) crystal fragments with dimensions ranging from 0.03 x 0.05 x 0.05 to 0.05 x 0.05 x 0.05 were used. The fragments were glued on the tip of a glass fiber then mounted on a Nonius Kappa CCD diffractometer (Mo K_α radiation (λ = 0.71073Å)). Data collections were obtained at 298 K. Additional crystallographic parameters are included in Tables 2.1, 2.2 and 2.3. The structures of $Ln_3Co_4Sn_{13}$ (*Ln* = Pr, Nd, Sm, Gd, Tb) were solved by selecting an appropriate space group, $Pm\bar{3}n$, and direct solution methods were used to refine the models using SHELXL97.[35] The occupancy parameters of $Ln_3Co_4Sn_{13}$ (*Ln* = Pr, Nd, Sm, Gd, Tb) were refined in a separate sets of least-squares cycles to determine the compositions on the

2*a* site. The Sn1 sites in $Ln_3Co_4Sn_{13}$ (*Ln* = Pr, Nd, Sm, Gd, Tb) are fully occupied. Table 2.4 lists the atomic positions, Wyckoff symmetry, and anisotropic displacement parameters for $Ln_3Co_4Sn_{13}$ (*Ln* = Pr, Nd, Sm, Gd, Tb).[21]

The structures of $Yb_3Co_4Sn_{12+x}$ (x = 0.79 and 0.90) were solved with direct methods using SHELXL97.[35] The atomic parameters of the parent structure $Yb_3Rh_4Sn_{13}$[11] were used to further refine the structural models of $Yb_3Co_4Sn_{12+x}$ (x = 0.79 and 0.90). After refinement, the data were corrected for both absorption and displacement parameters and were refined as anisotropic. The displacement parameters on the Sn1 (2*a*) site for both set of crystals (the 48 and 24 h synthesized samples) were larger than expected, which is an indication of occupational disorder on this site. To determine the composition of our single crystals, the occupancy parameters were refined in a separate set of least-squares cycles. For crystals formed by dwelling for 48 h the Sn1 occupancy is 79.2(10) %, resulting in the formula $Yb_3Co_4Sn_{12.79}$. Dwelling for 24 h results in a Sn1 occupancy of 89.5(11) % with the formula $Yb_3Co_4Sn_{12.90}$. Similar occupational defects are also observed in other $Ln_3M_4Sn_{13}$ analogues such as $Ce_4Rh_4Sn_{13}$ (92 %) and $Ce_3Ir_4Sn_{13}$ (76 %).[10] The final least-squares refinement resulted in a $R_1(F)$ of 0.0230 for $Yb_3Co_4Sn_{12.79}$ and $R_1(F)$ of 0.0235 for $Yb_3Co_4Sn_{12.90}$ (Table 2.1). We also investigated the occupational defect on different crystals obtained from the 48 h synthesis batch. The Sn1 occupancy on the 2*a* site is within σ^2 standard deviation, indicating the occupational disorder in crystals from this batch is similar. The physical properties measured on single crystals of $Yb_3Co_4Sn_{12.79}$ and $Yb_3Co_4Sn_{12.90}$ are the same indicating the properties are not affected by the occupational defects. Mudryk et al. reported a statistical distribution of Co (32 %) and Sn (68 %) on the 2*a* site of $Yb_3Co_{4.3}Sn_{12.7}$.[27] Refining our model with statistical disorder (Co and Sn) on the 2*a* site results in a statistical distribution of Co (46 %) and Sn (54 %) for the crystals synthesized by dwelling for 48 h. Dwelling for 24 h results in a Co (23 %) and Sn (77 %)

distribution. Table 2.5 and 2.6 lists the atomic positions, Wyckoff symmetry, anisotropic displacement parameters, occupancy and $R_1(F)$ values for the various models.

In solving the structures of $Ln_7Co_6Sn_{23}$ (Ln = Dy, Ho) and $Ln_5Co_6Sn_{18}$ (Ln = Er, Tm), the structural data of the known phases $Ho_7Co_6Sn_{23}$[33] and $Sn_{1-x}Er_xEr_4Rh_6Sn_{18}$[12] were used as preliminary models. The structural models were refined using SHELXL97.[35] After refinement, the data were corrected for absorption and displacement parameters were refined as anisotropic. The occupancy parameters of $Sn_{1-x}Ln_xLn_5Co_6Sn_{18}$ (Ln = Er, Tm) were refined in a separate set of least-square cycles to determine the exact composition on the 8*b* site, which could be occupied with Sn and *Ln*, as observed in $Sn_{1-x}Er_xEr_4Rh_6Sn_{18}$.[12] However, no mixed occupancies were observed for both compounds. A list of atomic positions, Wyckoff symmetry, and anisotropic displacement parameters for the above compounds are listed in Table 2.7. Although the thermal parameters of $Ln_5Co_6Sn_{18}$ (Ln = Er and Tm) appeared to be large on the Sn6 (32*g*) site no disorder was observed in least-square refinements. Unusual thermal parameters were also observed in the single crystal refinement of the disordered, microtwinned $Sc_{1-x}Sc_4Co_6Sn_{18}$ compound.[36]

2.2.3 Physical Property Measurements

Magnetic measurements on single crystals of $Ln_3Co_4Sn_{13}$ (Ln = Pr, Nd, Sm, Gd, Tb), $Ln_7Co_6Sn_{23}$ (Ln = Dy, Ho), and $Ln_5Co_6Sn_{18}$ (Ln = Er, Tm) were performed using a Quantum Design Physical Property Measuring System (PPMS). Data were collected over a temperature range of 2 to 300 K. The magnetic measurements on single crystals of $Yb_3Co_4Sn_{12.79}$ were performed up to 350 K. Electrical resistivity data on all the above compounds were measured using the standard four probe method with a Quantum Design PPMS. Specific heat measurements were performed with a Quantum Design PPMS.

Table 2.1 Crystallographic Parameters for $Ln_3Co_4Sn_{13}$ (*Ln* = Pr, Nd, Sm, Gd, Tb)

Compound	$Pr_3Co_4Sn_{13}$	$Nd_3Co_4Sn_{13}$	$Sm_3Co_4Sn_{13}$	$Gd_3Co_4Sn_{13}$	$Tb_3Co_4Sn_{13}$
Space Group	$Pm\bar{3}n$	$Pm\bar{3}n$	$Pm\bar{3}n$	$Pm\bar{3}n$	$Pm\bar{3}n$
a (Å)	9.582 (6)	9.583(8)	9.5350(6)	9.5190(4)	9.5010(6)
V (Å^3)	879.77(10)	880.0(12)	866.89(9)	862.53(6)	857.65(9)
Z	2	2	2	2	2
Dimensions (mm^3)	0.05x0.05x0.08	0.05x0.05x0.08	0.05x0.05x0.08	0.05x0.05x0.08	0.05x0.05x0.05
Temperature (K)	298(2)	298(2)	298(2)	298(2)	298(2)
ρ (g/cm3)	8.310	8.345	8.542	8.665	10.036
θ Range	3.01-30.02	3.01-30.02	3.02-30.00	3.01-29.16	3.03- 30.03
μ (mm-1)	29.819	29.819	31.993	33.476	33.489
Collected reflections	749	779	708	750	680
Unique reflections	227	237	225	234	24
h	$-13 \leq h \leq 13$	$13 \leq h \leq 13$	$-13 \leq h \leq 13$	$-13 \leq h \leq 13$	$-13 \leq h \leq 13$
k	$-9 \leq k \leq 9$	$-9 \leq k \leq 9$	$-9 \leq k \leq 9$	$-9 \leq k \leq 9$	$-9 \leq k \leq 9$
l	$-9 \leq l \leq 9$	$-9 \leq l \leq 9$	$-8 \leq l \leq 8$	$-8 \leq l \leq 8$	$-8 \leq l \leq 8$
$\Delta\rho_{max}$ (eÅ^{-3})	2.813	1.113	1.400	1.016	3.907
$\Delta\rho_{min}$ (eÅ^{-3})	-1.279	-1.637	-3.367	-3.304	-3.894
R_1 (F)[a]	0.0338	0.0257	0.0235	0.0235	0.0395
R_w[b]	0.0707	0.0619	0.0599	0.0543	0.0757

[a] $R_1 = \Sigma||F_o| - |F_c||/\Sigma|F_o|$

[b] $R_w = [\Sigma [w (F_o^2 - F_c^2)^2]/ \Sigma [w (F_o^2)^2]]^{1/2}$; w = $1/[\sigma^2(F_o^2) + (0.0224P)^2 + 4.3937P]$, w = $1/[\sigma^2(F_o^2) + (0.0346P)^2 + 2.1024P]$, w = $1/[\sigma^2(F_o^2) + (0.0000P)^2 + 11.3670P]$, w = $1/[\sigma^2(F_o^2) + (0.0056P)^2 + 15.0860P]$, w = $1/[\sigma^2(F_o^2) + (0.0617P)^2 + 25.9124P]$, respectively for Pr, Nd, Sm, Gd and Tb

Table 2.2 Crystallographic Parameters for $Yb_3Co_4Sn_{12+x}$ (x = 0.79 and 0.90)

Dwell Time	48 h	24 h
Formula	$Yb_3Co_4Sn_{12.79}$	$Yb_3Co_4Sn_{12.90}$
Space Group	$Pm\bar{3}n$	$Pm\bar{3}n$
a (Å)	9.5330(5)	9.5330(4)
V (Å^3)	866.34(8)	866.34(6)
Z	2	2
Dimensions (mm^3)	0.03 x 0.05 x 0.05	0.05 x 0.05 x 0.05
Temperature (K)	298(2)	298(2)
ρ (g/cm3)	8.713	8.761
θ Range	3.02- 30.01	4.28-30.01
μ (mm^{-1})	37.742	37.890
Collected reflections	753	751
Unique reflections	240	235
R_{int}	0.0372	0.0353
h	$-13 \leq h \leq 13$	$-13 \leq h \leq 13$
k	$-9 \leq k \leq 9$	$-9 \leq k \leq 9$
l	$-8 \leq k \leq 8$	$-8 \leq k \leq 8$
$\Delta\rho_{max}$ (eÅ^{-3})	1.535	1.559
$\Delta\rho_{min}$ (eÅ^{-3})	-0.962	-1.445
Goodness of fit on F_o^2	1.259	1.203
Extinction coefficient	0.0030(2)	0.0055(3)
R_1 (F) for $F_o^2 > 2\sigma(F_o^2)$[a]	0.0230	0.0235
$R_w(F_o^2)$[b]	0.0514	0.0497

[a] $R_1 = \Sigma||F_o| - |F_c||/\Sigma|F_o|$ [b] $R_w = [\Sigma [w (F_o^2 - F_c^2)^2]/ \Sigma [w (F_o^2)^2]]^{1/2}$; w = $1/[\sigma^2(F_o^2) + (0.0086P)^2 + 6.6792P]$, w = $1/[\sigma^2(F_o^2) + (0.0086P)^2 + 10.3281P]$ for the 48h and 24h samples respectively.

Table 2.3 Crystallographic Parameters for $Ln_7Co_6Sn_{23}$ (*Ln* = Dy, Ho) and $Ln_5Co_6Sn_{18}$ (*Ln* = Er, Tm)

Compound	$Dy_7Co_6Sn_{23}$	$Ho_7Co_6Sn_{23}$	$Er_5Co_6Sn_{18}$	$Tm_5Co_6Sn_{18}$
Space Group	$P\bar{3}m1$	$P\bar{3}m1$	$I4_1/acd$	$I4_1/acd$
a (Å)	9.6420(4)	9.6210(3)	13.5310(2)	13.5190(6)
c (Å)	9.8590(5)	9.8210(4)	26.9970(4)	26.9760(9)
V (Å^3)	793.77(6)	787.27(5)	4942.83(13)	4930.2(4)
Z	1	1	8	8
Crystal Dimensions (mm^3)	0.05x0.08x0.08	0.05x0.08x0.08	0.05x0.05x0.08	0.05x0.05x0.08
Temperature (K)	298(2)	298(2)	298(2)	298(2)
ρ (g/cm3)	8.830	8.939	8.940	8.938
θ Range	2.07-30.05	2.07-30.02	2.61-30.50	2.61-30.03
μ (mm-1)	36.961	38.245	38.446	39.518
Collected reflections	2464	2772	6939	5700
Unique reflections	841	855	1785	1415
h	-13≤ h ≤ 13	-13≤ h ≤ 13	-19≤ h ≤ 19	-18≤ h ≤ 18
k	-11≤ k ≤ 11	-11≤ k ≤ 10	-13≤k ≤ 13	-13≤k ≤ 13
l	-13≤ l ≤ 9	-13≤ l ≤ 9	-37≤ l ≤ 37	-13≤ l ≤ 13
$\Delta\rho_{max}$ (eÅ^{-3})	2.661	12.891	20.645	21.338
$\Delta\rho_{min}$ (eÅ^{-3})	-2.071	-5.345	-6.501	-11.649
R_1 (F)[a]	0.0221	0.0464	0.0678	0.0942
R_w[b]	0.0541	0.1452	0.1910	0.2463

[a] $R_1 = \Sigma||F_o| - |F_c||/\Sigma|F_o|$

[b] $R_w = [\Sigma [w (F_o^2 - F_c^2)^2]/ \Sigma [w (F_o^2)^2]]^{1/2}$; w = 1/[$\sigma^2(F_o^2)$ +(0.0000P)^2 +1.9810P], w = 1/[$\sigma^2(F_o^2)$ +(0.1000P)^2 +0.0000P], w = 1/[$\sigma^2(F_o^2)$ +(0.0003P)^2 +10.7560P], w = 1/[$\sigma^2(F_o^2)$ +(0.0093P)^2 +9.5760P], respectively for Dy, Ho, Er and Tm

Table 2.4 Atomic Positions and Atomic Displacement Parameters for $Ln_3Co_4Sn_{13}$ (*Ln* = Pr, Nd, Sm, Gd, Tb)

Atom	Wyckoff site	x	y	z	U_{eq} (eÅ^2) [a]
		$Pr_3Co_4Sn_{13}$			
Sn1	2*a*	0	0	0	0.0154(5)
Pr	6*d*	1/4	1/2	0	0.0101(3)
Co2	8*e*	3/4	3/4	3/4	0.0076(5)
Sn2	24k	0	0.30350(7)	0.15685(7)	0.0135(3)
		$Nd_3Co_4Sn_{13}$			
Sn1	2*a*	0	0	0	0.0169(4)
Nd	6*d*	1/4	1/2	0	0.0126(3)
Co2	8*e*	3/4	3/4	3/4	0.0089(4)
Sn2	24k	0	0.30340(5)	0.15687(5)	0.0148(3)
		$Sm_3Co_4Sn_{13}$			
Sn1	2*a*	0	0	0	0.0209(6)
Sm	6*d*	1/4	1/2	0	0.0116(3)
Co2	8*e*	3/4	3/4	3/4	0.0088(4)
Sn2	24k	0	0.30448(7)	0.15704(7)	0.0141(3)

Table 2.4 cont

		$Gd_3Co_4Sn_{13}$			
Sn1	2*a*	0	0	0	0.0120(3)
Gd	6*d*	1/4	1/2	0	0.0120(3)
Co2	8*e*	3/4	3/4	3/4	0.0082(4)
Sn2	24k	0	0.30465(7)	0.15702(6)	0.0138(3)
		$Tb_3Co_4Sn_{13}$			
Sn1	2*a*	0	0	0	0.0171(9)
Tb	6*d*	1/4	1/2	0	0.0092(5)
Co2	8*e*	3/4	3/4	3/4	0.0051(7)
Sn2	24k	0	0.30494(12)	0.15689(11)	0.0104(5)

[a] U_{eq} is defined as one-third of the trace of the orthogonalized U_{ij} tensor

Table 2.5 Atomic Positions and Atomic Displacement Parameters for Crystals Grown by Dwelling for 48 h.

Atom	Wyckoff site	*x*	*y*	*z*	Occ.	U_{eq} (eÅ^2)
			$Yb_3Co_4Sn_{12.79}$			
Sn1	2*a*	0	0	0	0.792(10)	0.0168(9)
Yb	6*d*	¼	½	0	1	0.0111(4)
Co	8*e*	¾	¾	¾	1	0.0060(4)
Sn2	24*k*	0	0.30388(6)	0.15733(5)	1	0.0063(3)
			R_1 = 0.0230			
			$Yb_3Co_{4.46}Sn_{12.54}$			
Sn1	2*a*	0	0	0	0.54(2)	0.0153(9)
Co	2*a*	0	0	0	0.46(2)	0.0153(9)
Yb	6*d*	¼	½	0	1	0.0111(4)
Co	8*e*	¾	¾	¾	1	0.0060(4)
Sn2	24*k*	0	0.30388(6)	0.15733(5)	1	0.0063(3)
			R_1 = 0.0231			

[a] U_{eq} is defined as one-third of the trace of the orthogonalized U_{ij} tensor

Table 2.6 Atomic Positions and Atomic Displacement Parameters for Crystals Grown with 24h Dwell time.

Atom	Wyckoff site	*x*	*y*	*z*	Occ.	U_{eq} (eÅ^2)
			$Yb_3Co_4Sn_{12.90}$			
Sn1	2*a*	0	0	0	0.895(11)	0.0225(9
Yb	6*d*	¼	½	0	1	0.0104(4)
Co	8*e*	¾	¾	¾	1	0.0056(4)
Sn2	24*k*	0	0.30576(6)	0.15786(6)	1	0.0056(3)
			R_1 = 0.0235			
			$Yb_3Co_{4.23}Sn_{12.77}$			
Sn1	2*a*	0	0	0	0.77(2)	0.0218(9)
Co1	2*a*	0	0	0	0.23(2)	0.0218(9)
Yb	6*d*	¼	½	0	1	0.0104(4)
Co2	8*e*	¾	¾	¾	1	0.0056(4)
Sn2	24*k*	0	0.30576(6)	0.15786(6)	1	0.0056(3)
			R_1 = 0.0235			

[a] U_{eq} is defined as one-third of the trace of the orthogonalized U_{ij} tensor

Table 2.7 Atomic Positions and Atomic Displacement Parameters for $Ln_7Co_6Sn_{23}$ (*Ln* = Dy, and Ho) and $Ln_5Co_6Sn_{18}$ (*Ln* = Er, Tm)

Atom	Wyckoff site	*x*	*y*	*z*	U_{eq} (eÅ^2) [a]
			$Dy_7Co_6Sn_{23}$		
Dy	1*a*	0	0	0	0.0124(2)
Dy	6*i*	0.47844(2)	0.52156(2)	0.30648(3)	0.00851(13)
Co	6*i*	0.16812(6)	0.83188(6)	0.80138(10)	0.0079(2)
Sn1	2*d*	1/3	2/3	0.81969(9)	0.0089(2)
Sn2	6*i*	0.21860(3)	0.78140(3)	0.54551(5)	0.01042(15)
Sn3	6*i*	0.11753(3)	0.88247(3)	0.27551(5)	0.00981(15)
Sn4	1*b*	0	0	1/5	0.0121(3)
Sn5	6g	0.34767(5)	0	0	0.01075(15)
Sn6	2*d*	1/3	2/3	0.11368(9)	0.0097(2)
			$Ho_7Co_6Sn_{23}$		
Ho	1*a*	0	0	0	0.0062(4)
Ho	6*i*	0.47876(4)	0.52124(4)	0.30653(6)	0.0018(3)
Co	6*i*	0.16829(11)	0.83171(11)	0.80136(18)	0.0010(4)
Sn1	2*d*	1/3	2/3	0.82037(16)	0.0026(4)
Sn2	6*i*	0.21892(6)	0.78108(6)	0.54523(10)	0.0038(3)
Sn3	6*i*	0.11773(6)	0.88227(6)	0.27556(10)	0.0032(3)
Sn4	1*b*	0	0	1/5	0.0055(5)
Sn5	6*g*	0.34763(9)	0	0	0.0039(3)
Sn6	2*d*	1/3	2/3	0.11515(17)	0.0032(4)

Table 2.7 cont

			$Er_5Co_6Sn_{18}$		
Er1	8*b*	0	1/4	1/8	0.0076(7)
Er2	32*g*	0.13259(4)	0.38650(4)	0.30709(2)	0.0044(3)
Co1	16*d*	0	1/4	0.25204(11)	0.0013(10)
Co2	32g	0.24498(17)	0.25061(13)	0.37481(5)	0.0064(10)
Sn1	16*f*	0.17176(8)	0.57824(8)	0.3750	0.0036(4)
Sn2	16*f*	0.32590(8)	0.57590(8)	1/8	0.0040(4)
Sn3	16*e*	0.70985(12)	0	1/4	0.0079(7)
Sn4	32*g*	0.08875(7)	0.33997(7)	0.41974(4)	0.0066(4)
Sn5	32*g*	0.32797(7)	0.25722(8)	0.46106(4)	0.0036(5)
Sn6	32g	0.00394(9)	0.57614(7)	0.46121(4)	0.0040(6)
			$Tm_5Co_6Sn_{18}$		
Tm1	8*b*	0	1/4	1/8	0.0121(10)
Tm2	32*g*	0.13243(6)	0.38617(6)	0.30723(3)	0.0092(5)
Co1	16*d*	0	1/4	0.25222(16)	0.0057(16)
Co2	32g	0.2447(3)	0.2506(2)	0.37482(8)	0.0096(14)
Sn1	16*f*	0.17191(12)	0.57809(12)	0.3750	0.0075(6)
Sn2	16*f*	0.32606(12)	0.57606(12)	0.1250	0.0082(6)
Sn3	16*e*	0.71052(18)	0	1/4	0.0117(10)
Sn4	32*g*	0.08892(11)	0.34002(10)	0.41971(5)	0.0113(7)
Sn5	32*g*	0.32793(11)	0.25691(12)	0.46112(5)	0.0091(7)
Sn6	32g	0.00389(12)	0.57602(11)	0.46132(5)	0.0082(9)

[a] U_{eq} is defined as one-third of the trace of the orthogonalized U_{ij} tensor

2.3. Results and Discussion

2.3.1 Structure of $Ln_3Co_4Sn_{13}$ (*Ln* = Pr, Nd, Sm, Gd and Tb)

$Ln_3Co_4Sn_{13}$ (*Ln* = Pr, Nd, Sm, Gd, Tb) crystallize in the $Yb_3Rh_4Sn_{13}$ structure type. [11] The structure consists of three sublattices: a rare earth cuboctahedra ($LnSn_{12}$), a transition metal trigonal prism (TSn_6), and Sn icosahedra $Sn1(Sn2)_{12}$.[21] The structure of $Pr_3Co_4Sn_{13}$ is similar to that of perovskites, or $A'A''_3B_4O_{12}$-type compounds.[37] The *Ln* cuboctahedra ($LnSn_{12}$) shown in Figure 2.1 are both face and edge sharing and are made up of two different *Ln*-Sn2 interatomic distances (Table 2.8).[21] The *Ln*-Sn2 distances decreases from Pr-Tm; this trend is indicative of lanthanide contraction where the *Ln*-Sn bond distances contract as a result of increasing atomic radius. The distortion in the cuboctahedra, which is measure of the ratio of the different *Ln*-Sn2 distances, becomes less distorted as one moves across the row of lanthanide metals (Pr-Tb). The Co atoms in $Ln_3Co_4Sn_{13}$ (*Ln* = Pr, Nd, Sm, Gd, Tb) form trigonal prisms with Sn2 to give

[$Co(Sn2)_6$] as shown in Figure 2.2. The trigonal prisms are corner sharing and have a three-dimensional arrangement that encompasses the Sn1 atoms.[21] This is similar to the arrangement of BO_6 octahedra found in the perovskites type $A'A''_3B_4O_{12}$ compounds, where the three-dimensional arrangement of the octahedra create cages.[37]

Table 2.8 Selected Interatomic Distance (Å) for $Ln_3Co_4Sn_{13}$ (*Ln* = Pr, Nd, Sm, Gd and Tb)

	$Pr_3Co_4Sn_{13}$	**$Nd_3Co_4Sn_{13}$**	**$Sm_3Co_4Sn_{13}$**	**$Gd_3Co_4Sn_{13}$**	**$Tb_3Co_4Sn_{13}$**
Sn icosahedra					
Sn1-Sn2 (x 12)	3.2735(7)	3.273(3)	3.2666(7)	3.2625(7)	3.2582(12)
Co trigonal prism					
Co-Sn2 (x 6)	2.6073(3)	2.607(2)	2.5957(3)	2.5918(3)	2.5878(4)
Ln cuboctahedra					
Ln-Sn2 (x 4)	3.398(3)	3.398(3)	3.3764(5)	3.3697(4)	3.3061(6)
Ln-Sn2 (x 8)	3.3278(7)	3.328(3)	3.3111(6)	3.3061(6)	3.3014(10)

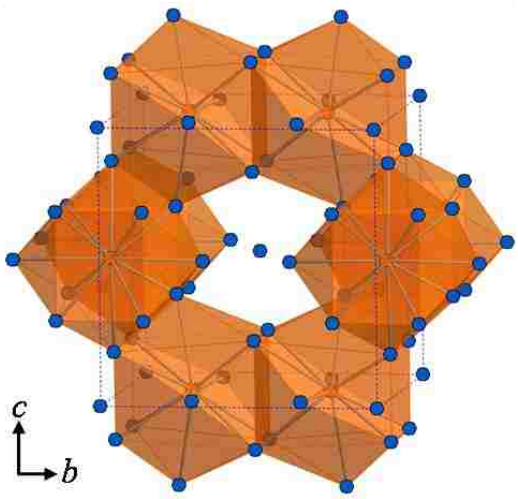

Figure 2.1 Projection of the $LnSn_{12}$ cuboctahedra (orange) of $Ln_3Co_4Sn_{13}$, Sn atoms are blue spheres.

The origin of the unit cell is occupied by the Sn1 atoms, which form edge-sharing $Sn1(Sn2)_{12}$ icosahedra (Figure 2.3). The packing of the Sn icosahedra is similar to that in $Yb_3Rh_4Sn_{13}$, where each icosahedra is connected to 8 $CoSn_6$ trigonal prisms and 12 *Ln* centered

cuboctahedra.[11] The Sn1-Sn2 distances are 3.2735(7), 3.273(3), 3.2666(7), 3.2625(7), and 3.2582(12) Å for *Ln* = Pr, Nd, Sm Gd and Tb.[21] Theses distances are slightly larger than those observed in β-Sn (4 x 3.02 Å and 2 x 3.18 Å).[38]

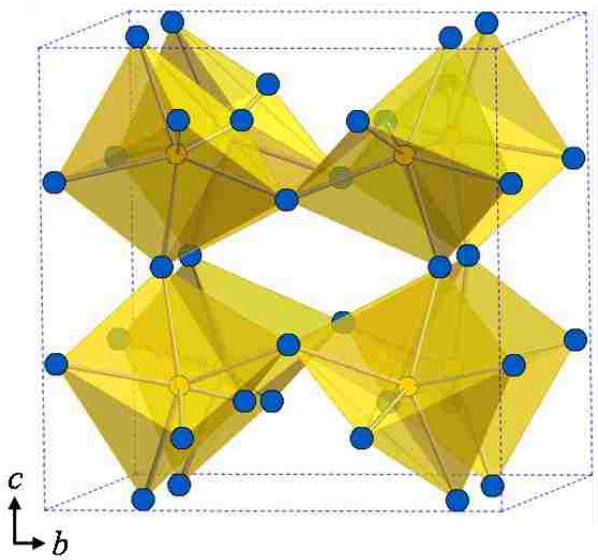

Figure 2.2 The structure of $Ln_3Co_4Sn_{13}$ showing the $CoSn_6$ trigonal prisms (gold) Sn atoms are blue spheres.

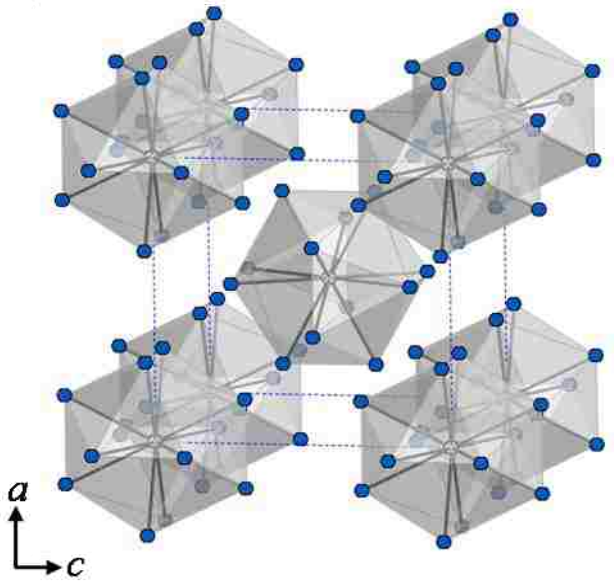

Figure 2.3 Projection of the $Sn1Sn2_{12}$ icosahedra (silver) of $Ln_3Co_4Sn_{13}$

2.3.2 Structure of $Yb_3Co_4Sn_{12+x}$ (x = 0.79 and 0.90)

$Yb_3Co_4Sn_{12+x}$ (x = 0.79 and 0.90) crystallizes in the cubic $Yb_3Rh_4Sn_{13}$[11] structure type in the space group $Pm\bar{3}n$. The structure of $Yb_3Co_4Sn_{12+x}$ (x = 0.79 and 0.90) is similar to the structure of $Ln_3Co_4Sn_{13}$ discussed in section 2.31 and consists of three sublattices: rare earth cuboctahedra ($YbSn_{12}$), Sn icosahedra $Sn1(Sn2)_{12}$, and cobalt trigonal prisms ($CoSn_6$). Figure 2.4 shows a plot of the cell volume of $Ln_3Co_4Sn_{13}$ (*Ln* = Ce-Nd, Sm, Gd, Tb) [20, 21] and $Yb_3Co_4Sn_{12.79}$. A positive deviation is observed in the volume of $Yb_3Co_4Sn_{12.79}$ indicating the divalent state of Yb in the compound. This is similar to the previously reported $Yb_3Rh_4Sn_{13}$.[16]

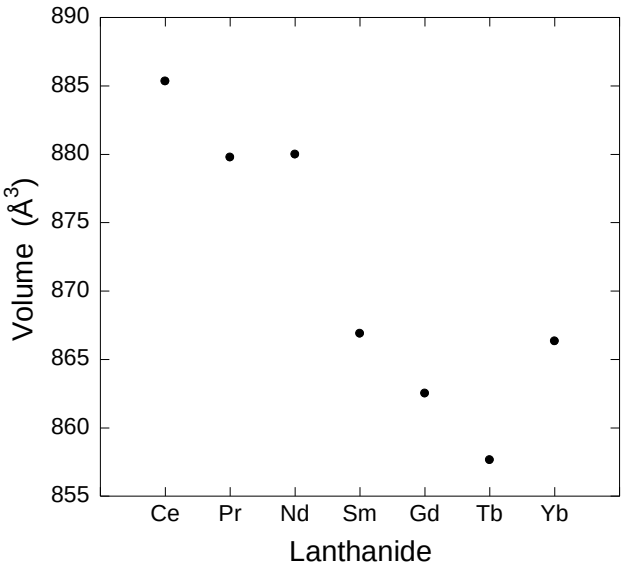

Figure 2.4 Cell volume of $Ln_3Co_4Sn_{13}$ (*Ln* = Pr, Nd, Sm, Gd, Tb) and $Yb_3Co_4Sn_{12.79}$ as a function of lanthanide. Data for the Ce, Pr, Nd, Sm, Gd, and Tb, were obtained from Ref (20) and Ref (21).

Single crystal X-ray diffraction on $Yb_3Co_4Sn_{12+x}$ (x = 0.79 and 0.90) show that crystals grown by dwelling for 48 h have an occupational defect of 20.8(10) % on the 2*a* site. Dwelling for 24 h results in crystals with an occupational defect of 10.5 %. Table 2.9 lists selected interatomic distances for the various models obtained from single crystal X-ray diffraction. The covalent radii of Co and Sn are 1.16 Å and 1.40 Å respectively.[39] If the 2*a* site is mixed with Co

and Sn, as reported by Mudryk et al.,[27] one would expect a contraction in Sn1-Sn2 distances between the partially occupied model and the mixed occupied one. From Table 2.9 the bond distance between the partial and mixed occupied models are the same. The above information suggests that the crystallographic model with occupational disorder on the 2*a* site might be an accurate model. A detailed elemental analysis technique like ICP mass spectroscopy will lead to a better determination of the composition of $Yb_3Co_4Sn_{12+x}$ (x = 0.79 and 0.90). As expected the Sn1-Sn2 distances for $Yb_3Co_4Sn_{12.79}$ are slightly smaller than that of $Yb_3Co_4Sn_{12.90}$, indicating that the dwell period during synthesis affects the amount of Sn on the 2*a* site.

Table 2.9 Selected Interatomic Distances (Å) for $Yb_3Co_4Sn_{12.79}$ (48 h partial occupied), $Yb_3Co_{4.46}Sn_{12.54}$ (48 h mixed occupied), $Yb_3Co_4Sn_{12.90}$ (24 h partial occupied) and $Yb_3Co_{4.23}Sn_{12.77}$ (48 h mixed occupied).

Formula	$Yb_3Co_4Sn_{12.79}$	$Yb_3Co_{4.46}Sn_{12.54}$	$Yb_3Co_4Sn_{12.90}$	$Yb_3Co_{4.23}Sn_{12.77}$
Dwell Time	48 h	48 h	24 h	24h
Sn1-Sn2 (x 12)	3.2622(6)	3.2621(6)	3.2804(6)	3.2804(6)
Co trigonal prism				
Co-Sn2 (x 6)	2.5931(2)	2.5931(2)	2.5950(2)	2.5950(2)
Yb cuboctahedra				
Ln-Sn2 (x 4)	3.3069(5)	3.3069(5)	3.3047(6)	3.3047(6)
Ln-Sn2 (x 8)	3.3800(4)	3.3800(4)	3.3724(4)	3.3724(4)

2.3.3 Structure of $Ln_7Co_6Sn_{23}$ (*Ln* = Dy, Ho)

$Ln_7Co_6Sn_{23}$ (*Ln* = Dy, Ho) crystallize with the $Ho_7Co_6Sn_{23}$ structure type in the space group $P\bar{3}m1$ (No.164).[33] The structure consists of four different polyhedral units: *Ln*1 cuboctahedra, *Ln*2 truncated cuboctahedra, Co trigonal prisms, and Sn octahedra ($SnSn_6$). Table 2.10 lists selected interatomic distances of the various polyhedral units. In the $Ln_7Co_6Sn_{23}$ cuboctahedra, the *Ln*1 atoms are bonded to two different crystallographic Sn atoms (Sn3 and Sn5) Figure 2.5a. The *Ln*1-Sn3 (x 6) bond distances in $Dy_7Co_6Sn_{23}$ and $Ho_7Co_6Sn_{23}$ are

3.3512(5) Å and 3.3426(10) Å for respectively. While the *Ln*1-Sn5 (x 6) distances are 3.3523(5) Å and 3.3446(9) Å for the Dy and Ho analogues respectively. *Ln*2 forms a truncated cuboctahedron with Sn atoms. A truncated cuboctahedron contains 10 atoms instead of 12, as shown in Figure 2.5b. A single atom takes the place of 3 missing atoms in the cuboctahedron. The *Ln*2-Sn bond distances range from 3.0803(7) to 3.3812(5) Å for $Dy_7Co_6Sn_{23}$ and from 3.0672(12) to 3.3707(8) Å for $Ho_7Co_6Sn_{23}$.

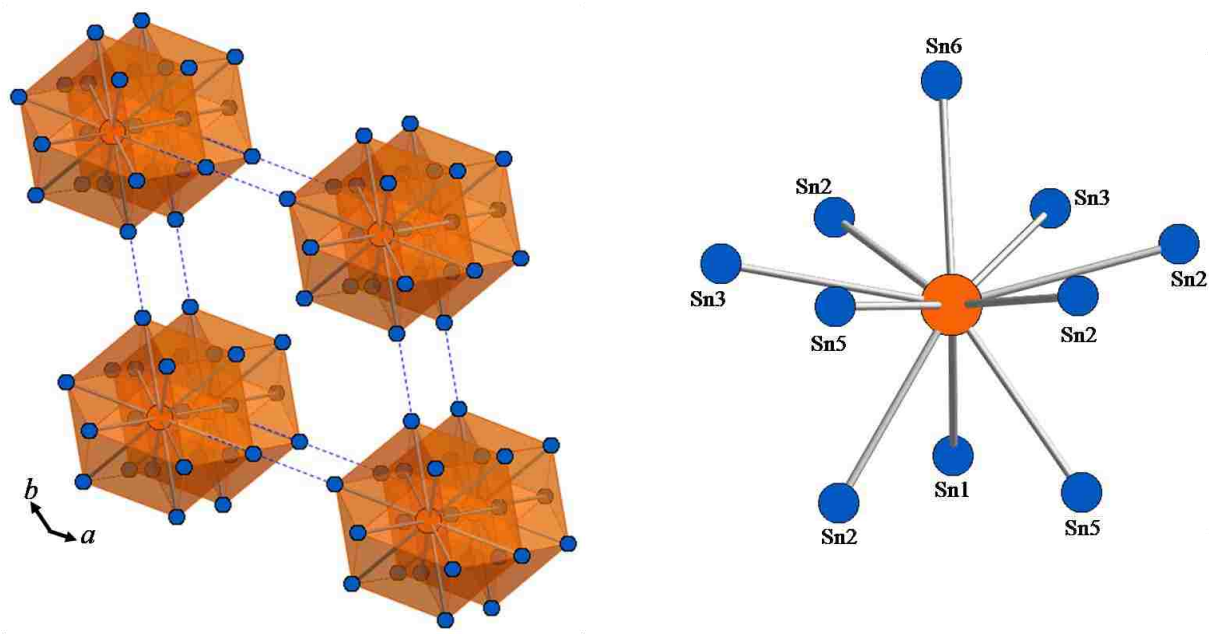

Figure 2.5 (a) The structure of *Ho*$_7$Co$_6$Sn$_{23}$ showing the Ho1Sn$_{12}$ cuboctahedra (orange) Sn atoms are blue spheres. (b) Projection of the Ho2Sn$_{10}$ truncated cuboctahedra of *Ho*$_7$Co$_6$Sn$_{23}$.

Table 2.10 Selected Interatomic Distance (Å) for $Ln_7Co_6Sn_{23}$ (*Ln* = Dy and Ho)

Compound	$Dy_7Co_6Sn_{23}$	$Ho_7Co_6Sn_{23}$
*Ln*1 cuboctahedron		
*Ln*1-Sn3 (x 6)	3.3512(5)	3.3426(10)
*Ln*1-Sn5 (x 6)	3.3523(5)	3.3446(9)

Table 2.10 cont

*Ln*2 truncated cuboctahedron		
*Ln*2-Sn1	3.3812(5)	3.3707(8)
*Ln*2-Sn2 (x 2)	3.1079(4)	3.0967(7)
*Ln*2-Sn2 (x 2)	3.2332(5)	3.2223(9)
*Ln*2-Sn3 (x 2)	3.1970(4)	3.1886(8)
*Ln*2-Sn5 (x 2)	3.3789(4)	3.3670(7)
*Ln*2-Sn6	3.0803(7)	3.0672(12)
Sn4 octahedron		
Sn4-Sn3 (x 6)	2.9582(5)	2.9509(10)
Co trigonal prism		
Co-Sn1	2.7645(10)	2.7561(19)
Co-Sn2	2.6598(12)	2.653(2)
Co-Sn3 (x 2)	2.6076(8)	2.6043(15)
Co-Sn5 (x 2)	2.5793(8)	2.5711(14)

The manner in which the transition metal-Sn trigonal prisms are connected is believed to lead to the formation of a particular structure (Phase I, I′, II, II′)[14] by forming cuboctahedral and/or icosahedral holes. Likewise, the Co trigonal prisms in $Ln_7Co_6Sn_{23}$ (Figure 2.6) also form cuboctahedral, truncated cuboctahedral and octahedral holes for the *Ln*1, *Ln*2 and Sn4 atoms respectively.[33, 34] In $Ln_7Co_6Sn_{23}$, the Co atoms are bonded to 4 different crystallographic Sn atoms (Sn1, Sn2, Sn3 (x 2) and Sn5 (x 2)) forming a trigonal prism. The longer Co-Sn distances range from 2.5793(8) Å to 2.7645(10) Å and 2.5711(14) Å to 2.7561(19) Å for the $Dy_7Co_6Sn_{23}$ and $Ho_7Co_6Sn_{23}$ compounds, respectively. The Co-Sn bond distances are slightly greater than the sum of their respective covalent radii (Co 1.25 Å and Sn 1.40 Å).[39] However, the Co-Sn bond distances are similar to those observed in $CoSn_2$ (2.737 Å).[40] In $Ln_7Co_6Sn_{23}$, Sn4 is bonded to six Sn3 atoms to form octahedra, as shown in Figure 2.7, with interatomic distances of 2.9582(5) Å (x6) and 2.9520(4) Å (x6) for *Ln* = Dy and Ho respectively. The shorter Sn4-Sn3 bond distances observed in $Ln_7Co_6Sn_{23}$ are similar to the Sn-Sn distances observed in α-$CoSn_3$ (2.961 Å), β-$CoSn_3$ (2.963 Å),[41] and to the "anion-like" Sn interatomic distances observed in and

$Er_5Rh_6Sn_{18}$ (2.967 Å).[14] The Sn4 octahedra are face-sharing with two cuboctahedra and edge sharing with $CoSn_6$ trigonal prisms

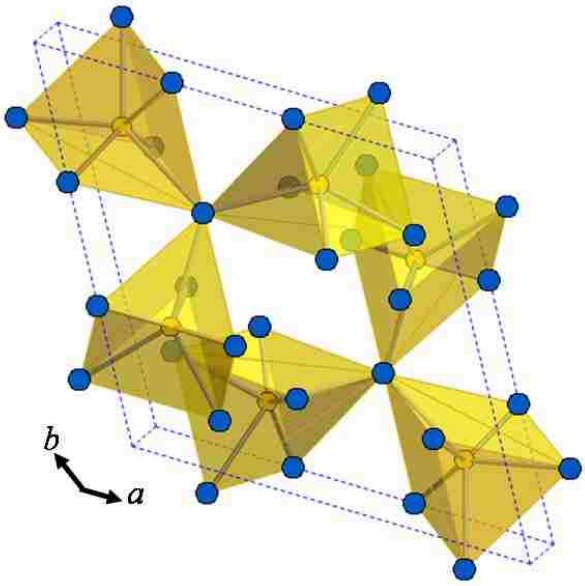

Figure 2.6 Projection of the $CoSn_6$ trigonal prisms (gold) of $Ho_7Co_6Sn_{23}$. Sn atoms are shown as blue spheres.

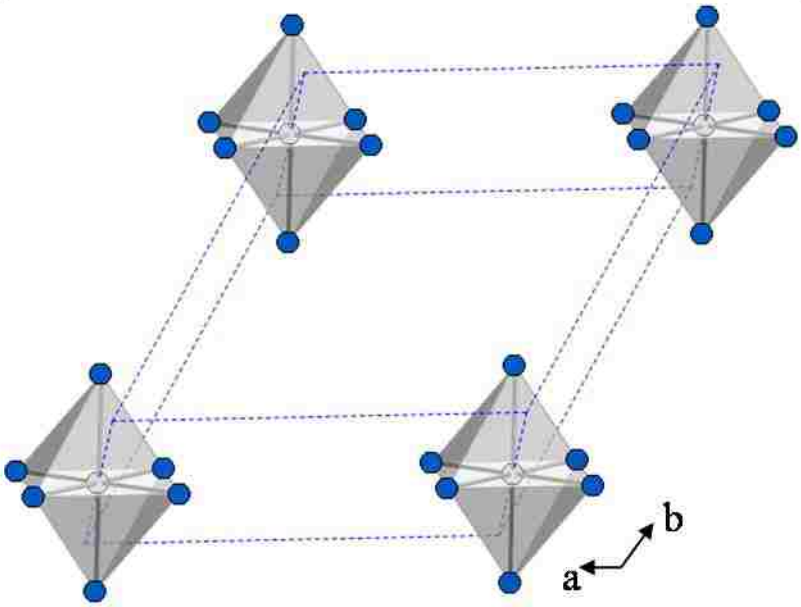

Figure 2.7 Projection of the Sn octahedra (Silver) of $Ho_7Co_6Sn_{23}$. Sn atoms are shown as blue spheres.

2.3.4 Structure of $Ln_5Co_6Sn_{18}$ (*Ln* = Er, Tm)

$Ln_5Co_6Sn_{18}$ (*Ln* = Er, Tm), crystallize in the $Sn_{1-x}Er_xEr_4Rh_6Sn_{18}$ structure type in space group $I4_1/acd$ with $Z = 8$.[2] The structure of $Er_5Co_6Sn_{18}$ consists of four different polyhedral units: *Ln*1cuboctahedra, *Ln*2 truncated cuboctahedra, and two different Co trigonal prisms. A list of selected bond distances is given in Table 2.11.

Table 2.11. Selected Interatomic Distances (Å) for $Ln_5Co_6Sn_{18}$ (*Ln* = Er, and Tm)

Polyhedra	$Er_5Co_6Sn_{18}$	$Tm_5Co_6Sn_{18}$
Co1 trigonal prism		
Co1-Sn4 (x 2)	2.717(3)	2.713(4)
Co1-Sn5 (x 2)	2.5792(17)	2.579(3)
Co1-Sn6 (x 2)	2.5986(17)	2.599(3)
Co2 trigonal prism		
Co2-Sn1	2.590(2)	2.590(3)
Co2-Sn2	2.590(2)	2.589(3)
Co2-Sn4 (x 2)	2.703(2)	2.698(3)
Co2-Sn5	2.586(2)	2.587(3)
Co2-Sn6	2.569(2)	2.572(3)
*Ln*1 cuboctahedra		
*Ln*1-Sn1 (x 2)	3.2863(16)	3.286(2)
*Ln*1-Sn2 (x 2)	3.3310(16)	3.325(2)
*Ln*1-Sn5 (x 4)	3.2898(10)	3.2888(15)
*Ln*1-Sn6 (x 4)	3.3093(11)	3.3100(16)
*Ln*2 truncated cuboctahedra		
Er2-Sn1 (x 2)	3.2209(10)	3.2188(14)
Er2-Sn2	3.2344(10)	3.2336(14)
Er2-Sn3	3.0460(14)	3.043(2)
Er2-Sn4	3.1430(11)	3.1367(17)
Er2-Sn4	3.1622(12)	3.1534(17)
Er2-Sn4	3.1646(11)	3.1585(17)
Er2-Sn5	3.2452(12)	3.2414(18)
Er2-Sn5	3.2455(12)	3.2424(18)
Er2 Sn6	3.1984(12)	3.1950(18)

*Ln*1 forms a distorted cuboctahedron with 12 Sn atoms [Sn1(x 2), Sn2 (x 2), Sn5 (x 4), and Sn6 (x 4)] as shown in Figure 2.8a. The *Ln*1 atoms occupy a "cage" created by the

arrangement of the $CoSn_6$ trigonal prisms.[14] The *Ln*(1)Sn_{12} cuboctahedra are face sharing with two Co(2)Sn_6 trigonal prisms, one on the top of the cuboctahedron and the other at the bottom, and four Co(1)Sn_6 trigonal prisms which are also face sharing.[14] The *Ln*(1)-Sn bond distances are 3.2863(16) Å (x2), 3.3310(16) Å (x2), 3.2898(10) Å (x4), and 3.3093(11) Å (x4) for $Er_5Co_6Sn_{18}$ and 3.286(2) Å (x2), 3.325(2) Å (x2), 3.2888(15) Å (x4), and 3.3100(16) Å (x4) for $Tm_5Co_6Sn_{18}$. The *Ln*-Sn bond distances in the above compounds are comparable to the *Ln*-Sn bond distance observed in $Ln_7Co_6Sn_{23}$ (*Ln* = Dy, Ho) and $Ln_3Co_4Sn_{13}$ (*Ln* = Pr, Nd, Sm, Gd and Tb).[21]

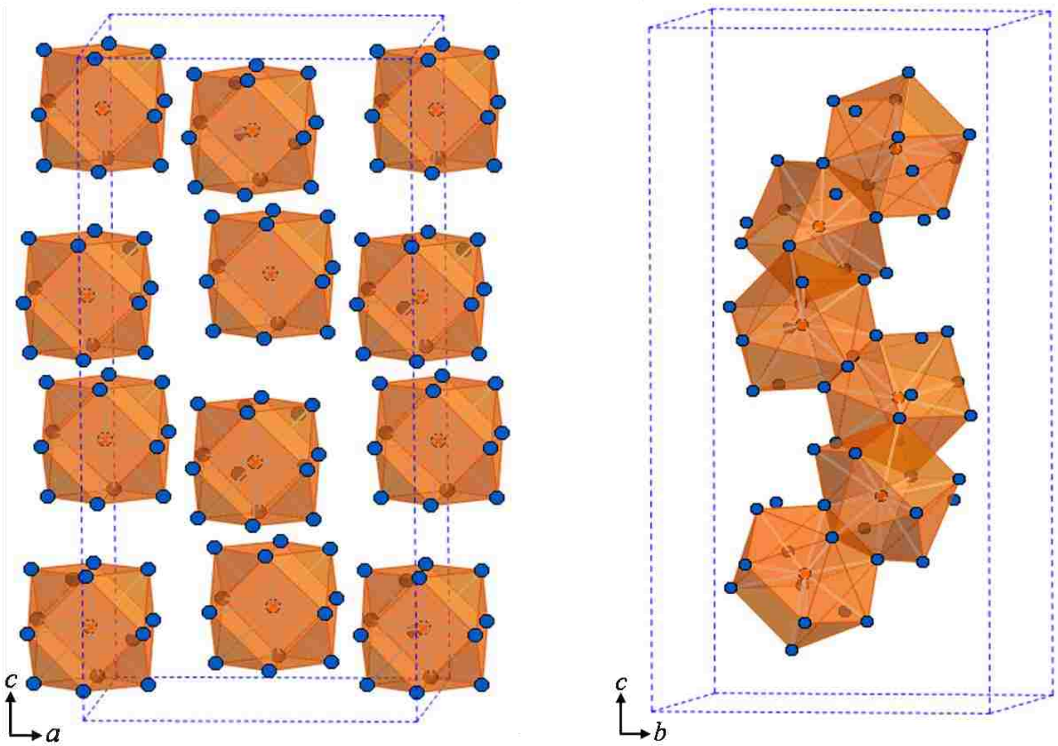

Figure 2.8 (a) Projection of the structure of $Er_5Co_6Sn_{18}$ showing the Er1$(Sn)_{12}$ cuboctahedra (orange). (b) Projection of the *Ln*2 truncated cuboctahedra (orange) of $Er_5Co_6Sn_{18}$.

$Ln_5Co_6Sn_{18}$ (*Ln* = Er, Tm) also contains *Ln*2 truncated cuboctahedra as shown in Figure 2.8b. The truncated cuboctahedra is formed by *Ln*2 sharing 9 Sn atoms [Sn1, Sn2, Sn4 (x3), Sn5 (x2), and Sn6] from the $CoSn_6$ trigonal prisms and a tenth Sn atom (Sn3). Like the *Ln*1

cuboctahedra, the *Ln*2 truncated cuboctahedra are also face sharing with the $CoSn_6$ trigonal prisms in addition to being edge sharing with *Ln*1 cuboctahedra. The *Ln*2-Sn bond distances range from 3.0460(12) to 3.2209(10) Å and 3.043(2) to 3.2188(14) Å for the Er and Tm analogues, respectively (Table 2.11). The arrangement of the $CoSn_6$ trigonal prisms in $Er_5Co_6Sn_{18}$ is shown in Figure 2.9. This arrangement is similar to that of the single crystal structure of $Sn_{1-x}Er_xEr_4Rh_6Sn_{18}$ reported by Hodeau *et. al*, in which the trigonal prisms are described as layers of corner sharing $RhSn_6$ trigonal prisms arranged in a "star" formation.[14] In the structure of $Er_5Co_6Sn_{18}$, the Co1 and Co2 atoms are arranged in layers separated by Sn atoms. Each Co atom is bonded to six Sn atoms forming a trigonal prism (Figure 2.9). This arrangement allows 2 Co1 trigonal prisms to share vertices with four Co2 prisms along the [100], [010], and [001] directions.[14]

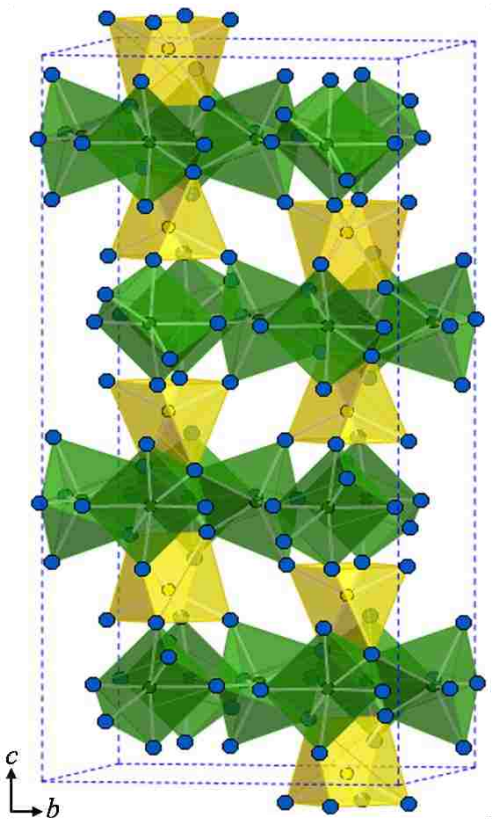

Figure 2.9 The structure of $Er_5Co_6Sn_{18}$ showing the $Co1Sn_6$ (gold) and $Co2Sn_6$ (green) trigonal prisms. Sn atoms are red spheres. *Ln* atoms have been removed for clarity.

The arrangement of the $CoSn_6$ trigonal prisms create holes occupied by *Ln*1 and *Ln*2. The distances between the Co1 and Sn atoms range from 2.5792(17) to 2.717(3) Å for $Er_5Co_6Sn_{18}$, and 2.579(3) to 2.713(4) Å for $Tm_5Co_6Sn_{18}$. Co2-Sn distances range from 2.590(2) to 2.703(2) Å for $Er_5Co_6Sn_{18}$, and 2.590(3) to 2.698(3) Å for $Tm_5Co_6Sn_{18}$. The above distances are similar to that observed in the $Ln_3Co_4Sn_{13}$ (*Ln* = Pr, Nd, Sm, Gd and Tb) compounds where Co is bonded to six equivalent Sn atoms (Sn2), with bond distances ranging from 2.6073(3) Å to 2.5878(4) Å for Pr to Tb.[21]

2.3.5 Structural Comparisons

The size and oxidation number of the rare-earth metal is believed to influence the formation of a particular phase in the *Ln*-*M*-Sn system. In $Yb_3Rh_4Sn_{13}$, Yb is divalent and thus has a relatively larger ionic radius which allows for the formation of the cubic ($Pm\bar{3}n$) Phase I structure.[11, 16] However, when pressure is applied to the structure, the Yb ion can be changed from a divalent state to a mixed valent state, thus transforming the structure to the cubic ($Fm\bar{3}m$) Phase III $a \sim 13$ Å structure type.[16] Smaller rare-earth metals tend to form either the tetragonal Phase II or the cubic Phase III compounds. An understanding of the bonding in the various cuboctahedra may lead to a better understanding of the transition from one phase to another.

In the compounds $Ln_3Co_4Sn_{13}$ (*Ln* = Pr, Nd, Sm, Gd and Tb), $Ln_7Co_6Sn_{23}$ (*Ln* = Dy, Ho) and $Ln_5Co_6Sn_{18}$ (*Ln* = Er, Tm), the $LnSn_{12}$ cuboctahedra have bond distances that are comparable to the sum of the atomic radii of their respective rare-earth and Sn,[39] however, the differences in the various cuboctahedral units lie in the way they are distorted. Table 2.12 is a comparison of the bond distances and bond angles of $Ln_3Co_4Sn_{13}$, $Ln_7Co_6Sn_{23}$ and $Ln_5Co_6Sn_{18}$.

Table 2.12 Comparison of Interatomic Distances Between $Ln_3Co_4Sn_{13}$, $Ln_7Co_6Sn_{23}$ and $Ln_5Co_6Sn_{18}$

[LnSn$_{12}$] Cuboctahedra Interatomic Distances (Å)

$Ln_3Co_4Sn_{13}$		$Ln_7Co_6Sn_{23}$		$Ln_5Co_6Sn_{18}$	
Pr-Sn2 (x 4)	3.3974(5)	Dy1-Sn3 (x 6)	3.3512(5)	Er1-Sn1 (x 2)	3.326(2)
Pr-Sn2 (x 8)	3.3278(7)	Dy1-Sn5 (x 6)	3.3523(5)	Er1-Sn1 (x 2)	3.326(2)
				Er1-Sn5 (x 4)	3.3096(15)
				Er1-Sn6 (x 4)	3.2884(15)

[CoSn$_6$] trigonal prisms Interatomic Distances (Å)

$Ln_3Co_4Sn_{13}$		$Ln_7Co_6Sn_{23}$		$Ln_5Co_6Sn_{18}$	
Co-Sn2(x 6)	2.6073(3)	Co-Sn1	2.7645(10)	Co1-Sn4 (x 2)	2.717(3)
		Co-Sn2	2.6598(12)	Co1-Sn5 (x 2)	2.5792(17)
		Co-Sn3 (x 2)	2.6076(8)	Co1-Sn6 (x 2)	2.5986(17)
		CoSn5 (x 2)	2.5793(8)		
				Co2-Sn1	2.572(3)
				Co2-Sn2	2.590(3)
				Co2-Sn4 (x 2)	2.589(3)
				Co2-Sn5	2.698(3)

The cuboctahedra in the $Ln_7Co_6Sn_{23}$ (Ln = Dy, Ho) compounds are less distorted, with the Ln1-Sn3 and Ln1-Sn5 bond distances in the range of ~ 3.3512(5) Å and ~ 3.3523(5) Å, and the Sn3-Ln1-Sn3 and Sn5-Ln1-Sn5 bond angles almost the same ~ 60.969(15)º and ~ 60.09º. In comparison, the cuboctahedra in $Ln_3Co_4Sn_{13}$ (Ln = Pr, Nd, Sm, Gd and Tb) and $Ln_5Co_6Sn_{18}$ (Ln = Er, Tm) show more distortion. The Ln-Sn bond distances range from 3.3278(7) Å to 3.3974(5) Å and 3.2884(15) Å to 3.326(2) Å for the $Ln_3Co_4Sn_{13}$ and $Ln_5Co_6Sn_{18}$ structure types, respectively Their respective bond angles are between ~ 63.962(2)º - 63.744(11)º for $Ln_3Co_4Sn_{13}$ (Ln = Pr, Nd, Sm, Gd and Tb) and ~ 60.442(16)º - 62.63(2)º for $Ln_5Co_6Sn_{18}$ (Ln = Er, Tm). Thus, the distortion in the compound $Ln_5Co_6Sn_{18}$ is a result of both bond distances and bond angles compared to $Ln_3Co_4Sn_{13}$ (Ln = Pr, Nd, Sm, Gd and Tb) which is distorted only by the ratios of bond distances.[21] The compounds $Ln_7Co_6Sn_{23}$ (Ln = Dy, Ho) show a distortion closest to unity. The trigonal prisms have similar bond distances and corresponding bond angles

(Table 2.12). The trigonal prisms contained in the $Ln_3Co_4Sn_{13}$ compounds have the same bond distances ~ 2.6073 Å and bond angles ~ 86.12º.[21] However, the trigonal prisms in $Ln_7Co_6Sn_{23}$ and $Ln_5Co_6Sn_{18}$ exhibit distortion with the Co-Sn bond distances ranging from ~2.579 Å to 2.7645 Å for $Ln_7Co_6Sn_{23}$ and corresponding bond angles of ~ 75.26(2)º to 86.92(4)º. The Co trigonal prisms in $Ln_5Co_6Sn_{18}$ manifests the most distortion with the $Co1Sn_6$ trigonal prism bond distances ranging from 2.5792(5) Å to 2.717(2) Å and bond angles between ~ 86.17º(4) and 78.59(6)º. The $Co2Sn_6$ trigonal prisms show a great deal of distortion in the Sn-Co-Sn bond angles which are between ~ 50.68(7)º to 78.81(2)º and the Co-Sn bond distances which are between 2.572(5) Å to 2.701(2) Å. Thus, as a function of rare-earth metals, there seems to be more distortion in the $CoSn_6$ trigonal prisms with compounds containing heavier rare-earth elements compared to lighter rare-earth elements.

2.3.6 Physical Properties of $Ln_3Co_4Sn_{13}$ (*Ln* = Pr, Nd, Sm, Gd and Tb)

The temperature dependent magnetic susceptibility of $Ln_3Co_4Sn_{13}$ (*Ln* = Pr, Nd, Sm, Gd and Tb) for an applied field of 0.1 T is shown in Figure 2.10. $Pr_3Co_4Sn_{13,}$ $Sm_3Co_4Sn_{13}$, $Gd_3Co_4Sn_{13}$, and $Tb_3Co_4Sn_{13}$ all show antiferromagnetic transitions at 2.31 K, 6.6 K, 12.5 K, and 10.8 K respectively whilst the compound $Nd_3Co_4Sn_{13}$ shows paramagnetic ordering down to a low temperature of 1.8 K. A linear fit to the inverse susceptibility data was used to obtain the effective magnetic moments of $Ln_4Co_3Sn_{13}$ (Pr, Nd, Sm, Gd and Tb). All the compounds obey Curie-Weiss law ($\chi = C/(T- \theta)$ with θ values of -7.4, -27.2, -27.5,-24.4 and -17.3 for Pr, Nd, Sm, Gd and Tb analogues respectively. The negative values of the Weiss constants indicate the antiferromagnetic nature of $Pr_3Co_4Sn_{13,}$ $Sm_3Co_4Sn_{13}$, $Gd_3Co_4Sn_{13}$, and $Tb_3Co_4Sn_{13}$. The negative value for $Nd_3Co_4Sn_{13}$ suggests antiferromagnetic behavior for the compound. The experimental effective moments were 3.25 μ_B, 3.51 μ_B, 0.68 μ_B, 7.93 $\mu_{B,}$ and 10.44 μ_B for the Pr, Nd, Sm, Gd,

and Tb analogues, respectively. These values are close to the expected values for their Ln^{3+} free ions.

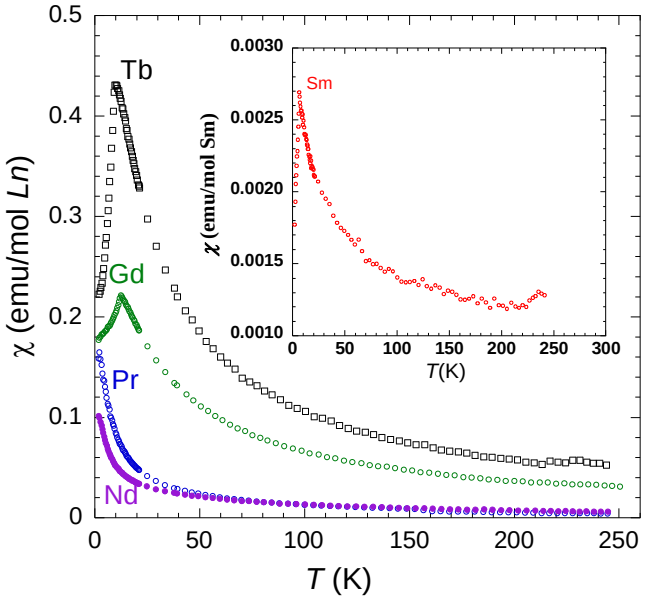

Figure 2.10 Magnetic susceptibility (χ) for $Ln_3Co_4Sn_{13}$ (*Ln* = Pr, Nd, Sm, Gd, Tb) at an applied field of 0.1 T.

The field dependence of magnetization taken at 3 K is shown in Figure 2.11. Apart from $Gd_3Co_4Sn_{13}$, which shows a linear dependence of magnetization with increasing field, the other analogues show signs of saturation below their respective saturation moments. Figure 2.12 shows a plot of electrical resistivity (ρ) as a function of temperature for $Ln_3Co_4Sn_{13}$ (*Ln* = Pr, Nd, Sm, Gd and Tb). The plots indicate metallic behavior for each compound, as the resistivity increases with increasing temperature. This phenomena is similar to the analogues containing the transition metals Rh and Ir where the Ce analogues are semiconducting and the rare-earth analogues with *Ln* =Pr, Nd, Sm and Gd, display metallic behavior.[6, 20] Dips are observed in the resistivity plots of $Pr_3Co_4Sn_{13}$, $Nd_3Co_4Sn_{13}$ and $Tb_3Co_4Sn_{13}$ at 3.7 K. The dips are likely due to Sn (T_c ~ 3.7 K) inclusions in the aforementioned single crystals. The Nd-analogue shows the lowest resistivity at room temperature with a value ~104.52 μΩ-cm. The residual resistivity

ratios (RRR = ρ_{298K}/ρ_{2K}) for $Ln_3Co_4Sn_{13}$ (*Ln* = Pr, Nd, Sm, Gd and Tb) are 2.13, 2.30, 1.26, 2.58 and 1.55, respectively.

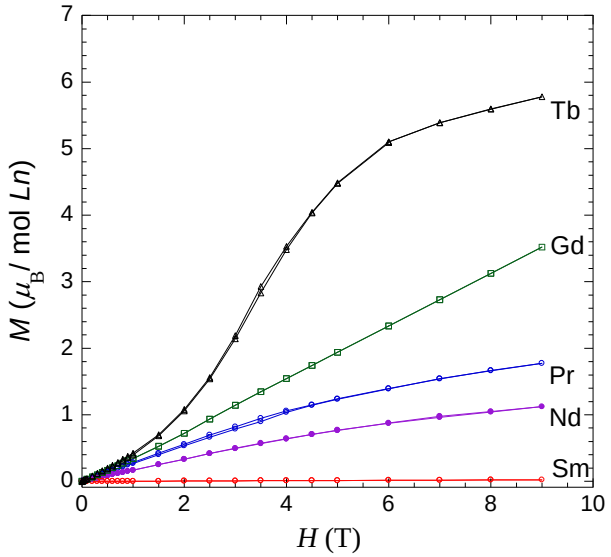

Figure 2.11 Field dependent magnetization M (H) at 3 K for $Ln_3Co_4Sn_{13}$ (*Ln* = Pr, Nd, Sm, Gd, and Tb).

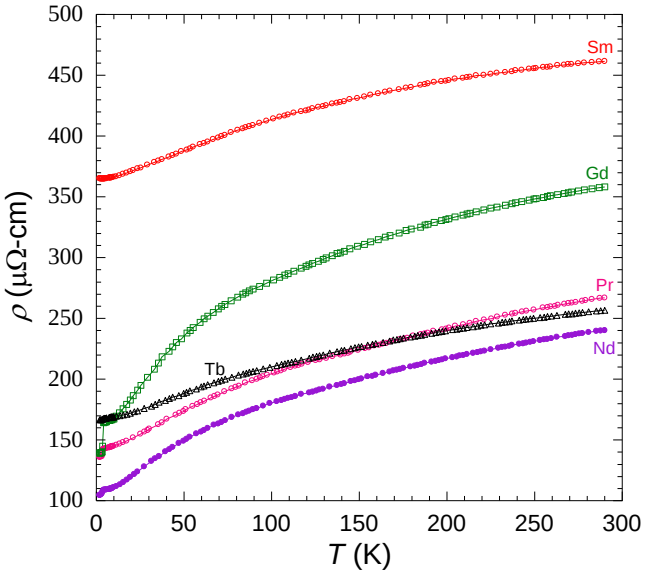

Figure 2.12 Resistivity as a function of temperature for $Ln_3Co_4Sn_{13}$ (*Ln* = Pr, Nd, Sm, Gd,and Tb)

2.3.7 Physical Properties of $Yb_3Co_4Sn_{12.79}$

As stated earlier the physical properties of $Yb_3Co_4Sn_{12+x}$ (x = 0.79 and 0.90) do not change with composition, thus we report the physical properties of $Yb_3Co_4Sn_{12.79}$ in this

dissertation. Figure 2.13a shows the temperature dependence of electrical resistivity (ρ) between 2 and 350 K at both zero field and 8 Tesla for a single crystal of $Yb_3Co_4Sn_{12.79}$. In both cases, the resistivity decreases with decreasing temperature reflecting metallic behavior. At high temperatures, it varies more or less linearly with temperature. Below ~ 150 K, ρ(T) departs slowly from high-temperature behavior, *i.e.*, decreasing faster than the high-temperature case. While there is small upturn below ~ 10 K under 8 Tesla (Figure 2.13d), a sharp drop occurs in the zero-field resistivity at T_c = 3.8 K (Figure 2.13c). Although polycrystalline sample showed similar character in zero-field resistivity,[14] we note several differences: (1) the resistivity ratio ρ(4K)/ρ(300K) ~ 0.36 for our single crystal, considerably smaller than that of polycrystalline sample; (2) there is no sign of saturation of ρ(T) up to at least 350 K (Figure 2.13a); (3) the step-like resistivity drop (Figure 2.13c) suggests filamentary superconductivity in single crystals of $Yb_3Co_4Sn_{12.79}$, in contrast with bulk superconductivity observed in the polycrystalline sample.[14]

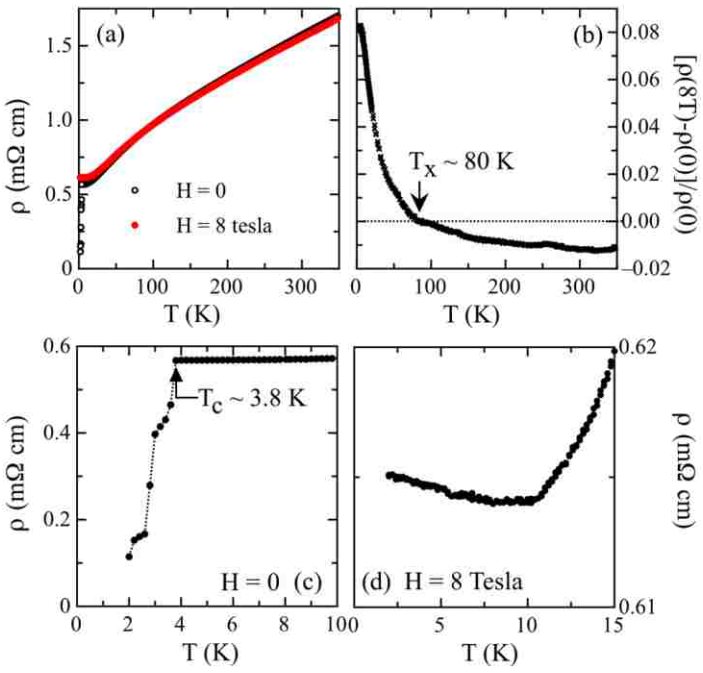

Figure 2.13 (a) Temperature-dependent electrical resistivity of $Yb_3Co_4Sn_{12.79}$ at H = 0 and H = 8 T (b) The temperature-dependent magnetoresistance of $Yb_3Co_4Sn_{12.79}$ (c) A zoomed portion of the electrical resistivity of $Yb_3Co_4Sn_{12.79}$ (d) Low temperature resistivity of $Yb_3Co_4Sn_{12.79}$ at H = 8 T.

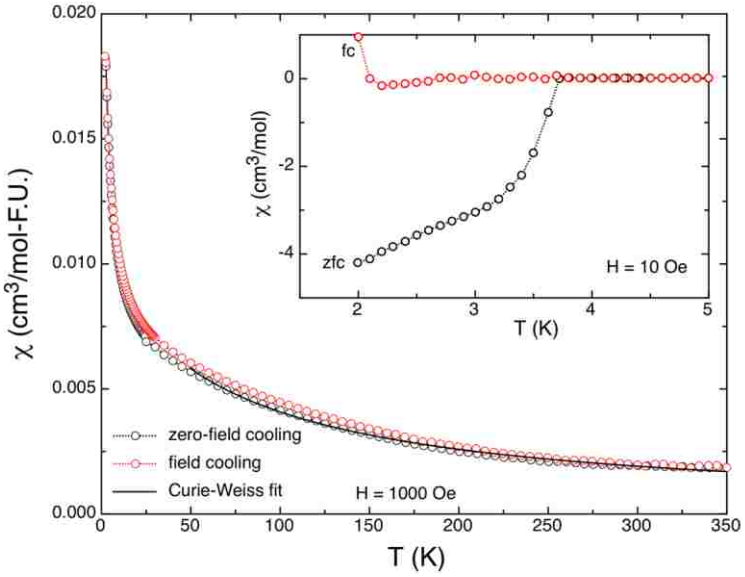

Figure 2.14 Zero- field cooled (black circles) and field cooled (red circles) magnetic susceptibility (χ) of $Yb_3Co_4Sn_{12.79}$ at H = 0.1 T. The inset shows a zoomed portion of the magnetic susceptibility at H = 0.001 T.

In order to elucidate the origin of the anomalies observed in the electrical resistivity, the temperature dependent magnetic susceptibility of $Yb_3Co_4Sn_{12.79}$ was investigated. Figure 2.14 shows the zero-field-cooling (zfc) and field-cooling (fc) magnetic susceptibility of $Yb_3Co_4Sn_{12.79}$ at H = 1000 Oe. The magnetic susceptibility increase with decreasing temperature, without obvious hysteresis, suggesting that the system is paramagnetic without long-range magnetic ordering. However, both χ_{zfc} and χ_{fc} are apparently different when measured at 10 Oe as shown in the inset of Figure 2.14. Below T_c = 3.8 K, a diamagnetic signal is observed in χ_{zfc} and χ_{fc}. Note that $\chi_{zfc} << \chi_{fc}$, indicating that the superconducting volume is very small. As T_c is close to that of elemental Sn (T_c = 3.72 K), it is possible that there is Sn flux remaining in the crystals that contribute to the diamagnetism observed and provides a low-resistivity path. This is further confirmed by the field dependence of the magnetization at T = 1.8 K, as shown in Figure 2.15a. The upper critical field at 1.8 K is $H_{c2} \sim 290$ Oe, close to that for Sn.

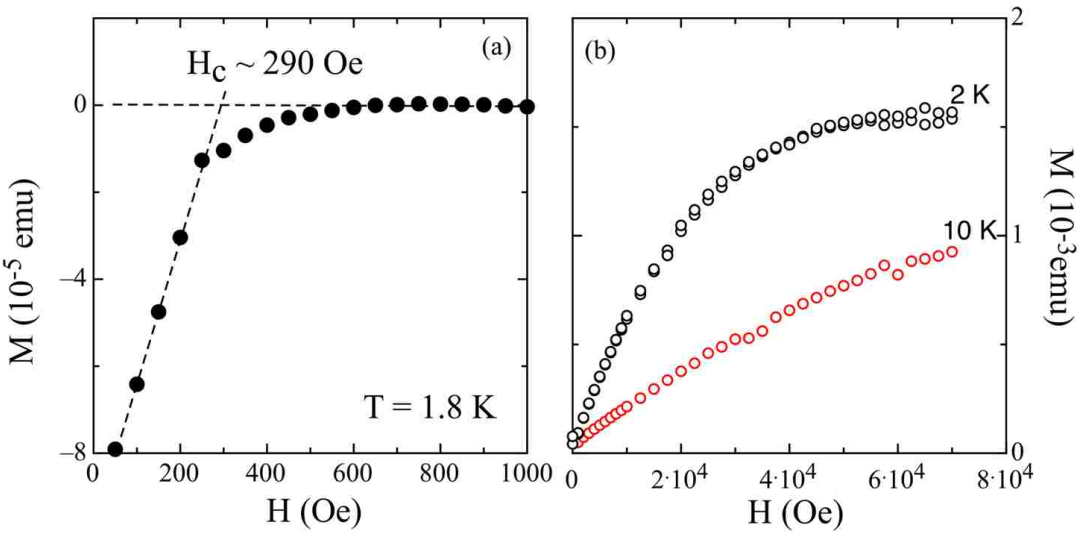

Figure 2.15 Field-dependent magnetization, M (H), of $Yb_3Co_4Sn_{12.79}$ at (a) T = 1.8 K and (b) T = 3 K.

The intrinsic physical properties of $Yb_3Co_4Sn_{12.79}$ may be identified when the superconductivity of Sn inclusions is completely suppressed by applying a high magnetic field. Therefore, the magnetic susceptibility measured at 1000 Oe should reflect the magnetic behavior of $Yb_3Co_4Sn_{12.79}$ single crystals (Figure 2.14). Similar to the case for the polycrystalline sample, our magnetic susceptibility data between 50 and 350 K can be fit using Curie-Weiss law $\chi = \chi_0 + C/(T-\Theta_{CW})$, where χ_0 is the T-independent susceptibility, C is the Curie-Weiss constant, and Θ_{CW} is the Curie-Weiss temperature. As can be seen in Figure 2.14, the data is well described by the Curie-Weiss formula represented by the solid line, with $\chi_0 \sim 1.31\times10^{-4}$ cm^3/mol, C = 0.65 K cm^3/mol and Θ_{CW} ~ -64.2 K. The constant C gives an effective moment $\mu_{eff} \sim 2.27\mu_B$/formula unit or $0.75\mu_B$/Yb, where μ_B is the Bohr magneton. This is slightly smaller than that obtained from the polycrystalline sample ($1.1\mu_B$/Yb).[27] On the other hand, the value of Θ_{CW} for our single crystals is much larger than that for polycrystalline sample (-15 K), [14] implying stronger magnetic interactions in the former case. Nevertheless, the negative Θ_{CW} suggests antiferromagnetic (AFM) magnetic interactions. Such a system is expected to exhibit positive

magnetoresistance (MR), as the application of a magnetic field tends to reduce AFM interactions, resulting in an increase in spin scattering. Surprisingly, the temperature dependence MR shown in Figure 2.13b indicates that MR is negative at high temperatures but positive below ~ 80 K. This suggests that the magnetic interactions are more complicated than a simple antiferromagnet. This is further evident by the low-temperature M(H) of $Yb_3Co_4Sn_{12.79}$ single crystals shown in Figure 2.15b. M deviates from linearity, and tends to saturate in high fields at 2 and 10 K, suggesting that ferromagnetic (FM) type magnetic interactions are dominant at low temperatures and high fields.

As introduced earlier, many Remeika compounds exhibit heavy fermion behavior at low temperatures. Figure 2.16 shows the temperature dependence of specific heat (C_p) of $Yb_3Co_4Sn_{12.79}$ single crystals between 1.8 and 200 K. As expected, specific heat decreases with decreasing temperature, without an apparent anomaly over the entire temperature range. For clarity, we replot the low-temperature (1.8 to 10 K) specific heat data as C_p/T versus T^2 in the inset for $Yb_3Co_4Sn_{12.79}$. The absence of a specific heat peak at T_c is consistent with the picture of filamentary superconductivity, but a small anomaly is observed at 2.3 K which may be attributed to a small amount of Yb_2O_3 impurity, as suggested in Ref. [27].[27] This is also consistent with the upturn observed in the χ_{fc} susceptibility shown in the inset of Figure 2.14. Nevertheless, the the application of 8 T field suppresses the low-temperature specific heat anomaly (see the inset of Figure 2.16). The specific heat data cannot be fitted well by $C_p/T = \gamma + \beta_3 T^2$ (β_3 is a constant), as C_p/T versus T^2 is not linear. We therefore fit the low-temperature specific heat using $C_p(8T)/T = \gamma + \beta_3 T^2 + \beta_5 T^4$, where the second and third terms describe phonon contributions (β_5 is a constant). From the results we obtain γ value ~ 44.5 mJ/mol (F.U.)-K^2, and a Debye temperature

Θ_D = 182.8 K obtained through relationship $\beta_3 = \frac{12\pi^4 RN}{5\Theta_D^3}$ (R = 8.314 J/mol K, and N is the number of atoms per formula), similar to that of the polycrystalline sample reported in Ref. [27].

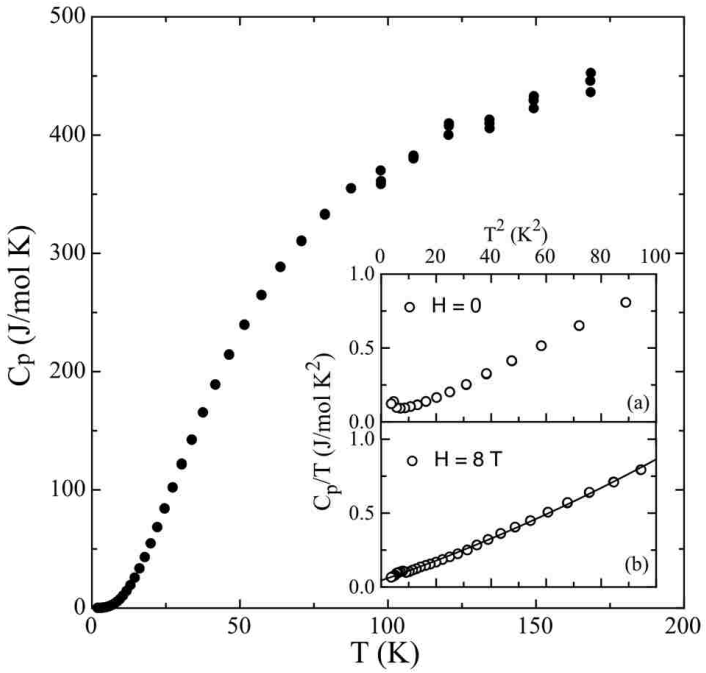

Figure 2.16. Zero-field specific heat of $Yb_3Co_4Sn_{12.79}$ as a function of temperature. The inset shows C_p/T vs.T^2 at (a) H = 0 and (b) H = 8 T.

As reported previously the magnetism in $Ln_3Co_4Sn_{13}$ (*Ln* =Ce-Nd, Sm, Gd and Tb)[20, 21] compounds is influenced by the lanthanide ion and Co is nonmagnetic in the structure. The calculated effective moment of Yb in $Yb_3Co_4Sn_{12.79}$ is ~ 0.75 μ_B implying that the oxidation state of Yb is close to a 2+ oxidation state. The Yb-Sn2 distances (Table 2.19) for $Yb_3Co_4Sn_{12.79}$ and $Yb_3Co_4Sn_{12.90}$ are well within σ^2 standard deviation, indicating the interatomic distances in both compounds are similar. The similarity in bond distance can account for the similarities observed in the magnetic properties of single crystals of and $Yb_3Co_4Sn_{12.79}$ and $Yb_3Co_4Sn_{12.90}$ (not shown).

The H_c value obtained from the polycrystalline sample reported by Mudryk et al. was calculated using the relationship $\gamma T_c^2 / H_c^2(0) = 0.168$, which obtained a H_c value of 2.5 T.[27] using the same relationship and values from our specific heat and resistivity data yield an *H*c value of

3.8 T. The upper critical field obtained from field dependent magnetization experiments at 1.8 T is 0.29 Oe. Mudryk et al. did not perfume field dependent magnetization experiments to determine H_c as we did. Also we have demonstrated that the superconductivity observed in single crystals of $Yb_3Co_4Sn_{12.79}$, is granular and results from Sn inclusions.

2.3.8 Physical Properties of $Ln_7Co_6Sn_{23}$ (*Ln* = Dy, Ho) and $Ln_5Co_6Sn_{18}$ (*Ln* = Er, Tm)

Figure 2.17 shows the temperature dependent inverse magnetic susceptibility ($1/\chi$) at an applied field of 0.1 T. Above 10 K, all of the compounds obey the Curie law, as they display a linear temperature dependence to their inverse susceptibility. Only $Dy_7Co_6Sn_{23}$ shows a signature of magnetic ordering below 10 K (Figure 2.17 inset), consistent with ferromagnetic (or possibly ferrimagnetic) ordering near 7 K. From linear fits to the data the effective magnetic moment for $Dy_7Co_6Sn_{23}$ and $Ho_7Co_6Sn_{23}$ are 9.21 and 9.72 μ_B, respectively. The reduction in the effective magnetic moments of the above compounds can be attributed to crystal field effects. A negative value of θ_{Weiss} = -7.2 K for $Dy_7Co_6Sn_{23}$ indicates that weak magnetic interactions exist between the local moments in this material. $Ho_7Co_6Sn_{23}$ has a θ_{Weiss} value close to zero.

Both $Er_5Co_6Sn_{18}$ and $Tm_5Co_6Sn_{18}$ are Curie paramagnets down to 2 K, with $\theta_{Weiss} \sim 0$ K obtained from the inverse susceptibility plot. The effective moments of $Er_5Co_6Sn_{18}$ and $Tm_5Co_6Sn_{18}$ are 8.82 and 7.90 μ_B, respectively. Although the effective moment of $Er_5Co_6Sn_{18}$ is not close to the calculated moment of Er^{3+} = 9.58 μ_B, the low value of 8.82 μ_B is similar to that observed in the reentrant superconductor $Er_5Rh_6Sn_{18}$, where the effective moment is ~ 8.66 μ_B.[31] This low value can be attributed to the doublet ground state close to the ±J state of Er^{3+} with J = 15/2 and g_J = 6/5.[31] Figure 2.18 shows the field dependent magnetization M (H) at 3 K for $Ln_7Co_6Sn_{23}$ (*Ln* = Dy, Ho) and $Ln_5Co_6Sn_{18}$ (*Ln* = Er, Tm), $Dy_7Co_6Sn_{23}$, $Ho_7Co_6Sn_{23}$, $Er_5Co_6Sn_{18}$, and $Tm_5Co_6Sn_{18}$ show signs of saturation at 5.71, 7.06, 6.62, and 3.04 μ_B, respectively well before their respective saturation moments. A plot of resistivity as a function of temperature for

$Ln_7Co_6Sn_{23}$ (*Ln* = Dy, Ho) and $Ln_5Co_6Sn_{18}$ (*Ln* = Er, Tm) is shown in Figure 2.19. All compounds exhibit metallic behavior, as resistivity increases with an increase in temperature. The residual resistivity ratios (RRR) for $Ln_7Co_6Sn_{23}$ (*Ln* = Dy, Ho) are 1.0 and 1.8. A transition is observed around 3.7 K for the $Ho_7Co_6Sn_{23}$, $Er_5Co_6Sn_{18}$ and $Tm_5Co_6Sn_{18}$ compounds. This transition can be attributed to impurities of Sn (T_c ~ 3.7 K), as no diamagnetic behavior was observed in the magnetization data.

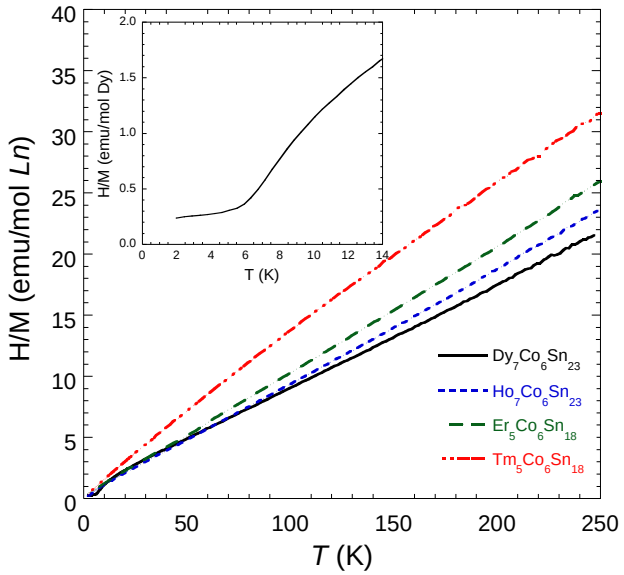

Figure 2.17 1/χ vs T for $Ln_7Co_6Sn_{23}$ (*Ln* = Dy, Ho) and $Ln_5Co_6Sn_{18}$ (*Ln* = Er, Tm). The inset shows the low temperature data for $Dy_7Co_6Sn_{23}$.

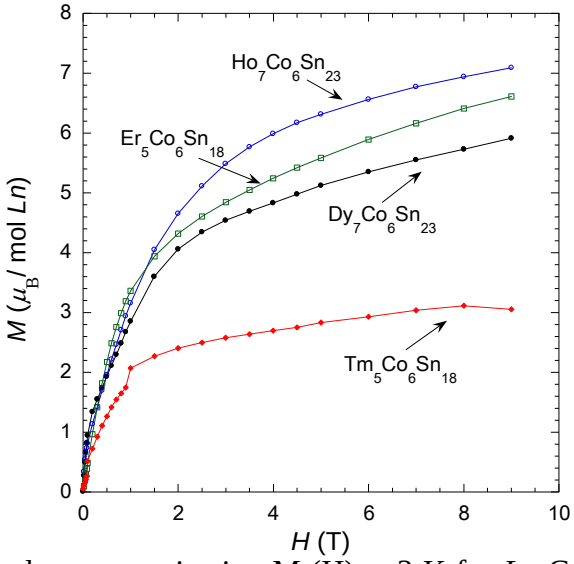

Figure 2.18 Field dependent magnetization M (H) at 3 K for $Ln_7Co_6Sn_{23}$ (*Ln* = Dy, Ho) and $Ln_5Co_6Sn_{18}$ (*Ln* = Er, Tm)

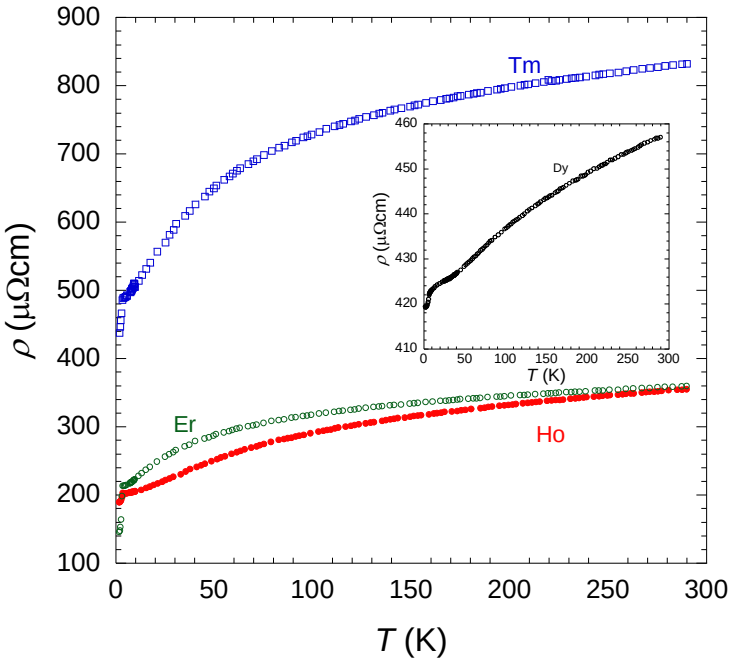

Figure 2.19 Plot of resistivity as a function of temperature for $Ln_7Co_6Sn_{23}$ (*Ln* = Dy, Ho) and $Ln_5Co_6Sn_{18}$ (*Ln* = Er, Tm).

2.4 References

(1) Remeika, J. P.; Espinosa, G. P.; Cooper, A. S.; Barz, H.; Rowell, J. M.; McWhan, D. B.; Vandenberg, J. M.; Moncton, D. E.; Fisk, Z.; Woolf, L. D.; Hamaker, H. C.; Maple, M. B.; Shirane, G.; Thomlinson, W., *Solid State Commun.* **1980,** *34*, 923-926.

(2) Espinosa, G. P.; Cooper, A. S.; Barz, H.; Remeika, J. P., *Mat. Res. Bull.* **1980,** *15*, 1635-1641.

(3) Lloret, B.; Chevalier, B.; Gravereau, P.; Darriet, B.; Etourneau, J., *J. Phys. I* **1988,** *49*, 487-488.

(4) Hodeau, J. L.; Marezio, M.; Pannetier, J.; Benoit, A., *Annales de Chimie (Paris, France)* **1984,** *9*, 1015-1018.

(5) Hodeau, J. L.; Bordet, P.; Wolfers, P.; Marezio, M.; Remeika, J. P., *J. Magn. Magn. Mater* **1986,** *54-57*, 1527-1528.

(6) Sato, H.; Fukuhara, T.; Iwakawa, S.; Aoki, Y.; Sakamoto, I.; Takayanagi, S.; Wada, N., *Physica B* **1993,** *188*, 630-632.

(7) Ghosh, K.; Ramakrishnan, S.; Chandra, G., *Phys. Rev. B* **1993,** *48*, 10435-10439.

(8) Takayanagi, S.; Sato, H.; Fukuhara, T.; Wada, N., *Physica B* **1994,** *199*, 49-51.

(9) Tomy, C. V.; Balakrishnan, G.; Paul, D. M., *Phys. Rev. B* **1997,** *56*, 8346-8350.

(10) Niepmann, D.; Pöttgen, R.; Poduska, K. M.; DiSalvo, F. J.; Trill, H.; Mosel, B. D., *Z.Naturforsch.(B)* **2001,** *56b*, 1-8.

(11) Hodeau, J. L.; Chenavas, J.; Marezio, M.; Remeika, J. P., *Solid State Commun.* **1980,** *36*, 839-845.

(12) Chenavas, J.; Hodeau, J. L.; Collomb, A.; Marezio, M.; Remeika, J. P.; Vandenberg, J. M., *Ternary Supercond., Proc. Int. Conf.* **1981**, 219-224.

(13) Vandenberg, J. M., *Mat. Res. Bull.* **1980,** *15*, 835-847.

(14) Hodeau, J. L.; Marezio, M.; Remeika, J. P., *Acta Crystallogr. Sect. B-Struct. Commun* **1984,** *40*, 26-38.

(15) Mirambet, F.; Chevalier, B.; Fournes, L.; Besnus, M. J.; Gravereau, P.; Etourneau, J., *J. Magn. Magn. Mater.* **1993,** *118*, 187-192.

(16) Jayaraman, A.; Remeika, J. P.; Espinosa, G. P.; Cooper, A. S.; Barz, H.; Maines, R. G.; Fisk, Z., *Solid State Commun.* **1981,** *39*, 1049-1051.

(17) Israel, C.; Bittar, E. M.; Agüero, O. E.; Urbano, R. R.; Rettori, C.; Torriani, I.; Pagliuso, P. G.; Moreno, N. O.; Thompson, J. D.; Hundley, M. F.; Sarrao, J. L.; Borges, H. A., *Physica B* **2005,** *359*, 251-253.

(18) Cooper, A. S., *Mat. Res. Bull.* **1980,** *15*, 799-805.

(19) Skolozdra, R. V.; Yasnitskaya, I. V.; Koretskaya, O. E.; Aksel'rud, L. G., *Dopov. Akad. Nauk Ukr. RSR, Ser. B* **1983,** *6*, 42-45.

(20) Thomas, E. L.; Bankston, A. N.; Lee, H.-O.; MaQuilon, S.; Moldovan, M.; Young, D. P.; Chan, J. Y., *J. Solid State Chem.* **2006,** *179*, 1641-1648

(21) Thomas, E. L.; Millican, J. N.; Okudzeto, E. K.; Chan, J. Y., *Comments Inorg. Chem.* **2006,** *27*, 1-39.

(22) Marezio, M., *Rev. Real Acad. Cienc. Exact. Fís. Natur. Madrid* **1986,** *80*, 293-306.

(23) Espinosa, G. P.; Cooper, A. S.; Barz, H., *Mat. Res. Bull.* **1982,** *17*, 963-969.

(24) Lloret, B.; Chevalier, B.; Lejay, P.; Etourneau, J., *C.R. Acad. Sci., Ser. II* **1986,** *303*, 1193-1195.

(25) Westerveld, J. P. A.; Lo Cascio, D. M. R.; Bakker, H.; Loopstra, B. O.; Goubitz, K., *J. Phys. Condens. Matter* **1989,** *1*, 5689-5702.

(26) Ghosh, K.; Ramakrishnan, S.; Dhar, S. K.; Malik, S. K.; Chandra, G.; Pecharsky, V. K.; Gschneidner, K. A., Jr.; Hu, Z.; Yelon, W. B., *Phys. Rev. B* **1995,** *52*, 7267-7277.

(27) Mudryk, Y.; Grytsiv, A.; Rogl, P.; Dusek, C.; Galatanu, A.; Idl, E.; Michor, H.; Bauer, E.; Godart, C.; Kaczorowski, D.; Romaka, L.; Bodak, O., *J. Phys.-Condens. Matter* **2001,** *13*, 7391-7402.

(28) Fisk, Z.; Hess, D. W.; Pethick, C. J.; Pines, D.; Smith, J. L.; Thompson, J. D.; Willis, J. O., *Science* **1988,** *239*, 33-42.

(29) Hundley, M. F.; Sarrao, J. L.; Thompson, J. D.; Movshovich, R.; Jaime, M.; Petrovic, C.; Fisk, Z., *Phys. Rev. B: Condens. Matter* **2002,** *65*, 024401.

(30) Fisk, Z.; Lambert, S. E.; Maple, M. B.; Remeika, J. P.; Espinosa, G. P.; Cooper, A. S.; Barz, H.; Oseroff, S., *Solid State Commun.* **1982,** *41*, 63-67.

(31) Andres, K.; Remeika, J. P.; Espinosa, G. P.; Cooper, A. S., *Phys. Rev. B.* **1981,** *23*, 1179-1184.

(32) Espinosa, G. P., *Mat. Res. Bull.* **1980,** *15*, 791-798.

(33) Skolozdra, R. V.; Akselrud, L. G.; Koretskaya, O. E., *Kristallografiya* **1985,** *30*, 1003-1004.

(34) Skolozdra, R. V.; Koretskaya, O. E.; Aksel'rud, L. G., *Ukr. Fiz. Zh.* **1986,** *31*, 1537-1541.

(35) Sheldrick, G. M. *SHELXL-97, Program for Refinement of Crystal Structures*, University of Göttingen: Göttingen, Germany, **1997**.

(36) Kotur, B. Y.; Cerny, R., *Croatica Chemica Acta* **1999,** *72*, 341-350.

(37) Bochu, B.; Deschizeaux, M. N.; Joubert, J. C.; Collomb, A.; Chenavas, J.; Marezio, M., *J. Solid State Chem.* **1979,** *29*, 291-298.

(38) Donohue, J., *The Structures of the Elements*. Wiley: New York, 1974; p 216.

(39) Emsley, J., *The Elements*. Oxford University Press: New York, **1999**.

(40) Havinga, E. E.; Hokkelin.P; Damsma, H., *J. Less-Common Met.* **1972,** *27*, 169-186.

(41) Lang, A.; Jeitschko, W., *Z. MetaIlkd.* **1996,** *87*, 759-764.

CHAPTER 3. CRYSTAL GROWTH, TRANSPORT AND MAGNETIC PROPERTIES OF $YbCoGa_5$*

3.1 Introduction

Heavy fermion materials are intermetallic compounds whose *f*-electrons couple strongly with conductive electrons, resulting in the effective mass becoming ~ 100 times greater than that of a free electron.[1, 2] Heavy fermions possess large Sommerfeld or electronic specific heat coefficients (γ), which are about two orders of magnitude to that of ordinary metals (Cu $\gamma \sim 1$ mJ $mol^{-1} K^{-2}$) and are obtained from heat capacity measurements.[2] A characteristic of heavy fermion behavior is the instability of the *f* electronic configuration.[3] Ce ions can have an outer electronic configuration of $4f^1$ (Ce^{3+}) or $4f^0$ (Ce^{4+}). Because the ground states of $4f^1$ and $4f^0$ are close in energy, it is possible for fluctuations to occur between both oxidation states (Ce^{3+}/Ce^{4+}). Likewise, it is also possible for Yb to fluctuate between Yb^{3+}/Yb^{2+}. Due to the similarities between Ce ions and Yb ions, Yb can be viewed as the hole analogue of Ce. Recently we have focused our efforts to find Yb based compounds that display both heavy fermion behavior and superconductivity.[4] Nakatsuji et al. have reported superconductivity (T_c = 80 mK) and heavy fermion behavior ($\gamma \sim 150$ mJ $mol^{-1} K^{-2}$) in β-$YbAlB_4$, which is the first ytterbium-based heavy fermion superconductor.[4-6]

The discovery of superconductivity in the heavy fermion compound $CeRhIn_5$[7] led to the study of its structurally related compounds with the formula Ce_nMIn_{3n+2} (n = 1, 2, ∞; M = Co, Rh, Ir).[8-13] These compounds display heavy fermion behavior with the coexistence of superconductivity and magnetism.[8-13] The heavy fermion compound $CeRhIn_5$ ($\gamma \sim 400$ mJ $mol^{-1}K^{-2}$) superconducts below 2.1 K at a pressure of 1.6 GPa.[7] $CeCoIn_5$ ($\gamma \sim 290$ mJ $mol^{-1}K^{-2}$) and $CeIrIn_5$ ($\gamma \sim 750$ mJ $mol^{-1}K^{-2}$) superconduct at 2.3 K and 0.4 K, respectively under ambient pressure.[8, 9] The n = 2 members include Ce_2RhIn_8 ($\gamma \sim 400$ mJ $mol^{-1}K^{-2}$) which superconducts at

*Reprinted by permission of American Chemical Society: Okudzeto, E. K; Kuga, K.; Nakatsuji, S.; Chan, J. Y.; "Crystal Growth, Transport, and Magnetic Properties of $YbCoGa_5$", *Cryst. Growth Des*. **2009**, 9, 1956-1959.

2 K under an induced pressure of 2.3 GPa.[10] Ce_2CoIn_8 ($\gamma \sim 400$ mJ $mol^{-1}K^{-2}$) superconducts at 0.4 K while Ce_2IrIn_8 ($\gamma \sim 700$ mJ $mol^{-1}K^{-2}$) is paramagnetic.[11, 12]

The structure and magnetic properties of $YbCoIn_5$, $YbRhIn_5$ and $YbIrIn_5$ have previously been reported.[14-17] $YbCoIn_5$ displays Pauli paramagnetic behavior,[16] while $YbRhIn_5$ and $YbIrIn_5$ are diamagnetic with Yb in the +2 oxidation state.[17] Grin et al. reported the structure of *Ln*$CoGa_5$ with *Ln* = Y, Gd-Tm and Lu.[18] The magnetic properties of *Ln*$CoGa_5$ (*Ln* = Tb-Tm) has been reported by Hudis et al.[19] The compounds with *Ln* = Tb, Dy and Ho order antiferromagnetically at low temperatures, while the Er and Tm analogues show no sign of magnetic ordering down to 2 K.[19] Previous attempts to synthesize single crystals of $YbCoGa_5$ resulted in the synthesis of $YbCo_2Ga_8$.[19, 20] Our detailed investigation of the Yb-Co-Ga system has led us to succeed in the synthesis of high quality single crystals of $YbCoGa_5$ for the first time. We present herein the crystal growth, structure, magnetic, specific heat and transport properties of $YbCoGa_5$.

3.2 Experimental

3.2.1 Synthesis

Single crystals of $YbCoGa_5$ were grown in gallium flux using the constituent elements (Yb, 99.9 %, Co, 99.998 %, and Ga, 99.99999 %) all purchased from Alfa Aesar and used as received. The constituent elements were combined in a 2:1:10 (Yb:Co:Ga) molar ratio, covered with quartz wool and sealed into an evacuated fused-silica tube. The sample was then heated to 1323 K dwelled for 48 h, and slowly cooled to 550 K at a rate of 5 K/h. Excess gallium flux was separated from the crystals by centrifugation. When necessary, topical flux was removed by immersing the recovered crystals in hot water, as well as etching in dilute HCl. Crystals obtained from the above synthesis method were plate-like in nature, with maximum dimensions

of ~ 0.5 x 3 x 4 mm^3. Figure 3.1 shows a picture of a single crystal of $YbCoGa_5$. Multiple crystals were selected for characterization by single crystal X-ray diffraction.

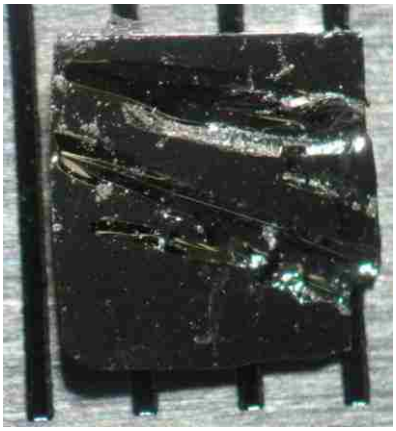

Figure 3.1 Photograph of a single crystal of $YbCoGa_5$ grown with Ga flux.

3.2.2 Single Crystal X-ray Diffraction and Elemental Analysis

Crystal fragments with dimensions of ~ 0.03 x 0.03 x 0.03 mm^3 were mechanically selected for the structural analysis of $YbCoGa_5$. The crystals were glued onto the tip of a glass fiber and mounted on a Nonius Kappa CCD diffractometer outfitted with Mo K_α radiation (λ = 0.71073Å). Data collection was taken at 298 K. Additional crystallographic parameters are included in Table 3.1. The crystal structure of $YbCoGa_5$ was solved with direct methods using SHELXS97 and refined using SHELXL97.[21] The model of the refined structure was compared to the parent compound $HoCoGa_5$.[18] After refinement the data were corrected for extinction effects and the displacement parameters were refined as anisotropic. A list of atomic positions, Wyckoff symmetry, and anisotropic displacement parameters are shown in Table 3.2. Electron micro-probe analysis was performed on single crystals of $YbCoGa_5$ to determine the relative amount of impurities in the compound. The elemental analysis was performed using a JEOL JSM-5060 scanning electron microscope equipped with an energy dispersive spectrometer. The

accelerating voltage was 15 kV with a beam to sample distance of 20 mm. The average elemental ratio obtained was Yb: Co: Ga = 1: 0.98: 5.10, with an error of ~ 3 %.

Table 3.1 Crystallographic Parameters for $YbCoGa_5$

Compound	$YbCoGa_5$
Space Group	*P*4/*mmm*
a (Å)	4.190(1)
c (Å)	6.727(3)
V (Å^3)	118.10(7)
Z	1
Dimensions (mm^3)	0.03 x 0.03 x 0.03
Temperature (K)	298(2)
ρ (g/cm^3)	8.163
θ Range	3.03 - 31.84
Collected reflections	364
Unique reflections	144
h	$-5 \leq h \leq 5$
k	$-4 \leq k \leq 4$
l	$-9 \leq l \leq 8$
$\Delta\rho_{max}$ (eÅ^{-3})	2.724
$\Delta\rho_{min}$ (eÅ^{-3})	-1.467
R_1 (*F*)[a]	0.0194
R_w[b]	0.0530

[a] $R_1 = \Sigma||F_o| - |F_c||/\Sigma|F_o|$

[b] $R_w = [\Sigma [w (F_o^2 - F_c^2)^2]/ \Sigma [w (F_o^2)^2]]^{1/2}$; $w = 1/[\sigma^2(F_o^2) + (0.0241P)^2 + 0.4441P]$

Table 3.2 Atomic Positions and Thermal Parameters for $YbCoGa_5$

Atom	Wyckoff site	*x*	*y*	*z*	U_{eq} (eÅ^2)[a]
Yb	1*a*	0	0	0	0.0009 (3)
Co	1*b*	0	0	½	0.0015 (4)
Ga1	1*c*	½	½	0	0.0052 (4)
Ga2	4*i*	0	½	0.30735(13)	0.0049 (3)

[a] U_{eq} is defined as one-third of the trace of the orthogonalized U_{ij} tensor

3.2.3 Physical Property Measurements

Magnetic susceptibility measurements were performed using a Quantum Design Magnetic Property Measuring System. Data were collected over a temperature range of 2–300 K. The susceptibility measurements were performed on different crystals of $YbCoGa_5$ for each direction. Electrical resistivity data was measured using the four probe method using a Quantum Design Physical Property Measuring System, with the current applied in the plane of the sample. Specific heat measurements were performed with a Quantum Design PPMS using a thermal relaxation method from 50 K down to 0.35 K. Resistivity measurements performed on single crystals of $YbCoGa_5$ show no superconducting transition associated with Ga. This confirms the absence of excess Ga flux.

3.3 Results and Discussion

3.3.1 Structure

$YbCoGa_5$ crystallizes in the tetragonal $HoCoGa_5$ structure type in the space group *P*4/*mmm*.[18] The crystal structure of $YbCoGa_5$ is shown in Figure 3.2, and consists of $YbGa_{12}$ cuboctahedra and $CoGa_2$ rectangular prisms. $YbCoGa_5$ can be viewed as a variant of the $AuCu_3$ and $PtHg_2$ structure types with the $YbGa_{12}$ cuboctahedra separated by the $CoGa_2$ rectangular prisms.

Figure 3.3 shows a plot of the cell volume of *Ln*$CoGa_5$ (*Ln* = Gd-Yb).[18] The cell volumes decrease from Gd to Lu as expected due to the lanthanide contraction. The volume of $YbCoGa_5$ shows a positive deviation in the plot, indicating that ytterbium is intermediate-valent or divalent. A similar phenomenon is seen in the *Ln*$RhIn_5$ and *Ln*$CoIn_5$ series with *Ln* = La-Lu where a positive deviation is seen in the cell volume of Yb.[22] Figure 3.4 shows a plot of lattice parameters of *Ln*$CoGa_5$ (*Ln* = Sm-Yb).[18, 23] The *c* lattice parameter of $YbCoGa_5$ is in between

that of Er and Ho. In contrast, the *a* and *c* lattice parameters of $YbRhIn_5$ are between those of $SmRhIn_5$ and $GdRhIn_5$, indicating a divalent state for

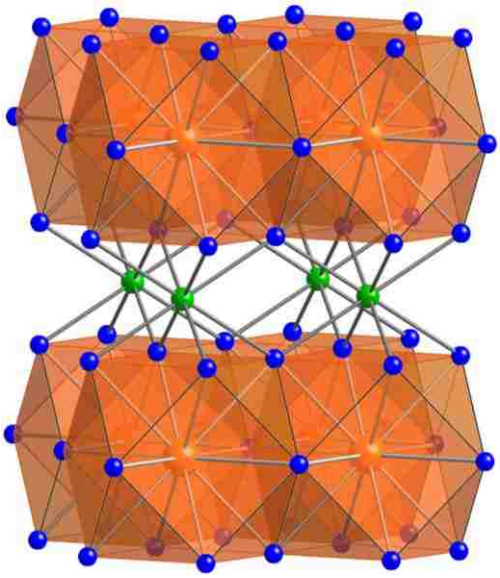

Figure 3.2 The crystal structure of $YbCoGa_5$ is shown along the *c*-axis. Yb, Co and Ga atoms are represented as orange, green and blue spheres, respectively.

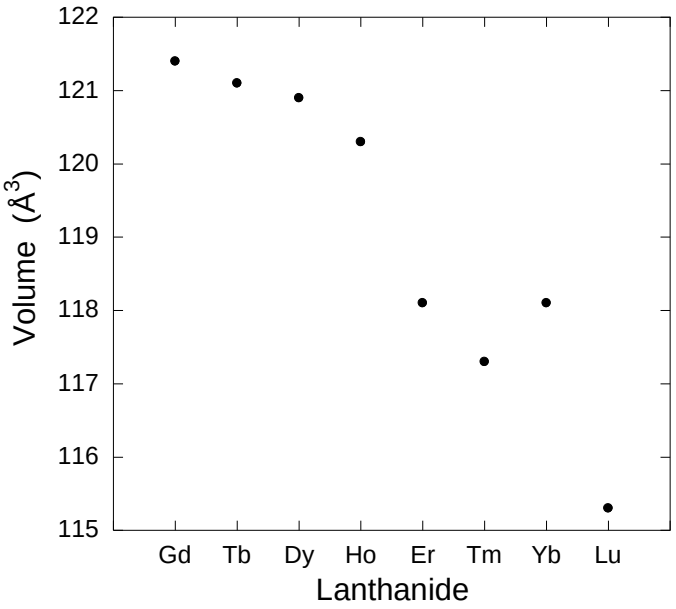

Figure 3.3 Cell volume of *Ln*$CoGa_5$ (*Ln* = Gd-Lu) as a function of lanthanide. Data for the Gd, Tb, Dy, Ho, Er, Tm and Lu analogues were obtained from Ref (12).

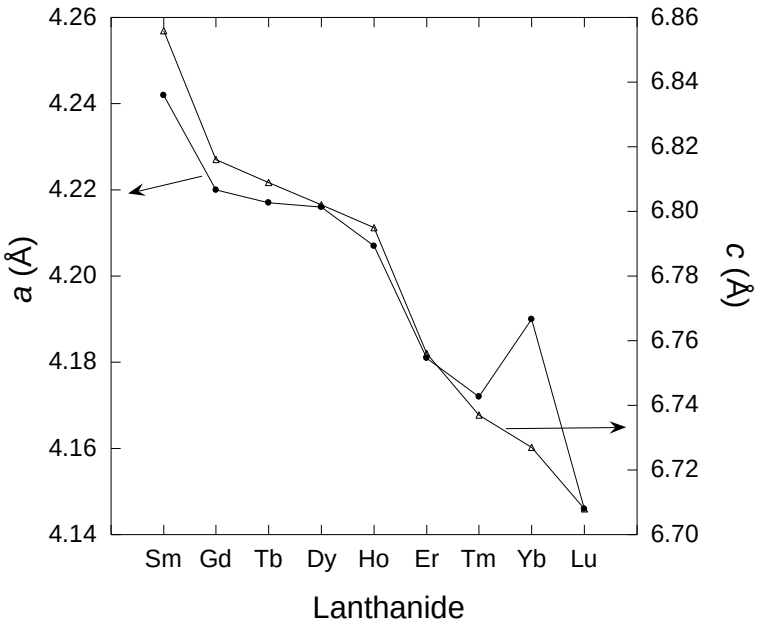

Figure 3.4 Lattice parameters of *Ln*CoGa$_5$ (*Ln* = Sm-Lu) as a function of lanthanide. Data for the Sm, Gd, Tb, Dy, Ho, Er, Tm and Lu analogues were obtained from Ref (12) and (20). Lines are drawn to guide the eye.

3.3.2 Physical Properties

Figure 3.5 shows the temperature dependent magnetic susceptibility of YbCoGa$_5$ at 0.1 T and 1 T from 2-300 K. The susceptibility measurements were obtained with an applied field parallel to the *c*-axis and the *ab*-plane. The results from both directions indicate temperature independent paramagnetic behavior, which is indicative of a Pauli paramagnet and similar to the isostructural compound YbCoIn$_5$.[16] However, negative susceptibility corresponding to diamagnetism, is observed on single crystals of YbRhIn$_5$ and YbIrIn$_5$.[17] At low temperatures a strong upturn is seen in χ (T) of YbRhIn$_5$ and YbIrIn$_5$ which is believed to be due to paramagnetic impurities.[17] The absence of a low temperature upturn in the susceptibility of YbCoGa$_5$ indicates that our crystals are free of such impurities.

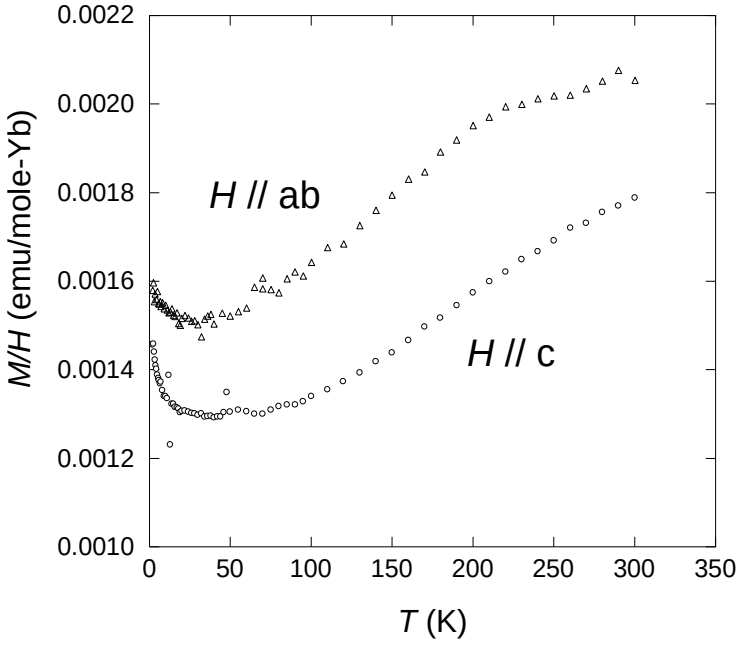

Figure 3.5 Temperature-dependence of the magnetic susceptibility (χ) of $YbCoGa_5$ at H = 0.1 T, where open triangles and circles represent crystal orientation parallel to the *ab* plane and *c*-axis, respectively.

Figure 3.6 shows the temperature dependence of the specific heat divided by temperature (C/T) for $YbCoGa_5$. At temperatures much lower than the Debye temperature, the specific heat of a normal metal can be fit to $C = \gamma T + \alpha T^3$, namely, the sum of the heat capacity contributions from the electrons and phonons, respectively. The equation fits well with the experimental data below 6 K, as shown in the inset of Figure 3.6, and gives γ ~ 11.2 mJ/mol K^2 and Θ_D = 220 K. We observe much smaller values of γ and χ at low temperatures in $YbCoGa_5$ than in $YbAlB_4$,[4, 5] suggesting that ytterbium is indeed divalent. The γ value and Debye temperature in $YbCoGa_5$ are similar to those observed in the f^{14} containing compound $LuCoGa_5$ (γ ~ 6 mJ/mol K^2 and Θ_D = 180 K).[24] The similarity in values confirms that Yb in $YbCoGa_5$ is likely to be in a f^{14} state and divalent.

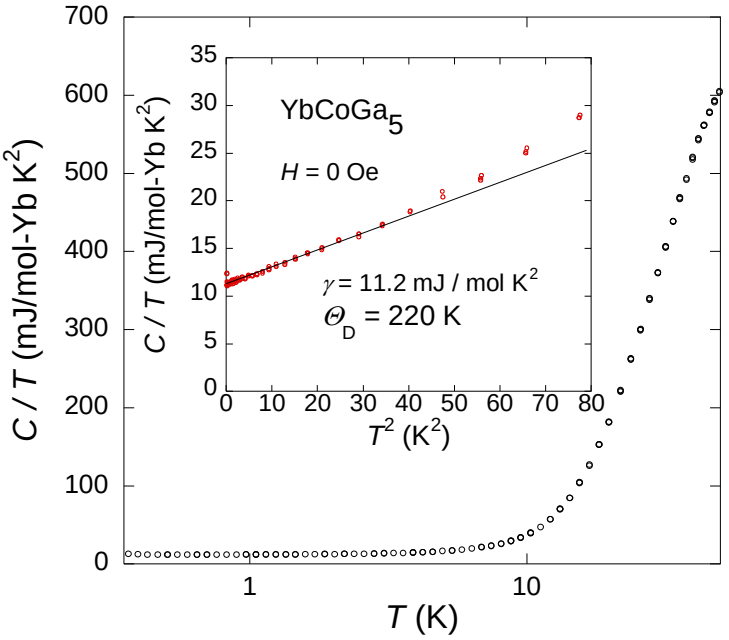

Figure 3.6 Zero-field specific heat of $YbCoGa_5$ as a function of temperature. The inset shows C_m/T vs.T^2 of $YbCoGa_5$.

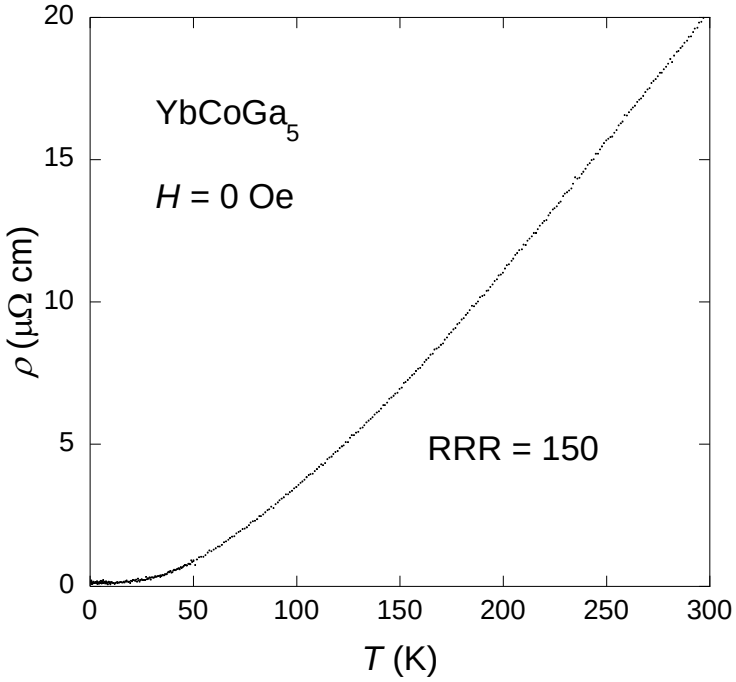

Figure 3.7 Temperature-dependent electrical resistivity of $YbCoGa_5$.

Figure 3.7 shows the temperature dependence of electrical resistivity for $YbCoGa_5$. $YbCoGa_5$ displays normal metallic behavior, unlike the Kondo behavior observed in $YbAlB_4$.[5] The electrical resistivity of $YbCoGa_5$ shows a T^5 relationship, indicating lattice contributions at temperatures lower than the Debye temperature. This means that the electron correlation effect is hardly seen in the temperature dependence of the resistivity and suggests again that ytterbium is indeed divalent. The residual resistivity ratio, RRR = $\rho_{300\ K}/\rho_0$ for $YbCoGa_5$ is 150, indicating high crystal quality. The residual resistivity values reported for *Ln*$CoGa_5$ (*Ln* = Tb-Tm) are ~ 10 for all analogues, indicating defects and disorder in the crystals.[19]

3.4 Summary

We have synthesized single crystals of $YbCoGa_5$ for the first time. The crystals have been characterized by single crystal X-ray diffraction. Magnetic and specific heat measurements indicate Yb in $YbCoGa_5$ is in a divalent state. The residual resistivity ratio obtained from resistivity measurements indicates high crystal quality of $YbCoGa_5$ crystals.

3.5 References

(1) Fisk, Z.; Ott, H. R.; Rice, T. M.; Smith, J. L., *Nature* **1986,** *320*, 124-129.

(2) Fisk, Z.; Hess, D. W.; Pethick, C. J.; Pines, D.; Smith, J. L.; Thompson, J. D.; Willis, J. O., *Science* **1988,** *239*, 33-42.

(3) Fisk, Z.; Sarrao, J. L.; Smith, J. L.; Thompson, J. D., *Proc. Natl. Acad. Sci* **1995,** *92*, 6663-6667.

(4) Macaluso, R. T.; Nakatsuji, S.; Kuga, K.; Thomas, E. L.; Machida, Y.; Maeno, Y.; Fisk, Z.; Chan, J. Y., *Chem. Mat.* **2007,** *19*, 1918-1922.

(5) Nakatsuji, S.; Kuga, K.; Machida, Y.; Tayama, T.; Sakakibara, T.; Karaki, Y.; Ishimoto, H.; Yonezawa, S.; Maeno, Y.; Pearson, E.; Lonzarich, G. G.; Balicas, L.; Lee, H.; Fisk, Z., *Nature Phys.* **2008,** *4*, 603-607.

(6) Kuga, K.; Karaki, Y.; Matsumoto, Y.; Machida, Y.; Nakatsuji, S., *Phys. Rev. Lett.* **2008,** *101*, 137004-4.

(7) Hegger, H.; Petrovic, C.; Moshopoulou, E. G.; Hundley, M. F.; Sarrao, J. L.; Fisk, Z.; Thompson, J. D., *Phys. Rev. Lett.* **2000,** *84*, 4986-4989.

(8) Petrovic, C.; Pagliuso, P. G.; Hundley, M. F.; Movshovich, R.; Sarrao, J. L.; Thompson, J. D.; Fisk, Z.; Monthoux, P., *J. Phys.-Condes. Matter* **2001,** *13*, L337-L342.

(9) Petrovic, C.; Movshovich, R.; Jaime, M.; Pagliuso, P. G.; Hundley, M. F.; Sarrao, J. L.; Fisk, Z.; Thompson, J. D., *Europhys. Lett.* **2001,** *53*, 354-359.

(10) Nicklas, M.; Sidorov, V. A.; Borges, H. A.; Pagliuso, P. G.; Petrovic, C.; Fisk, Z.; Sarrao, J. L.; Thompson, J. D., *Phys. Rev. B* **2003,** *67*, 020506.

(11) Chen, G. F.; Ohara, S.; Hedo, M.; Uwatoko, Y.; Saito, K.; Sorai, M.; Sakamoto, I., *J. Phys. Soc. Jpn.* **2002,** *71*, 2836-2838.

(12) Thompson, J. D.; Movshovich, R.; Fisk, Z.; Bouquet, F.; Curro, N. J.; Fisher, R. A.; Hammel, P. C.; Hegger, H.; Hundley, M. F.; Jaime, M.; Pagliuso, P. G.; Petrovic, C.; Phillips, N. E.; Sarrao, J. L., *J. Magn. Magn. Mater.* **2001,** *226*, 5-10.

(13) Mathur, N. D.; Grosche, F. M.; Julian, S. R.; Walker, I. R.; Freye, D. M.; Haselwimmer, R. K. W.; Lonzarich, G. G., *Nature* **1998,** *394*, 39.

(14) Hieu, N. V.; Shishido, H.; Nakashima, H.; Sugiyama, K.; Settai, R.; Takeuchi, T.; Matsuda, T. D.; Haga, Y.; Hagiwara, M.; Kindo, K.; Onuki, Y., *J. Magn. Magn. Mater.* **2007,** *310*, 1721-1723.

(15) Zaremba, V. I.; Rodewald, U. C.; Hoffmann, R.-D.; Kalychak, Y. M.; Pöttgen, R., *Z. Anorg. Allg. Chem.* **2003,** *629*, 1157-1161.

(16) Isikawa, Y.; Kato, D.; Mitsuda, A.; Mizushima, T.; Kuwai, T., *J. Magn. Magn. Mater.* **2004,** *272-276*, 635-636.

(17) Bukowski, Z.; Gofryk, K.; Kaczorowski, D., *Solid State Commun.* **2005,** *134*, 475-478.

(18) Grin, Y. N.; Yarmolyuk, Y. P.; Gradyshevsky, E. I., *Kristallografiya* **1979,** *24*, 242-246.

(19) Hudis, J.; Hu, R.; Broholm, C. L.; Mitrovic, V. F.; Petrovic, C., *J. Magn. Magn. Mater.* **2006,** *307*, 301-307.

(20) Fritsch, V.; Bobev, S.; Moreno, N. O.; Fisk, Z.; Thompson, J. D.; Sarrao, J. L., *Phys. Rev. B* **2004,** *70*, 052410.

(21) Sheldrick, G. M. *SHELXL-97, Program for Refinement of Crystal Structures*, University of Göttingen: Göttingen, Germany, **1997**.

(22) Zaremba, V. I.; Rodewald, U. C.; Pöttgen, R., *Z. Anorg. Allg. Chem.* **2005,** *631*, 1065-1070.

(23) Jia, Y.; Belin, C.; Tillard, M.; Lacroix-Orio, L.; Zitoun, D.; Feng, G., *Inorg. Chem.* **2007,** *46*, 4177-4186.

(24) Matsuda, T. D.; Haga, Y.; Sakai, H.; Aoki, D.; Ikeda, S.; Yamamoto, E.; Shishido, H.; Settai, R.; Harima, H.; Onuki, Y., *J. Phys. Soc. Jpn.* **2008,** *77*, 024704/1-024704/6.

CHAPTER 4. CRYSTAL GROWTH, TRANSPORT, MAGNETIC AND MÖSSBAUER PROPERTIES OF Ln_4FeGa_{12} WITH *Ln* = Y, Tb, Dy, Ho, AND Er

4.1 Introduction

Several compounds in the *Ln*-*M*-Ga family, where *Ln* is a lanthanide and *M* is a transition metal, display strongly correlated electron behavior, such as magnetic ordering, superconductivity, heavy fermion behavior, and large magnetoresistance.[1] For example, several recently studied[2,3] compounds in the *Ln*-*M*-Ga family, where *M* is Ni, Pd, and Pt, exhibit large positive magnetoresistance of up to ca. 200 % for La_2NiGa_{12} and Ce_2PdGa_{10}. Previously, we have grown single crystals of Ln_4MGa_{12}, where *Ln* is Tb, Dy, Ho, and Er; and *M* is Pd and Pt.[5,6] The Pt-analogues with Dy, Er, and Ho display a large positive magnetoresistance of 50, 220, and 900 %, respectively.[6]

In order to study the role of magnetic transition metals in lanthanide-gallium compounds we have explored several phases in the *Ln*-Fe-Ga system. This study has been motivated by the wide variety of thermal, electric, and magnetic properties of the iron containing AFe_4Sb_{12} skutterudites, where *A*, the so-called filling or rattling atom or ion, is an electropositive metal or ion. Depending on the nature of the electropositive metal, i.e., the filling atom, in the filled skutterudites, the iron sublattice may or may not exhibit a magnetic moment. Whereas in most rare-earth and thallium filled skutterudites[9,10] the iron atoms do not carry any magnetic moment, in the filled $NaFe_4Sb_{12}$ and KFe_4Sb_{12} skutterudites the iron sublattice displays ferromagnetic ordering with an effective magnetic moment of 1.6 μ_B per iron.[7,8] In contrast, $LaFe_4Sb_{12}$ exhibits paramagnetic behavior,[9] and the mixed valent Yb-filled $YbFe_4Sb_{12}$ skutterudite exhibits no magnetic moment on the iron sublattice, as is indicated by the magnetic and Mössbauer spectral measurements.[10] With the goal of studying the effect of transition metals on the magnetization of the Ln_4MGa_{12} compounds, we have synthesized Ln_4FeGa_{12}, where *Ln* is Y, Tb, Dy, Ho, and

Er. Herein, we report the crystal growth, magnetic and transport measurements, structural properties, and Mössbauer spectral studies of these new Ln_4FeGa_{12} compounds.

4.2 Experimental

4.2.1 Synthesis

Single crystals of Ln_4FeGa_{12}, where *Ln* is Y, Tb, Dy, Ho, and Er, were synthesized from their constituent elements by using *Ln* metals of at least 99.9 % purity, Fe of 99.998 % purity, and Ga of 99.99999 % purity. All the starting materials were obtained from Alfa Aesar and used as received. The elements were combined in a 1:1:20 molar ratio in an alumina crucible, covered with quartz wool, and sealed in an evacuated fused-silica tube. Each sample was then heated to 1423 K for 24 h and slowly cooled to 773 K at a rate of 15 K/h. Excess Ga flux was removed from the synthesized crystals by centrifugation, and when necessary, topical flux was removed by etching the recovered crystals in concentrated HCl. The $LnGa_6$ and Fe_3Ga_4 binary compounds were the dominant phases formed in the above synthesis and the minor phase consisted of cubic crystals of Ln_4FeGa_{12}, crystals with a maximum dimension of 0.5 mm.

In order to determine whether the unexpected magnetic properties of Y_4FeGa_{12} were intrinsic or extrinsic, we varied the reaction profiles and conditions to optimize its synthesis; reaction profiles with reaction ratios of 2:1:20, 1:5:20, 1:1:10, and with various dwell times were used. All these reaction profiles resulted in YGa_6 and Fe_3Ga_4 as the dominant phases.

Arc melting of the constituent Y, Fe, and Ga elements in a 4:1:12 ratio resulted in a mixture of Y_4FeGa_{12} and YGa_6. In contrast, heating these elements in a 4:1:12 molar ratio in an induction furnace and subsequently annealing with a "seed crystal" of Y_4FeGa_{12} and excess Ga at 1423 K for 48 h, followed by slow cooling to 773 K at a rate of 5 K/h, resulted in an ca. 80 % yield of the cubic Y_4FeGa_{12} phase. The seed crystal method was also used to synthesize single crystals of Tb_4FeGa_{12}, Dy_4FeGa_{12}, Ho_4FeGa_{12}, and Er_4FeGa_{12}, with yields of 90, 80, 70, and 60

%, respectively. The cubic crystals obtained from the seed growth had a maximum volume of 9 mm^3; a picture of crystals of Dy_4FeGa_{12} grown in a gallium flux is shown in Figure 4.1. We were able to grow polycrystalline samples of Tm_4FeGa_{12} by using an induction furnace. However single crystals were not of sufficient quality or suitable for structural analysis or property measurements. Furthermore the yield is not adequate for measurements. Attempts to grow single crystals of Yb_4FeGa_{12} resulted in the synthesis of the binary $YbGa_4$.

Multiple single crystals of Ln_4FeGa_{12} were selected for characterization by single crystal x-ray diffraction and magnetization measurements. Further, several single crystals of Ln_4FeGa_{12} were ground and used for the Mössbauer spectral study. The homogeneity of the compounds was checked by powder x-ray diffraction.

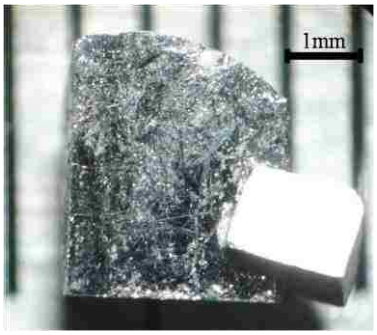

Figure 4.1 Photograph of crystals of Dy_4FeGa_{12} grown with Ga flux.

4.2.2 Single Crystal X-ray Diffraction

Crystal fragments with dimensions of ca. 0.05 × 0.05 × 0.05 mm^3 were manually selected with an optical microscope for structural analysis. The crystals were glued onto a glass fiber and mounted on a Nonius Kappa CCD diffractometer that used 0.71073 Å Mo $K\alpha$ radiation. Structural and refinement parameters are given in Table 4.1. The structure of Ln_4FeGa_{12} where *Ln* is Y, Tb, Dy, Ho, and Er, was solved by direct methods using SHELXS97 and refined using SHELXL97;[11] the model of the refined structures were compared with that of the parent

compound Y_4PdGa_{12}.[12] After refinement, the data were corrected for extinction effects and the displacement parameters were refined anisotropically. Table 4.2 gives the atomic positions and thermal displacement parameters for the above compounds. Additional information in CIF format is provided as supporting information.

Table 4.1 Crystallographic Parameters for Ln_4FeGa_{12} (*Ln* = Y, Tb, Dy, Ho, Er)

Compound	Y_4FeGa_{12}	Tb_4FeGa_{12}	Dy_4FeGa_{12}	Ho_4FeGa_{12}	Er_4FeGa_{12}
Space Group	$Im\bar{3}m$	$Im\bar{3}m$	$Im\bar{3}m$	$Im\bar{3}m$	$Im\bar{3}m$
a (Å)	8.5650(4)	8.5610(4)	8.5350(3)	8.5080(3)	8.4720(4)
V (Å^3)	628.32(5)	627.44(5)	621.74(4)	615.86(4)	608.08(5)
Z	2	2	2	2	2
Crystal Dimensions (mm^3)	0.05x0.05x0.5	0.05x0.05x0.05	0.05x0.05x0.05	0.05x0.05x0.05	0.05x0.05x0.05
Temperature (K)	298(2)	298(2)	298(2)	298(2)	298(2)
ρ (g/cm3)	6.597	8.089	8.239	8.370	8.528
θ Range	3.36-29.86	3.37-29.88	3.38-29.98	3.39-29.85	4.81-30.45
μ (mm-1)	44.528	48.543	50.275	52.184	54.431
Collected reflections	294	304	295	278	164
Unique reflections	103	108	105	107	101
h	-11≤ *h* ≤ 12	-11≤ *h* ≤ 12	-11≤ *h* ≤ 12	-11≤ *h* ≤ 11	-12≤ *h* ≤ 12
k	-8≤k ≤ 8	-8≤k ≤ 8	-8≤ *k* ≤ 8	-8≤k ≤ 8	-8≤k ≤ 8
l	-7≤ *l* ≤ 7	-7≤ *l* ≤ 7	-7≤ *l* ≤ 7	-7≤ *l* ≤ 7	-8≤ *l* ≤ 7
$\Delta\rho_{max}$ (eÅ^{-3})	2.605	2.641	2.906	1.513	1.108
$\Delta\rho_{min}$ (eÅ^{-3})	-1.631	-3.330	-2.307	-3.902	-2.464
R_1 (*F*)[a]	0.0382	0.0383	0.0305	0.0256	0.0200
R_w[b]	0.0655	0.0936	0.0871	0.0730	0.0588

[a] $R_1 = \Sigma||F_o| - |F_c||/\Sigma|F_o|$

[b] $R_w = [\Sigma [w (F_o^2 - F_c^2)^2]/ \Sigma [w (F_o^2)^2]]^{1/2}$; w = 1/[$\sigma^2(F_o^2)$ + (0.00000P)^2 + 4.7941P] , w = 1/[$\sigma^2(F_o^2)$ + (0.0390P)^2 + 7.8321*P*] , w = 1/[$\sigma^2(F_o^2)$ + (0.0311P)^2 + 17.4653P] , w = 1/[$\sigma^2(F_o^2)$ + (0.0138P)^2 + 20.5004P] , w = 1/[$\sigma^2(F_o^2)$ + (0.0226P)^2^+37.3517P] for Y, Tb, Dy, Ho and Er respectively

Table 4.2 Atomic Positions and Thermal Parameters for Ln_4FeGa_{12} (*Ln* = Y, Tb-Er)

Atom	Wyckoff site	*x*	*y*	*z*	U_{eq} (Å^2) [a]
			Y_4FeGa_{12}		
Y1	8*c*	¼	¼	¼	0.0070(4)
Fe1	2*a*	0	0	0	0.0128(10)
Ga1	12*d*	¼	0	½	0.0128(7)
Ga2	12*e*	0.2848(3)	0	0	0.0154(9)
			Tb_4FeGa_{12}		
Tb1	8*c*	¼	¼	¼	0.0074(6)
Fe1	2*a*	0	0	0	0.0124(12)
Ga1	12*d*	¼	0	½	0.0127(10)
Ga2	12*e*	0.2845(6)	0	0	0.0158(13)
			Dy_4FeGa_{12}		
Dy1	8*c*	¼	¼	¼	0.0051(5)
Fe1	2*a*	0	0	0	0.0148(15)
Ga1	12*d*	¼	0	½	0.0109(10)
Ga2	12*e*	0.2828(4)0		0	0.0184(13)

Table 5.2 cont

		Ho_4FeGa_{12}			
Ho1	8*c*	¼	¼	¼	0.0082(5)
Fe1	2*a*	0	0	0	0.0208(14)
Ga1	12*d*	¼	0	½	0.0128(9)
Ga2	12*e*	0.2814(4)0	0	0.0237(12)	
		Er_4FeGa_{12}			
Er1	8*c*	¼	¼	¼	0.0079(5)
Fe1	2*a*	0	0	0	0.042(4)
Ga1	12*d*	¼	0	½	0.031(3)
Ga2	12*e*	0.2617(17)	0	0	0.050(3)

[a] U_{eq} is defined as one-third of the trace of the orthogonalized U_{ij} tensor

4.2.3 Physical Property Measurements

Magnetic measurements on single crystals of Ln_4FeGa_{12} were performed by using the extraction magnetometer in a Quantum Design Physical Property Measurement System. The samples were held in place with Kapton tape. The magnetic properties have been measured after zero field cooling to 2 K and subsequent warming to 310 K in an applied field of 0.1 T followed by field cooling from 310 to 2 K over a period of approximately 12 hours. No significant difference was noted in the zero field cooled warming results and the field cooled results and the two data sets have been merged to obtain the results presented herein.

The four-probe method was used to measure the electrical resistivity of single crystals of Ln_4FeGa_{12} with a Quantum Design Physical Property Measurement System at ambient pressure. Two-mil diameter platinum leads were attached to the surface of the single crystals using silver epoxy and resistivity measurements were obtained from 2 to 290 K.

The Mössbauer spectra were measured between 4.2 and 295 K in a Janis Supervaritemp cryostat with a constant-acceleration spectrometer which utilized a rhodium matrix cobalt-57 source and was calibrated at 295 K with α-iron powder. The Mössbauer spectral absorbers contained 26 mg/cm^2 of Y_4FeGa_{12} or 20 mg/cm^2 of Tb_4FeGa_{12}, Dy_4FeGa_{12}, or Er_4FeGa_{12} powder mixed with boron nitride. The quoted errors for the Mössbauer spectral parameters are the relative statistical errors; the absolute errors are approximately twice as large.

4.3 Results

4.3.1 Crystal Structures

The Ln_4FeGa_{12} compounds, where *Ln* is Y, Tb, Dy, Ho, and Er, crystallize in the cubic Y_4PdGa_{12} structure, with the $Im\bar{3}m$, number 229, space group.[12] The crystal structure of Tb_4FeGa_{12}, as is shown in Figure 4.2, consists of face sharing $TbGa_3$ cuboctahedra with corner sharing $FeGa_6$ octahedra. Selected bond distances in the Ln_4FeGa_{12} compounds are given in Table 4.3. The Fe–Ga2 interatomic distances are ca. 2.4 Å for all compounds, a distance that is only slightly smaller than the sum of the respective iron and gallium atomic radii of 1.24 and 1.22 Å, respectively.[14] The *Ln*–Ga_6 cuboctahedra in Ln_4FeGa_{12} have six *Ln*–Ga1 and six *Ln*–Ga2 interatomic distances of ca. 3.0 Å, see Table 4.3. These values are only slightly shorter than the sum of the atomic radii of the respective rare earth and gallium.

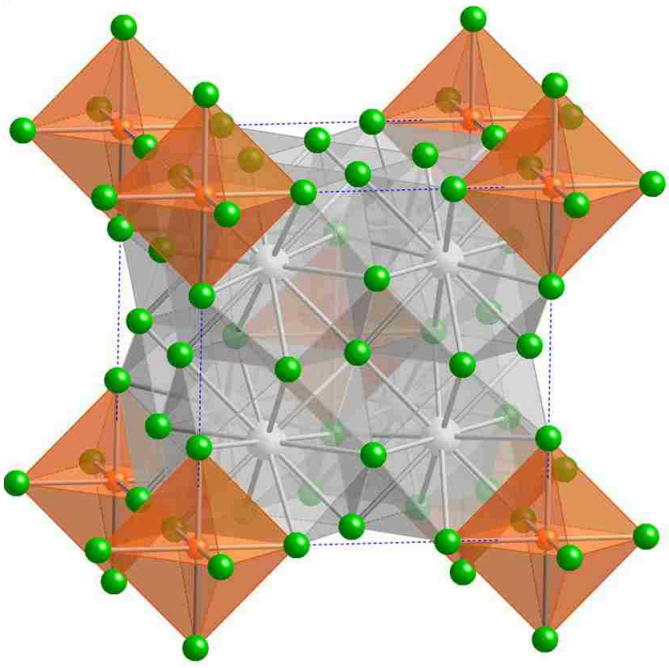

Figure 4.2 The crystal structure of Ln_4FeGa_{12}, where *Ln* may be Y, Tb, Dy, Ho, or Er. The *Ln*, Fe, and Ga atoms are shown in grey, orange, and green, respectively.

Table 4.3 Selected Interatomic Distances (Å) for Ln_4FeGa_{12} (*Ln* = Y, Tb, Dy, Ho, Er)

Metal bond	Y_4FeGa_{12}	Tb_4FeGa_{12}	Dy_4FeGa_{12}	Ho_4FeGa_{12}	Er_4FeGa_{12}
Ln cuboctahedra					
*Ln*1–Ga1	3.02818(14)	3.02677(14)	3.01758(11)	3.00803(11)	2.99530(14)
*Ln*1–Ga2	3.0428(3)	3.0416(4)	3.0305(4)	3.0199(4)	2.9969(5)
Ga1–Ga2	2.8255(15)	2.823(2)	2.827(2)	2.825(2)	2.927(13)
Fe octahedra					
Fe–Ga2	2.439(2)	2.440(4)	2.413(4)	2.394 (4)	2.216(18)

4.3.2 Magnetic Properties

The magnetic properties of the Ln_4FeGa_{12} compounds have been measured after zero field cooling to 2 K and subsequent warming to 310 K in an applied field of 0.1 T followed by field cooling. No significant difference was observed in the zero field cooled and the field cooled results indicating the absence of any magnetic spin-glass freezing above 2 K; the zero field cooled and the field cooled results have been merged to obtain the results presented below.

The magnetic susceptibilities, M/H, of the Ln_4FeGa_{12} compounds have been corrected for the diamagnetic contribution to the susceptibility by using Pascal's constants, see Table 4.4. For all the compounds the inverse molar magnetic susceptibility has been fit with the Curie-Weiss law over the temperature range given in Table 4.4. More specifically, for these fits, $1/\chi = aT + b$, where a is $1/C$, C is the Curie constant, and θ, the Weiss temperature, is $-b/a$. The resulting C and θ values and the corresponding effective magnetic moments, μ_{eff}, obtained from C are given in Table 4.4.

To a first approximation, the expected μ_{eff} for the four rare-earth containing compounds can be considered to arise from the sum of the moments of four *Ln*(III) ions and one Fe(III) ion and, in this case, $\mu_{eff} = \sqrt{4\mu_{Ln}^2 + \mu_{Fe}^2}$. In this approximation only the lowest energy, largest value, rare-earth J state is assumed to be populated. If the Fe(III) is assumed to be high-spin, its spin-only

effective magnetic moment is 5.916 μ_B. The expected μ_{eff} values obtained with these assumptions for four *Ln*(III) and one Fe(III) ions are given in Table 4.5, where the differences between the expected and observed values are also given. With the exception of Dy, all the observed μ_{eff} values are smaller than the expected calculated values. Because the assumption that the iron is high-spin iron(III) may be invalid in these intermetallic compounds, the iron μ_{eff} of 3.834 μ_B, obtained for Y_4FeGa_{12}, has been used to recalculate the expected μ_{eff}, see the seventh column in Table 4.5; the difference between the expected and observed values are given in the last column of Table 4.5. Even when using this smaller iron magnetic moment, all the differences are negative except for Dy_4FeGa_{12} and Ho_4FeGa_{12}; in the latter case the difference is very small. As the temperature increases, the somewhat higher energy, but smaller value, *J* states will be populated and μ_{eff} would be expected to decrease. The small thermal population of these higher energy, smaller value, *J* states will also introduce a small non-linearity to the inverse susceptibility, a non-linearity that is to some extent observed. Fits of the inverse molar magnetic susceptibility for all four of the rare-earth containing compounds at temperatures above 250 K yield slightly lower Curie constants and hence μ_{eff} values.

Table 4.4. Curie-Weiss Law Derived Magnetic Properties

Compound	χ_M^{dia}, emu/mol	Temperature range, K	θ, K	C, emuK/mol	$\mu_{eff,}^{a}$ μ_B
Y_4FeGa_{12}	–0.000154	150–320	–276.0	1.84	3.83
Tb_4FeGa_{12}	–0.000182	100–320	–52.1	47.84	19.56
Dy_4FeGa_{12}	–0.000182	75–320	–29.0(1)	65.26(2)	22.85(1)
Ho_4FeGa_{12}	–0.000182	15–300	–20.8	59.07	21.74
Er_4FeGa_{12}	–0.000178	40–320	–11.1	46.83	19.35

[a]The effective magnetic moment obtained from the Curie constant, *C*, and uncorrected for the θ value.

Table 4.5. Expected and Observed Magnetic Properties Based on Curie-Law Behavior

Ln(III)	Ground state	μ_{eff}, μ_B observed	μ_{eff}, μ_B, calc per *Ln*(III)	μ_{eff}, μ_B, calc per *Ln*(III)$_4$Fe(III)	Difference, μ_B	μ_{eff}, μ_B, calc per *Ln*(III)$_4$Fe(Y)	Difference, μ_B
Y	$^1S_0$	3.83	0	5.92	–2.09	3.83	0
Tb	$^7F_6$	19.56	9.72	20.32	–0.76	19.82	–0.26
Dy	$^6H_{15/2}$	22.85	10.64	22.10	+0.75	21.63	+1.22
Ho	$^5I_8$	21.74	10.61	22.02	–0.28	21.56	+0.18
Er	$^4I_{15/2}$	19.35	9.58	20.05	–0.70	19.54	–0.19

The temperature dependence of the molar magnetic susceptibility of Y_4FeGa_{12}, measured in an applied dc field of 0.1 T, is shown in Figure 4.3 and the analogous $\chi_M T$ plot is shown in the inset to this figure. At first one might think that the single iron in Y_4FeGa_{12} is undergoing long-range magnetic order below ca. 36 K. But this is not the case as is indicated by the rapid decrease in $\chi_M T$ below 18 K, by the small magnitude of the molar magnetic susceptibility below 36 K, by the large minimum Fe–Fe separation of 7.4175(4) Å along the body-diagonal of the unit cell, and by the Mössbauer spectra, to be discussed below. Rather it seems that below ca. 36 K the independent iron moments are simply polarized, i.e., aligned by the applied dc field of 0.1 T.

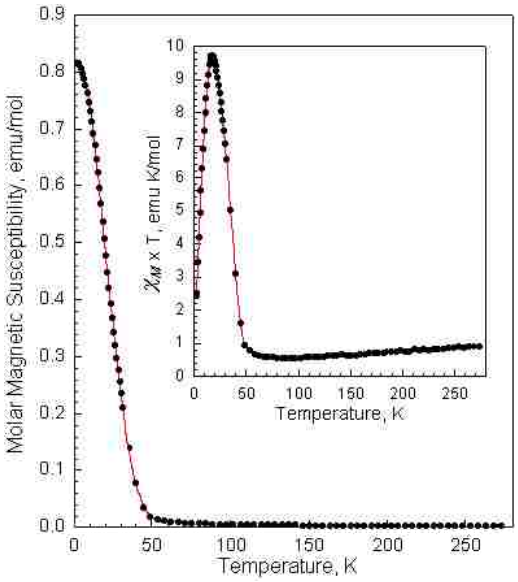

Figure 4.3 The temperature dependence of the molar magnetic susceptibility of Y_4FeGa_{12} measured in a 0.1 T applied dc field. Inset: The temperature dependence of $\chi_M \times T$.

A semi-logarithmic plot of the temperature dependence of the molar magnetic susceptibility of the rare-earth containing Ln_4FeGa_{12} compounds is shown in Figure 4.4a. All of these rare-earth containing compounds display an antiferromagnetic-like behavior with a maximum in the susceptibility at 25, 18.5, 9, and 6 K for the Tb, Dy, Ho, and Er compounds, respectively. This antiferromagnetic-like behavior results from the antiferromagnetic ordering of the *Ln* magnetic moments. However, unlike the molar magnetic susceptibility of a typical antiferromagnetic compound and, with the exception of Er_4FeGa_{12}, the molar susceptibility does not monotonically decrease at temperatures below the maximum, but rather remains constant at some value at or below that of its maximum. This constant susceptibility at lower temperatures could be the result of spin-canting, but this seems unlikely in an applied field of only 0.1 T. Thus we believe the susceptibility becomes approximately constant below the maximum because of the presence of the iron moment which may well be frustrated in the presence of the surrounding antiferromagnetically ordered rare-earth sublattices.

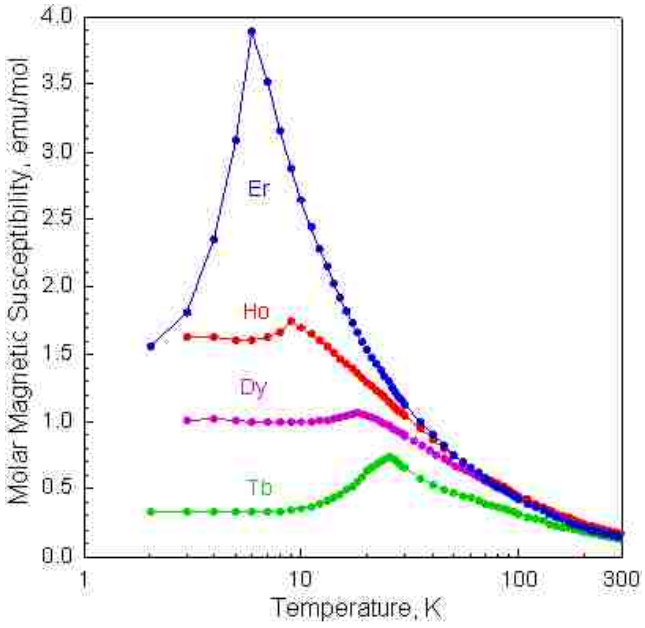

Figure 4.4a A semi logarithmic plot of the temperature dependence of the molar magnetic susceptibility of the Ln_4FeGa_{12} compounds measured in a 0.1 T applied dc field.

Ideally, one would like to subtract the molar magnetic susceptibility of Y_4FeGa_{12} from those of the rare-earth Ln_4FeGa_{12} compounds in order to obtain the temperature dependence of the contribution of the rare-earth magnetic ions to the molar magnetic susceptibility. But, rather surprisingly, the 2 K magnetic susceptibility observed for the Ln_4FeGa_{12} compounds is somewhat smaller than that of Y_4FeGa_{12}. Hence below 60 K, a 0.45, 1.53, 2.01, and 0.20 portion of the molar magnetic susceptibility of Y_4FeGa_{12} has been subtracted from the molar susceptibility of the Tb, Dy, Ho, and Er, compounds, respectively. The subtraction of the Y_4FeGa_{12} leads to a temperature dependence of the magnetic susceptibility that closely resembles that expected for the antiferromagnetic coupling of the *Ln* magnetic moments, with Néel temperatures, T_N, of 25, 44, 45, and 8 K, for the Tb, Dy, Ho, and Er compounds, respectively. The result of this subtraction is shown in Figure 4.5 for Tb_4FeGa_{12}. The various portions used in the subtraction may be a reflection of how frustrated are the iron moments, or of how extensively coupled are the rare-earth moments, or both. In this regard, it should be noted that the two compounds with the lower T_N values, i.e., Tb_4FeGa_{12} and Er_4FeGa_{12}, have the smallest contribution from the iron to their molar magnetic susceptibilities.

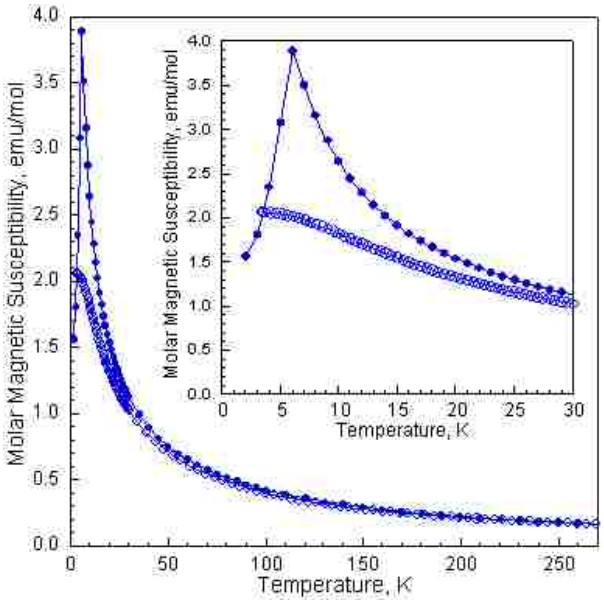

Figure 4.4b The temperature dependence of the magnetic susceptibility of Er_4FeGa_{12} measured at 0.1 T, solid points, and 5 T, larger open points. Inset: The temperature dependence between 3 and 30 K.

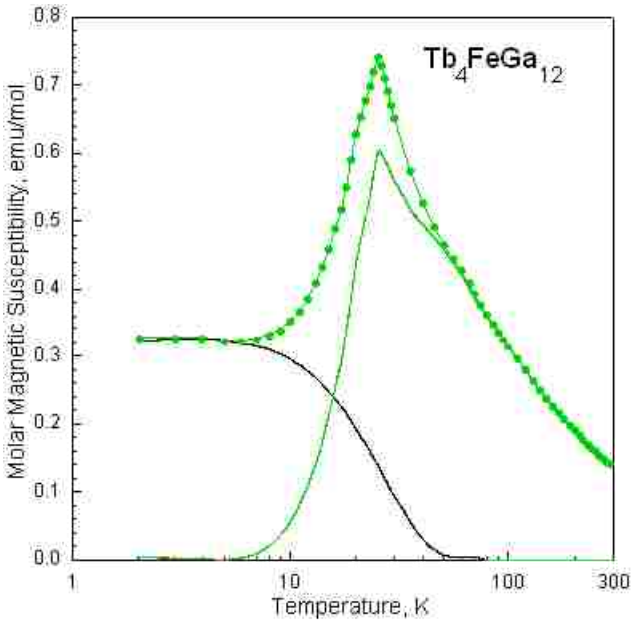

Figure 4.5 The temperature dependence of the molar magnetic susceptibility of Tb_4FeGa_{12} before, the green points, and after, the green line, subtraction of a 0.45 fraction of the molar magnetic susceptibility of Y_4FeGa_{12}, the black line.

The temperature dependence of the magnetic susceptibility of Er_4FeGa_{12}, measured in applied dc fields of 0.1 and 5 T, is shown in Figure 4.4b. In an applied field of 0.1 T, below a T_N of 8 K, the susceptibility decreases as expected for an antiferromagnet, whereas in an applied dc field of 5 T, the susceptibility increases as a result of a spin-flop transition.

There is an good linear correlation between the Weiss temperature, θ, and the de Gennes factor, $(g - 1)^2 J(J + 1)$, for the rare-earth Ln_4FeGa_{12} compounds, a correlation that indicates that the molar magnetic susceptibility is dominated by the *Ln* sublattice.

The field dependence of the 3 K magnetization of the rare-earth Ln_4FeGa_{12} compounds is shown in Figure 4.6. The magnetization of Dy_4FeGa_{12} increases linearly up to 9 T, in a fashion similar to that observed in Dy_4PtGa_{12} and Dy_4PdGa_{12}.[6] Below the critical fields of 6.5, 6, and 1 T, the magnetizations of Tb_4FeGa_{12}, Ho_4FeGa_{12}, and Er_4FeGa_{12} increase linearly with the applied field, as would be expected for an antiferromagnetic compound whose magnetic moments are

progressively polarized by the applied field. At the critical fields, metamagnetic transitions occur, and in Tb_4FeGa_{12} the metamagnetic transition is hysteretic between 7 and 8 T; above 8 T the magnetization is virtually saturated. In Ho_4FeGa_{12} the magnetization increases noticeably at the metamagnetic transition and more slowly, without saturating, above 7 T. In Er_4FeGa_{12} the magnetization increases substantially at the ca. 1 T metamagnetic transition and continues to increase without saturation even at 9 T. We propose that at the metamagnetic transition the *Ln* magnetic moments cant in the applied field and this canting angle decreases as the field is further increased up to 9 T. Even in a large field of 9 T the moments are not perfectly aligned in the applied field and the magnetization is not saturated.

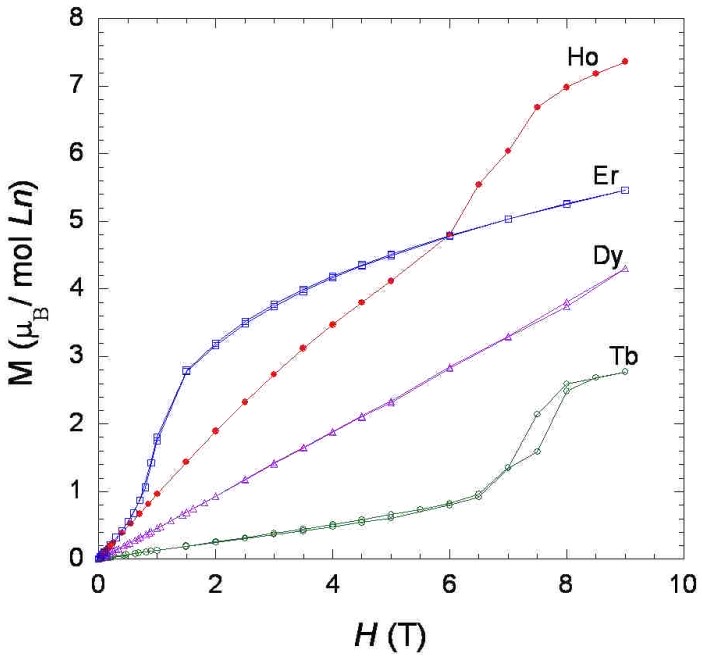

Figure 4.6 The field dependence of the magnetization of the Ln_4FeGa_{12} compounds measured at 3 K.

4.3.3 Resistivity Measurements

The temperature dependence of the electrical resistivities of the Ln_4FeGa_{12} compounds is shown in Figure 4.7. All the compounds show metallic behavior with increasing resistivity as the temperature increases. The residual resistivity ratios, ρ(295 K)/ρ(2 K), are 2.6, 2.7, 2.0, 1.9,

and 1.9, for the Y, Tb, Dy, Ho, and Er compounds, respectively, similar ratios that indicate that the crystal quality of the compounds is similar. Changes in the slope are observed near the ordering temperature, a change that is most obvious in Tb_4FeGa_{12} at ca. 25 K; variations in the slope suggest that the spin-disorder scattering changes at or below the ordering temperature. The magnetoresistance of the Ln_4FeGa_{12} compound containing Y, Tb, Dy, and Ho, displays a positive behavior at low temperature but do not exceed 15 %. The magnetoresistance of Er_4FeGa_{12} displays a negative behavior with a small value of –0.2 % at 9 T.

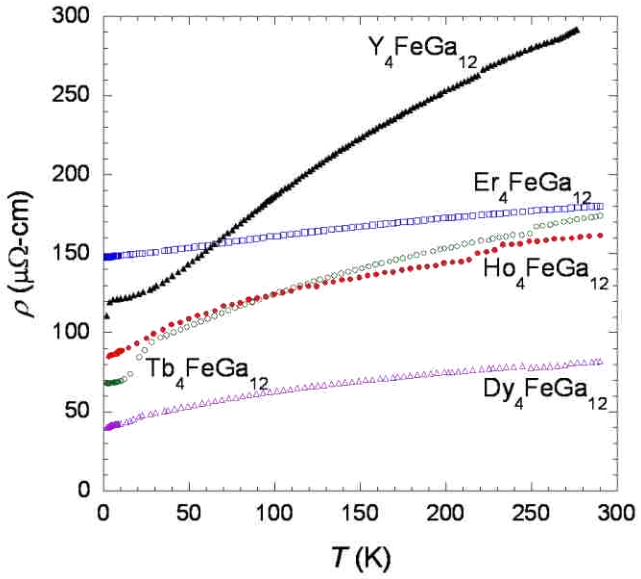

Figure 4.7 The temperature dependence of the electrical resistivity of the Ln_4FeGa_{12} compounds.

4.3.4 Mössbauer Spectra

Selected iron-57 Mössbauer spectra of the Y_4FeGa_{12}, Tb_4FeGa_{12}, Dy_4FeGa_{12}, and Er_4FeGa_{12} compounds, obtained between 4.2 and 295 K, are shown in Figure 4.8. The solid red lines in Figure 4.8 are the result of a single line fit (model 1) and the resulting isomer shifts, δ, and line widths, Γ, are given in Table 4.6; their temperature dependence is shown in Figure 4.9. T he single line fit and the absence of any quadrupole splitting is consistent with the cubic symmetry of the iron 2*a* site in the structure of these compounds.

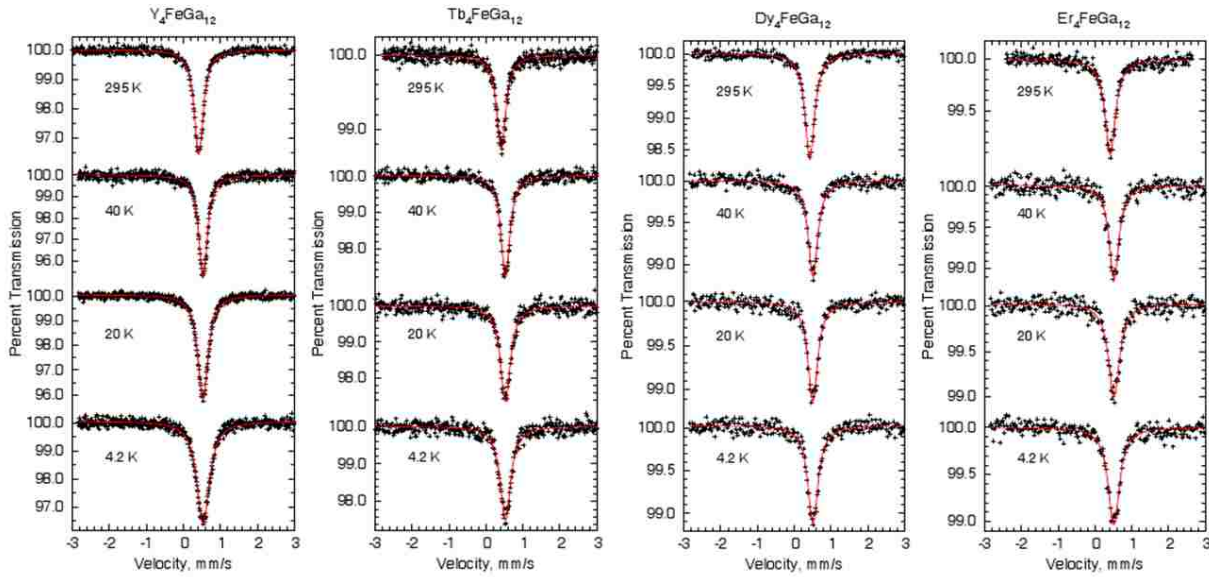

Figure 4.8 The iron-57 Mössbauer spectra of the Ln_4FeGa_{12} compounds obtained at the indicated temperatures. The solid red line is the result of a single line fit.

Table 4.6. Mössbauer Spectral Parameters for the Model 1 Fits

T, K	Isomer shift,[a] mm/s				Line width, mm/s			
	Y	Tb	Dy	Er	Y	Tb	Dy	Er
295	0.413(1)	0.415(2)	0.424(2)	0.403(3)	0.298(4)	0.296(7)	0.314(5)	0.36(1)
155	0.500(1)	0.489(3)	0.486(2)	0.484(3)	0.284(2)	0.30(1)	0.314(5)	0.37(1)
85	0.532(2)	0.525(2)	0.511(1)	0.514(3)	0.292(5)	0.299(5)	0.311(1)	0.361(5)
60	0.527(2)	0.529(2)	0.512(3)	0.504(3)	0.275(5)	0.297(5)	0.32(1)	0.35(1)
40	0.529(1)	0.526(2)	0.511(4)	0.504(4)	0.276(2)	0.287(6)	0.31(1)	0.35(1)
30	0.530(3)	-	-	-	0.287(8)	-	-	-
20	0.526(1)	0.524(3)	0.505(3)	0.504(4)	0.336(3)	0.324(9)	0.32(1)	0.39(1)
10	0.528(1)	0.533(1)	-	-	0.390(4)	0.338(2)	-	-
4.2	0.529(2)	0.524(3)	0.509(4)	0.502(4)	0.406(5)	0.342(9)	0.34(1)	0.39(1)

[a]Relative to 295 K α-iron powder.

In agreement with the expected second-order Doppler shift, the temperature dependencies of the isomer shifts are well fit with the Debye model for a solid,[16] see the solid lines in Figure 4.9, left panel. The characteristic Mössbauer temperatures corresponding to these fits are 457(19), 406(26), 610(35), and 499(20) K, for Y_4FeGa_{12}, Tb_4FeGa_{12}, Dy_4FeGa_{12}, and Er_4FeGa_{12},

respectively. Except for Dy_4FeGa_{12} these temperatures are only somewhat above the range of 265 to 410 K observed[17,18] for several Ln_2Fe_{17} and $LnCo_{4-x}Fe_xB$ compounds.

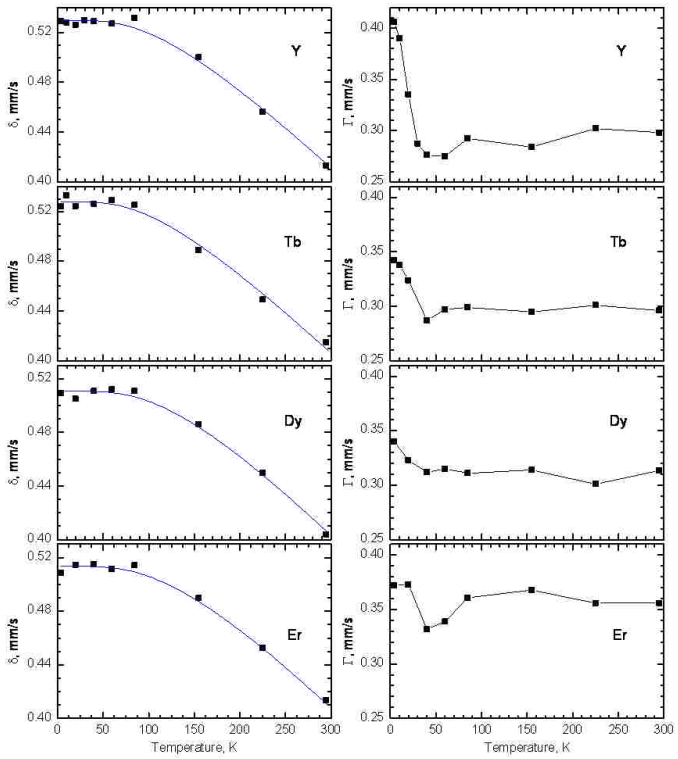

Figure 4.9 The temperature dependence of the isomer shift, left, and of the line width, right, for the Ln_4FeGa_{12} compounds.

Two different temperature dependencies of the line width, Γ, are observed, see Figure 4.9. Below 40 K the line width observed for Y_4FeGa_{12} increases significantly upon cooling. In contrast, below 40 K the line width observed for Tb_4FeGa_{12}, Dy_4FeGa_{12}, and Er_4FeGa_{12} increases only slightly upon cooling. This different behavior may be related to the differences in the magnetic properties of Y_4FeGa_{12} as compared to those of Tb_4FeGa_{12}, Dy_4FeGa_{12}, and Er_4FeGa_{12}.

The molar magnetic susceptibility of Y_4FeGa_{12} increases continuously below 36 K in a ferromagnetic-like fashion, see Figure 4.3, whereas those of Tb_4FeGa_{12}, Dy_4FeGa_{12}, and Er_4FeGa_{12} exhibit maxima at 26, 18.5, and 6 K, respectively, see Figure 4.4. As a consequence, the Mössbauer spectra of Y_4FeGa_{12} obtained below 60 K have alternatively been fit with one

symmetric sextet, herein referred to as model 2, with a line width constrained to 0.275 mm/s, the value obtained with model 1 at 60 K; the resulting isomer shifts and hyperfine fields are given in Table 4.7. It should be noted that the isomer shift is independent of the model used.

Table 4.7. Mössbauer Spectral Parameters for the Model 2 Fits

T, K	Isomer shift,[a] mm/s				Hyperfine field, T			
	Y	Tb	Dy	Er	Y	Tb	Dy	Er
40	0.529(1)	-	-	-	0.18(4)	-	-	-
30	0.530(3)	-	-	-	0.28(6)	-	-	-
20	0.526(1)	0.525(3)	0.505(3)	-	0.49(1)	0.38(5)	0.33(6)	-
10	0.527(1)	0.533(3)	-	-	0.71(1)	0.47(3)	-	-
4.2	0.530(2)	0.523(3)	0.509(4)	0.502(4)	0.76(1)	0.48(4)	0.40(6)	0.44(6)

[a]Relative to 295 K α-iron powder.

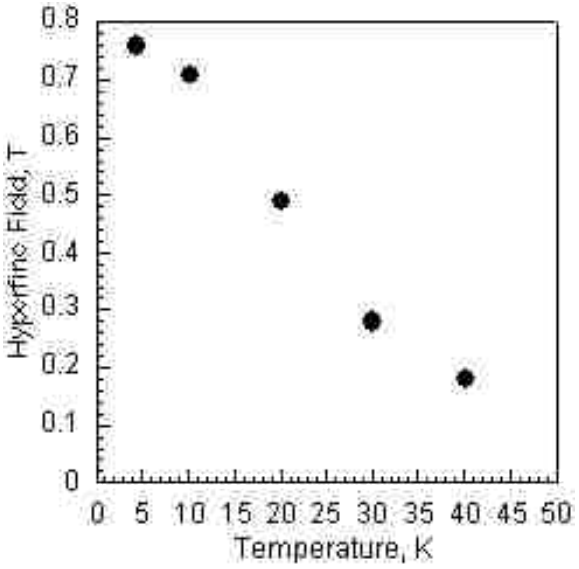

Figure 4.10 The temperature dependence of the hyperfine field in Y_4FeGa_{12} obtained from a sextet fit with model 2.

The temperature dependence of the hyperfine field is shown in Figure 4.10. The 4.2 K hyperfine field of 0.76(1) T is very small, and if the usual conversion factor of 15 T per μ_B is used, this field corresponds to an iron magnetic moment of 0.05 μ_B, a value that is smaller than the value of 0.13 μ_B observed at 3 K in a field of 0.03 T. A fit with model 2 of the Mössbauer

spectra of the Ln_4FeGa_{12} compounds, where *Ln* is Tb, Dy, or Er, below their respective Néel temperature, yields the parameters given in Table 4.7.

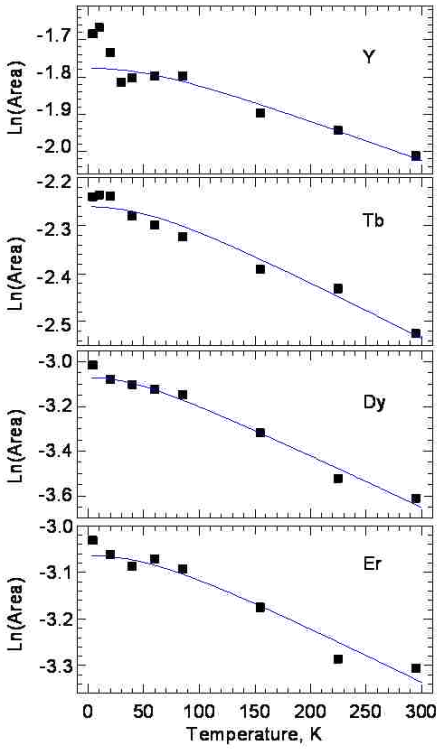

Figure 4.11 The temperature dependence of the logarithm of the spectral absorption area for the Ln_4FeGa_{12} compounds, with *Ln* = Y, Tb, Dy and Er. The blue solid lines are the result of a fit with the Debye model for the lattice vibrations. For Y_4FeGa_{12}, only the areas obtained above 60 K are used in the fit.

The temperature dependence of the logarithm of the spectral absorption area for the Ln_4FeGa_{12} compounds containing Y, Tb, Dy, and Er, is shown in Figure 4.11. The solid lines are the result of a fit with the Debye model for the lattice vibrations. The resulting Debye temperatures are 350(20), 331(19), 239(5), and 345(14) K for Y, Tb, Dy, and Er, respectively. These Debye temperatures are related to the mean-square vibrational displacements of the iron nuclei in the lattice, whereas the Mössbauer temperatures obtained from the fit of the temperature dependence of the isomer shifts are related to the mean-square vibrational velocities of the iron nuclei. There is no model-independent relation between these two temperatures, and it is usual to observe larger Mössbauer temperatures than Debye temperatures, because the

former probe the high-frequency phonons, whereas the latter probe the low-frequency phonons. In the case of the Ln_4FeGa_{12} compounds, the Mössbauer temperature is approximately 1.5 times the Debye temperature, a factor that is smaller than observed[19,20] in organometallic compounds.

4.4 Discussion

We can rationalize the magnetic behavior of Y_4FeGa_{12} as follows. The shortest iron-iron distance in Y_4FeGa_{12} is 7.4175(4) Å, which is the half diagonal of the cubic unit cell, a diagonal that passes through a yttrium near neighbor. The next shortest iron-iron distance in Y_4FeGa_{12} is 8.5650(4) Å, the edge of the unit cell that passes through two gallium near neighbors. Neither of these exchange pathways is favorable for ferromagnetic exchange coupling. Hence, there is no magnetic exchange coupling between the iron atoms, that may be considered as isolated. The absence of coupling is supported by the only broadened single line Mössbauer spectra observed from 295 to 4.2 K. The broadening of the single line observed below 36 K does not result from ordered magnetic moments carried by the iron atoms but from the slow magnetic relaxation of the iron magnetic moments on the Mössbauer time scale of 5×10^{-8} s, a slow relaxation that tends to align the iron magnetic moments along their single-ion anisotropy axis. Hence, the fitted hyperfine field of 0.76 T in model 2 should be understood as an effective field. In the applied dc field of 0.1 T used in the magnetic measurements, the iron magnetic moments align in the field and a ferromagnetic-like contribution to the magnetic susceptibility is observed.

The broadening of the single line Mössbauer spectra observed in the Ln_4FeGa_{12} compounds, when *Ln* is Tb, Dy, and Er, or the associated extremely small hyperfine fields, may be understood if the eight rare-earth ion near neighbors of the iron are antiferromagnetically coupled and create a zero or nearly zero transferred hyperfine field at the iron nucleus. In this case, the iron magnetic moments are randomly oriented as they would be in a paramagnetic compound, and a narrow single line Mössbauer spectrum is observed.

The isomer shifts observed herein are between 0.50 and 0.53 mm/s at 4.2 K and ca. 0.40 mm/s at 295 K. In the Ln_2Fe_{17},[21-24] $LnFe_{11}Ti$,[25] and $LnCo_{4-x}Fe_xB$[26,27] compounds, the isomer shifts are in the range of zero to 0.2 mm/s at 4.2 K. In contrast, for both iron in a gallium host[16] and for the iron in Fe_3Ga_4,[28] the isomer shifts are significantly more positive, i.e., 0.50 mm/s and 0.31 mm/s at 4.2 and 295 K, respectively. In all the gallium containing compounds, the iron atoms have gallium near neighbors and share their 3*d* electrons with these gallium near neighbors. This 3*d* electron sharing increases the isomer shift and gives an iron(III)-like character to the iron atoms in the Ln_4FeGa_{12} compounds. The isomer shift decreases from Y to Er in agreement with the lanthanide contraction and the decrease in the unit-cell lattice parameter.

4.5 Conclusion

Single crystals of Ln_4FeGa_{12}, where *Ln* is Y, Tb, Dy, Ho, and Er, have been synthesized and their structural, magnetic, and electric properties have been investigated between 3 and 320 K. The iron-57 Mössbauer spectra have also been obtained between 4.2 and 295 K.

Y_4FeGa_{12} exhibits slow paramagnetic relaxation of the well isolated iron magnetic moment on the Mössbauer time scale below 40 K in a zero applied field and an alignment of the iron magnetic moment below 36 K in an applied dc field of 0.1 T in the magnetic susceptibility measurements. The rare-earth containing Ln_4FeGa_{12} compounds exhibit an antiferromagnetic behavior of the rare-earth magnetic moments with Néel temperatures of 25, 44, 45, and 8 K, with no significant magnetic hyperfine field on the iron. Hence, the antiferromagnetic behavior is associated only with the *Ln* magnetic moments.

4.6 References

(1) Thomas, E. L.; Millican, J. N.; Okudzeto, E. K.; Chan, J. Y. *Comments Inorg. Chem.* **2006**, *27*, 1-39.

(2) Cho, J. Y.; Millican, J. N.; Capan, C.; Sokolov, D. A.; Moldovan, M.; Karki, A. B.; Young, D. P.; Aronson, M. C.; Chan, J. Y. *Chem. Mater.* **2008**, *20*, 6116-6123.

(3) Millican, J. N.; Macaluso, R. T.; Young, D. P.; Moldovan, M.; Chan, J. Y. *J. Solid State Chem.* **2004**, *177*, 4695-4700.

(4) Williams, W. M.; Macaluso, R. T.; Moldovan, M.; Young, D. P.; Chan, J. Y. *Inorg. Chem.* **2003**, *42*, 7315-7318.

(5) Williams, W. M.; Moldovan, M.; Young, D. P.; Chan, J. Y. *J. Solid State Chem.* **2005**, *178*, 52-57.

(6) Cho, J. Y.; Moldovan, M.; Young, D. P.; Chan, J. Y. *J. Phys.: Condens. Matter* **2007**, *19*, 266224.

(7) Leithe-Jasper, A.; Schnelle, W.; Rosner, H.; Senthilkumaran, N.; Rabis, A.; Baenitz, M.; Gippius, A.; Morozova, E.; Mydosh, J. A.; Grin, Y. *Phys. Rev. Lett.* **2003**, *91*, 037208.

(8) Leithe-Jasper, A.; Schnelle, W.; Rosner, H.; Baenitz, M.; Rabis, A.; Gippius, A. A.; Morozova, E. N.; Borrmann, H.; Burkhardt, U.; Ramlau, R.; Schwarz, U.; Mydosh, J. A.; Grin, Y.; Ksenofontov, V.; Reiman, S. *Phys. Rev. B* **2004**, *70*, 214418.

(9) Viennois, R.; Ravot, D.; Terki, F.; Hernandez, C.; Charar, S.; Haen, P.; Paschen, S.; Steglich, F. *J. Magn. Magn. Mater.* **2004**, *272*, E113-E114.

(10) Leithe-Jasper, A.; Kaczorowski, D.; Rogl, P.; Bogner, J.; Reissner, M.; Steiner, W.; Wiesinger, G.; Godart, C. *Solid State Commun.* **1999**, *109*, 395-400.

(11) Sheldrick, G. M. In *SHELXL-97, Program for Refinement of Crystal Structures*; University of Göttingen: Göttingen, Germany, **1997**.

(12) Vasilenko, L. O.; Noga, A. S.; Grin, Y. N.; Koterlin, M. D.; Yarmolyuk, Y. P. *Russ. Metall.* **1988**, 216-220.

(13) Zhuravleva, M. A.; Wang, X. P.; Schultz, A. J.; Bakas, T.; Kanatzidis, M. G. *Inorg. Chem.* **2002**, *41*, 6056-6061.

(14) Emsley, J. *The Elements* Oxford University Press, **1999**.

(15) Pelleg, J.; Kimmel, G.; Dayan, D. *J. Less-Common Met.* **1981**, *81*, 33-44.

(16) Shenoy, G. K.; Wagner, F. E.; Kalvius, G. M. in *Mössbauer Isomer Shifts*, Shenoy, G. K.; Wagner, F. E., Eds., North-Holland, Amsterdam, (1978) p. 49.

(17) Long, G. J.; Isnard, O.; Grandjean, F. *J. Appl. Phys.* **2002**, *91*, 1423.

(18) Mayot, H.; Isnard, O.; Grandjean, F.; Long, G. J. *J. Appl. Phys.*, **2009**, *105*, 113908 (7 pages).

(19) Reger, D. L.; Elgin, J. D.; Smith, M. D.; Grandjean, F.; Rebbouh, L.; Long, G. J. *Polyhedron* **2006**, *25*, 2616; Reger, D. L.; Gardinier, J. R.; Bakbak, S.; Gemmill, W.; Smith, M. D.; Rebbouh, L.; Grandjean, F.; Shahin, A. M.; Long, G. J. *J. Amer. Chem. Soc.* **2005**, *127*, 2303; Reger, D. L.; Gardinier, J. R.; Smith, M. D.; Shahin, A. M.; Long, G. J.; Rebbouh, L.; Grandjean, F. *Inorg. Chem.* **2005**, *44*, 1852; Jiao, J.; Long, G. J.; Rebbouh, L.; Grandjean, F.; Beatty, A. M.; Fehlner, T. P. *J. Am. Chem. Soc.* **2005**, *127*, 17819.

(20) Owen, T.; Grandjean, F.; Long, G. J.; Domasevitch, K. V.; Gerasimchuk, N. *Inorg. Chem.* **2008**, *47*, 8704-8713.

(21) Long, G. J.; Mishra, S.; Pringle, O. A.; Grandjean, F.; Buschow, K. H. J. *J. Appl. Phys.* **1994**, *75*, 5994.

(22) Hautot, D.; Long, G. J.; Ezekwenna, P. C.; Grandjean, F.; Middleton, D. P.; Buschow K. H. J. *J. Appl. Phys.* **1998**, *83*, 6736.

(23) Grandjean, F.; Hautot, D.; Long, G. J.; Isnard, O.; Miraglia, S.; Fruchart D. *J. Appl. Phys*. **1999**, *85*, 4654.

(24) Isnard, O.; Hautot, D.; Long, G. J.; Grandjean F. *J. Appl. Phys.* **2000**, *88*, 2750.

(25) Piquer, C.; Grandjean, F.; Isnard, O.; Long, G. J. *J. Phys.: Conden. Matter* **2006**, *18*, 205.

(26) Long, G. J.; Hermann, R. P.; Grandjean, F.; Chacon, C.; Isnard, O. *J. Phys.: Condens. Matter* **2006**, *18*, 10765.

(27) Mayot, H.; Isnard, O.; Grandjean, F.; Long, G. J. *J. Appl. Phys*. **2008**, *103*, 94093917 (6 p).

(28) Kobeissi, M. A.; Hutchings, J. A.; Appleyard, P. G.; Thomas, M. F.; Booth, J. G. *J. Phys.: Condens. Matter*, **1999**, *11*, 6251.

CHAPTER 5. CONCLUSION AND FUTURE WORK

5.1 Conclusion

The aim of this dissertation is the study of the structure-property relationships in the *Ln*-*M*-*X* systems (*Ln* = lanthanides, *M* = Fe and Co; *X* = Ga and Sn). The main feature of the structures investigated is the LnX_{12} cuboctahedra ($AuCu_3$ structure type),[1] a structural unit observed in several heavy fermion compounds.[2] We have synthesized single crystals of $Ln_3Co_4Sn_{13}$ (*Ln* = Pr, Nd, Sm, Gd and Tb),[2] $Ln_7Co_6Sn_{23}$ (*Ln* = Dy and Ho),[3] $Ln_5Co_6Sn_{18}$ (*Ln* = Er and Tm),[3] $Yb_3Co_4Sn_{12+x}$ (x = 0.79, 0.90), $YbCoGa_5$[4] and Ln_4FeGa_{12} (*Ln* = Y, Tb, Dy, Ho and Er).[5] Many of the compounds adopt structure types consisting of the $AuCu_3$ substructure with transition metals filling the octahedral or tetrahedral holes in the structure. In the case of the *Ln*-Co-Sn compounds, $LnSn_{12}$ cuboctahedra fill voids created by the arrangement of $CoSn_6$ trigonal prisms. In $Ln_7Co_6Sn_{23}$ and $Ln_5Co_6Sn_{18}$ the lanthanides form both $LnSn_{12}$ cuboctahedra and $LnSn_{10}$ truncated cuboctahedra. The structure of $YbCoGa_5$ consists of $YbCo_3$ cuboctahedra and CoGa2 rectangular prisms.

We have also studied the formation of compounds as a function of rare-earth elements to determine their stability. In the *Ln*-Co-Sn system, we observe that larger *Ln* (Pr-Tb) favor the $Yb_3Rh_4Sn_{13}$ structure type while the smaller *Ln* (Dy-Tm) crystallize in the $Ho_7Co_6Sn_{23}$ and $Er_5Rh_6Sn_{18}$ structure types.[3] With the exception of the Pr analogue, the compounds that crystallize in the $Yb_3Rh_4Sn_{13}$ structure type display antiferromagnetic behavior with their Neel temperatures following de Gennes factor with a maximum at $Gd_3Co_4Sn_{13}$.[2] Apart from $Dy_7Co_6Sn_{23}$ the compounds containing the latter *Ln* (Ho-Tm), all display paramagnetic behavior with Weiss temperatures close to zero. The lattice parameter and cell volume of $Yb_3Co_4Sn_{12+x}$ suggest that the oxidation state of Yb is close to +2, allowing a larger rare earth analogue to

adopt the $Yb_3Rh_4Sn_{13}$ structure type. Understanding specific structural stabilities and the coordination preferences of constituent elements enables the target synthesis of specific compounds. Our goal is to bridge the gap between specific structure types, the elements present in these compounds, and understanding their electronic and magnetic properties.

We have also studied the incorporation of magnetic transition metals (Fe and Co) into known ternary intermetallic structure types to determine the effects of their physical properties. We have synthesized Ln_4FeGa_{12} compounds for *Ln* = Y, Tb-Er. For the compounds where *Ln* is a magnetic lanthanide, an antiferromagnetic transition is observed. The Néel temperature and Weiss temperature scale well with the de Gennes factor indicating strong RKKY interaction in these compounds. The scaling coincides with the decrease in volume from Tb-Er. Interestingly the compound containing the nonmagnetic lanthanide Y, displays ferromagnetic behavior at 33 K, despite the observation that the Fe sublattice in the *Ln* = Tb-Er appears nonmagnetic.

During our investigating of *Ln*-*M*-Ga compounds, we have discovered that the stability of certain structure types depend on the size of the constituent elements and the stable binary impurities that can grow these systems. In the *Ln*-Fe-Ga system, we have found that the Y_4PdGa_{12} structure can only be synthesized for compounds that contain small rare-earth elements, *i.e.* Tb-Tm. Coincidentally the stable *Ln*-Ga binary for small rare-earths is $LnGa_3$ ($AuCu_3$ structure type) and the incorporation of Fe into the system leads to the formation of Ln_4FeGa_{12}. The structure of Ln_4FeGa_{12} consists of consists of $LnGa_{12}$ cuboctahedra and $FeGa_6$ octahedra. For larger rare-earths such as Ce, the stable product is $CeGa_6$ or variants of this structure type. It would be useful to perform in-situ powder X-ray diffraction experiments of the Ln-Fe-Ga phase. This would give an insight into crystal structure formation and the growth and synthesis of ternary phases. It is also worthwhile to note that a stable binary in the *Ln*-Sn system

is LnSn$_3$ ($AuCu_3$ structure type) of which $Ln_3Co_4Sn_{13}$, $Ln_7Co_6Sn_{23}$ and $Ln_5Co_6Sn_{18}$ are derivatives.

5.2 Future Work

As stated earlier, our goal is to explore ternary intermetallic systems with a specific structure type. Some structure types explored in our group include the $HoCoGa_5$,[6] Ho_2CoGa_8,[6] $Yb_3Rh_4Sn_{13}$[7] and the Y_4PdGa_{12}[8] structure types. Some compounds that adopt the aforementioned structure types also display the coexistence of heavy fermion behavior and superconductivity. While exploring the Yb-Co-Ga system we have synthesized single crystals of $YbCoGa_5$,[4] a compound not previously reported in the Ln_nCoGa_{3n+2} (n = 1, 2, ∞; Ln = Gd-Tm, Lu and Y) family.[6] The isostructural compound $SmCoGa_5$ was also recently synthesized.[9] The discovery of the Yb and Sm compounds opens the possibility of discovery of other lanthanide based compounds in this family i.e. Yb_2CoGa_8, Sm_2CoGa_8 and Eu_2CoGa_8. Lapunova et al. reported the structure of Ln_2FeGa_8 with Ln = Tb-Tm.[10] Co with an atomic radius of 1.25 Å[11] and Fe with 1.24 Å[11] are both transition metals that can be incorporated in the Ln_nMGa_{3n+2} structure type. Using our expertise for growing single crystals it would be worthwhile to explore the Ln-Fe-Ga system to try and synthesize single crystals of $YbFeGa_5$ and Yb_2FeGa_8. We could arc melt the constituent elements in a specific ratio (1:1:5 or 2:1:8) and use a seed of a Yb-Fe-Ga ternary to attempt to grow single crystals of $YbFeGa_5$ and Yb_2FeGa_8.

The effect of pressure on the interplay between magnetism and superconductivity was studied on Ce_nRhIn_{3n+2} (n = 1, 2).[12, 13] The application of hydrostatic pressure was found to induce superconductivity in the above compounds. The effects of chemical pressure by doping were studied on $YbCu_2Si_2$.[14] Upon the substitution of Cu with Ni, the nonmagnetic state of $YbCu_2Si_2$ was changed to a magnetic state.[14] Although $YbCoGa_5$ displays Pauli paramagnetic

behavior and Yb in the compound is divalent.[4] It would be interesting to study the effect of chemical pressure on $YbCoGa_5$ by substituting Co with Fe.

5.3 References

(1) Wilson, A. J. C., *Proceedings of the Royal Society of London, Series A: Mathematical, Physical and Engineering Sciences* **1943,** *181*, 360-8.

(2) Thomas, E. L.; Millican, J. N.; Okudzeto, E. K.; Chan, J. Y., *Comments Inorg. Chem.* **2006,** *27*, 1-39.

(3) Okudzeto, E. K.; Thomas, E. L.; Moldovan, M.; Young, D. P.; Chan, J. Y., *Physica B* **2008,** *403*, 1628-1629.

(4) Okudzeto, E. K.; Kuga, K.; Nakatsuji, S.; Chan, J. Y., *Cryst. Growth Des.* **2009,** *9*, 1956-1959.

(5) Okudzeto, E. K.; Karki, A. B.; Young, D. P.; Sougrati, M. T.; Grandjean, F.; Long, G. J.; Chan, J. Y., *Inorg. Chem.* **2009**, Submitted

(6) Grin, Y. N.; Yarmolyuk, Y. P.; Gradyshevsky, E. I., *Kristallografiya* **1979,** *24*, 242-246.

(7) Hodeau, J. L.; Chenavas, J.; Marezio, M.; Remeika, J. P., *Solid State Commun.* **1980,** *36*, 839-845.

(8) Vasilenko, L. O.; Noga, A. S.; Grin, Y. N.; Koterlin, M. D.; Yarmolyuk, Y. P., *Russ. Metall.* **1988**, 216-220.

(9) Jia, Y.; Belin, C.; Tillard, M.; Lacroix-Orio, L.; Zitoun, D.; Feng, G., *Inorg. Chem.* **2007,** *46*, 4177-4186.

(10) Lapunova, R. V.; Grin, Y. N.; Yarmolyuk, Y. P., *Dopov. Akad. Nauk Ukr. RSR, Ser. B: Geol., Khim. Biol. Nauki* **1984**, 43-4.

(11) Emsley, J., *The Elements*. Oxford University Press: New York, **1999**.

(12) Hegger, H.; Petrovic, C.; Moshopoulou, E. G.; Hundley, M. F.; Sarrao, J. L.; Fisk, Z.; Thompson, J. D., *Phys. Rev. Lett.* **2000,** *84*, 4986-4989.

(13) Nicklas, M.; Sidorov, V. A.; Borges, H. A.; Pagliuso, P. G.; Petrovic, C.; Fisk, Z.; Sarrao, J. L.; Thompson, J. D., *Phys. Rev. B* **2003,** *67*, 020506.

(14) Andreica, D.; Amato, A.; Gygax, F.; Pinkpank, M.; Schenck, A., *Physica B* **2000,** *289-290*, 24-27.

APPENDIX 1 INVESTIGATING THE STRUCTURE OF $Ni_{1-x}Co_xGa_2S_4$ (x = 0, 0.2, 0.3, 0.5) AND $Ni_{0.9}Mn_{0.1}Ga_2S_4$

A1.1 Introduction

Two dimensional (2D) antiferromagnetic materials that have triangular lattice structures have been proposed as candidates for spin liquid behavior.[1] Spin liquids are materials whose electrons/spins are not frozen in place at low temperatures and their spins are allowed to move freely. In order for a compound to be considered as a spin liquid it should have a frustrated lattice with site disorder/ quantum fluctuations.[1] Figure A1.1 shows such a triangular lattice system where a geometric frustrated antiferromagnet is created as a result of symmetry constraint. In spin liquids, no singularity is observed in specific heat measurements at low temperatures and the specific heat data should also show a power-law behavior with the absence of long range magnetic ordering.[1] Considerable research has been undertaken on geometric frustrated 2D antiferromagnetic compounds but only a few of them do not exhibit long range order. Some frustrated antiferromagnets that have been proposed as candidates for spin liquid behavior include ^{3}He layered film,[2, 3] $SrCr_{9p}Ga_{12-9P}O_{19}$,[4] Cs_2CuCl_4,[5] $NiGa_2S_4$,[6] and the organic compound κ-$(BEDT\text{-}TTF)_2Cu_2(CN)_3$.[7]

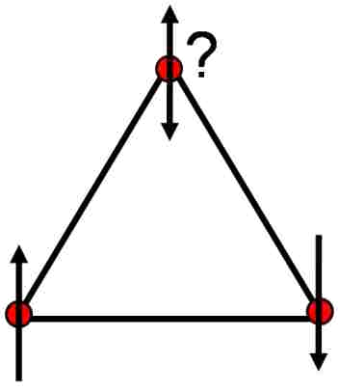

Figure A1.1 Projection of a geometric frustrated triangular lattice. The arrows represent magnetic spins and the red dots represent lattice points.

$NiGa_2S_4$ is a two dimensional layered compound and can be viewed as slabs of NiS_2 layers sandwiched between two GaS layers.[8] Each layer is separated from another by weak van der Waals forces. The Ni^{2+} ions with the electronic configuration $t_{2g}^6e_g^2$ and spin S = 1 are responsible for magnetism in the compound. The Ni^{2+} ions are arranged in a triangular lattice in the structure making it a candidate for geometric frustration. Although $NiGa_2S_4$ is a bulk 2D antiferromagnet with an exact triangular lattice no spin glass ordering has been observed down to low temperature.[6]

To understand the mechanisms in spin liquids, researchers have studied the effects of frustration and disorder at low temperature in these compounds. However in most spin glasses, geometric frustration is induced by disorder.[1] To understand the stability of the 2D coherent behavior in the $NiGa_2S_4$, Nakatsuji *et al* grew single crystals of the isostructural compound $FeGa_2S_4$.[9] Several similarities between $NiGa_2S_4$ and $FeGa_2S_4$, (both have a trigonal lattice and display T^2 dependence of C_M) suggest that both compounds have the same mechanism for 2D coherent behavior.[9] The non magnetic impurity Zn^{2+} (S = 0) as well as the magnetic impurity Fe^{2+} (S = 2) have been introduced into the crystal structure of $NiGa_2S_4$ and still display T^2 dependent C_M.[10] However when Co^{2+} (S = 3/2) and Mn^{2+}(S = 5/2) are substituted into $NiGa_2S_4$, an emergences of a spin glass phase is observed.[11] The purpose of this work is the full structure determination of Co and Mn doped $NiGa_2S_4$ single crystals to confirm composition and study the role of the transition metal on the spin glass phase observed in the doped compounds. Results obtained from single crystal XRD can also be used to determine the angles of superexchange pathways to determine if the Co concentration maybe the origin of enhancement of Weiss temperature observed in Co doped samples.

A1.2 Single Crystal X-ray Diffraction

Crystal fragments with maximum dimensions of ~ 0.03 x 0.08 x 0.08 mm^3 were mechanically selected for the structural analysis of $Ni_{1-x}Co_xGa_2S_4$ (x = 0, 0.2, 0.3 and 0.5) and $Ni_{0.9}Mn_{0.1}Ga_2S_4$. The crystals were glued on the tip of a glass fiber and mounted on a Nonius Kappa CCD diffractometer outfitted with Mo K_α radiation (λ = 0.71073Å). Data collection was taken at 298 K. Additional crystallographic parameters are included in Table A1.1. The structures of $Ni_{1-x}Co_xGa_2S_4$ (x = 0, 0.2, 0.3 and 0.5) and $Ni_{0.9}Mn_{0.1}Ga_2S_4$ were solved using the model of the parent compound $FeGa_2S_4$[12] and refined using SHELXL97.[13] The initial refinement resulted in an R value of ~ 80 %. Usually for a trigonal cell the *a* and *b* axis are well defined. However because of the 3-fold symmetry in the cell setting, these axis can be redefined by rotating the cell 60° around *c*. This results in $\vec{A} = \vec{a} + \vec{b}$, and $\vec{B} = -\vec{a}$, with the c-axis remaining the same. The initial data collected was indexed using the cell setting in Figure A1.2a. This setting resulted in a high R value after refinement. To correct this error, the cell was transformed by a 60° rotation, and thereby resulting in the cell setting shown in Figure A1.2b.

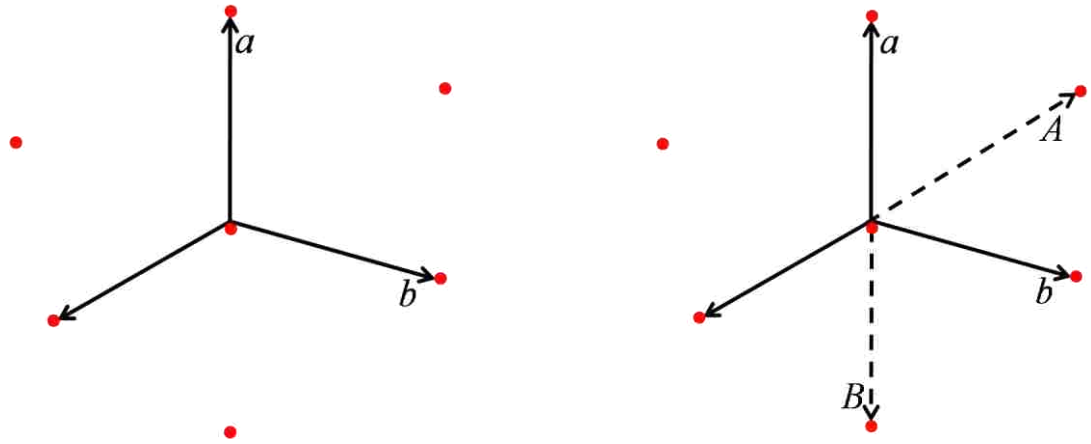

Figure A1.2 (a) Projection of a trigonal lattice, showing the *a* and *b* axis. The c-axis is projected into the paper. (b) Projection of the transformed trigonal cell showing the new axis *A* and *B*. The c-axis remains the same. (The red dots represent lattice point)

After refinement the new R values obtained were 0.0598, 0.0366, 0.0304, 0.0347, 0.0269 for $Ni_{1-x}Co_xGa_2S_4$ (x = 0, 0.2, 0.3 and 0.5) and $Ni_{0.9}Mn_{0.1}Ga_2S_4$ respectively. The data were then corrected for extinction effects and the displacement parameters were refined as anisotropic. A list of atomic positions, Wyckoff symmetry, and anisotropic displacement parameters are shown in Table A1.2.

Table A1.1 Crystallographic Parameters for $Ni_{1-x}Co_xGa_2S_4$ (x = 0, 0.2, 0.3, 0.5) and $Ni_{0.9}Mn_{0.1}Ga_2S_4$

Compound	$NiGa_2S_4$	$Ni_{0.8}Co_{0.2}Ga_2S_4$	$Ni_{0.7}Co_{0.3}Ga_2S_4$	$Ni_{0.5}Co_{0.5}Ga_2S_4$	$Ni_{0.9}Mn_{0.1}Ga_2S_4$
Space Group	*P*-3m1	*P*-3m1	*P*-3m1	*P*-3m1	*P*-3m1
a (Å)	3.6270(5)	3.6322(3)	3.6342(3)	3.6387(4)	3.633(2)
c (Å)	11.9990(10)	11.9998(6)	12.0035(7)	12.0095(13)	12.013(5)
V (Å^3)	136.70(3)	137.102(17)	137.295(18)	137.70(3)	137.31(12)
Z	1	1	1	1	1
Dimensions (mm^3)	0.03x0.08x0.08	0.03x0.08x0.08	0.03x0.05x0.08	0.03x0.08x0.05	0.05x0.05x0.05
Temperature (K)	298(2)	298(2)	298(2)	298(2)	298(2)
ρ (g/cm3)	3.965	3.953	3.948	3.936	3.910
θ Range	3.40-29.90	3.40-29.89	3.39-30.01	6.48-29.97	3.39-30.02
Collected reflections	477	511	521	423	543
Unique reflections	185	189	190	187	199
h	$-5 \leq h \leq 5$	$-5 \leq h \leq 5$	$-4 \leq k \leq 4$	$-4 \leq k \leq 4$	$-5 \leq h \leq 5$
k	$-3 \leq k \leq 3$	$-3 \leq k \leq 3$	$-3 \leq k \leq 3$	$-5 \leq h \leq 5$	$-3 \leq k \leq 3$
l	$-14 \leq k \leq 16$	$-16 \leq k \leq 14$	$-16 \leq k \leq 13$	$-16 \leq k \leq 15$	$-16 \leq k \leq 16$
$\Delta\rho_{max}$ (eÅ^{-3})	3.755	0.708	0.715	2.218	0.614
$\Delta\rho_{min}$ (eÅ^{-3})	-3.285	-2.859	-2.012	-1.043	-1.800
R_1 (*F*)[a]	0.0598	0.0366	0.0304	0.0347	0.0269
R_w[b]	0.1503	0.0834	0.0749	0.0881	0.0623

[a] $R_1 = \Sigma||F_o| - |F_c||/\Sigma|F_o|$

[b] $R_w = [\Sigma\ [w\ (F_o^2 - F_c^2)^2]/\ \Sigma\ [w\ (F_o^2)^2]]^{1/2}$; w = $1/[\sigma^2(F_o^2) + (0.0451P)2 + 3.7576P]$, w = $1/[\sigma^2(F_o^2) + (0.0338P)2 + 0.0258P]$, w = $1/[\sigma^2(F_o^2) + (0.0292P)^2 + 0.3502P]$, w = $1/[\sigma^2(F_o^2) + (0.0308P)^2 + 0.3374P]$, for *M** $Ni_{1-x}Co_x$ for x = 0, 0.2, 0.3, 0.5 respectively, and w = $1/[\sigma^2(F_o^2) + (0.0347P)^2 + 0.0621P]$ for $Ni_{0.9}Mn_{0.1}Ga_2S_4$.

Table A1.2 Atomic Positions and Thermal Parameters for $Ni_{1-x}Co_xGa_2S_4$ (x = 0, 0.2, 0.3 0.5) and $Ni_{0.9}Mn_{0.1}Ga_2S_4$

Atom	Wyckoff site	*x*	*y*	*z*	U_{eq} (eÅ^2) [a]
			$NiGa_2S_4$		
*M**	1*b*	0	0	1/5	0.0119(9)
Ga	2*d*	1/3	2/3	0.21398(16)	0.0122(8)
S1	2*d*	1/3	2/3	0.8680(3)	0.0125(10)
S2	2*d*	1/3	2/3	0.3985(3)	0.0101(9

Table 6.2 cont.

			$Ni_{0.8}Co_{0.2}Ga_2S_4$		
*M**	1*b*	0	0	1/5	0.0083(4)
Ga	2*d*	1/3	2/3	0.21296(5)	0.0105(4)
S1	2*d*	1/3	2/3	0.86860(13)	0.0090(4)
S2	2*d*	1/3	2/3	0.39790(12)	0.0083(4)
			$Ni_{0.7}Co_{0.3}Ga_2S_4$		
*M**	1*b*	0	0	1/5	0.0088(4)
Ga	2*d*	1/3	2/3	0.21211(6)	0.0112(4)
S1	2*d*	1/3	2/3	0.86852(14)	0.0098(4)
S2	2*d*	1/3	2/3	0.39761(13)	0.0089(4)
			$Ni_{0.5}Co_{0.5}Ga_2S_4$		
*M**	1*b*	0	0	1/5	0.0083(4)
Ga1	2*d*	1/3	2/3	0.21128(6)	0.0102(4)
S1	2*d*	1/3	2/3	0.86873(16)	0.0085(5)
S2	2*d*	1/3	2/3	0.39699(15)	0.0080(5)
			$Ni_{0.9}Mn_{0.1}Ga_2S_4$		
*M**	1*b*	0	0	1/5	0.0093(4)
Ga	2*d*	1/3	2/3	0.21421(4)	0.0106(3)
S1	2*d*	1/3	2/3	0.86876(9)	0.0106(5)
S2	2*d*	1/3	2/3	0.39850(8)	0.0101(5)

*M** = $Ni_{1-x}Co_x$ for x = 0, 0.2, 0.3, 0.5 and $Ni_{0.9}Mn_{0.1}$

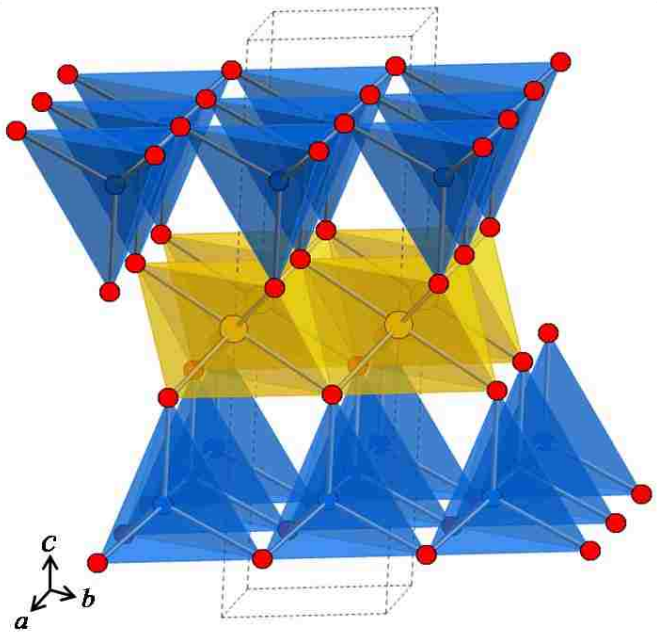

Figure A1.3 The crystal structure of $NiGa_2S_4$ showing the Ni octahedra (gold) and Ga tetrahedra (blue). Sulfur atoms are represented as red spheres.

A1.3 Structure

$Ni_{1-x}Co_xGa_2S_4$ (x = 0, 0.2, 0.3 and 0.5) and $Ni_{0.9}Mn_{0.1}Ga_2S_4$ crystallize in the $FeGa_2S_4$ structure type in the trigonal space group $P\bar{3}m1$ (No. 164).[12] Figure A1.3 shows the structure of $NiGa_2S_4$ which is a two dimensional layered compound and consists of hexagonal close-packed sulfur atoms.[14] The arrangement of the sulfur anions in the structure creates octahedra and tetrahedra holes.[14] These holes are occupied by Ni and Ga cations, respectively. X-rays cannot distinguish between Ni and Co because they are one electron apart. However, it is reasonable to model Co occupying the 1*b* site with Ni based on bond distances. Table A1.3 shows selected bond distances of *M*-S2 (*M* = $Ni_{1-x}Co_x$ for x = 0, 0.2, 0.3 and 0.5). Since Ni and Co share the same site one would expect an increase in the size of the octahedra in the unit cell. For Co^{2+} high spin (S = 3/2) in an octahedral environment, the ionic radius is 0.745 Å.[15] Ni^{2+} in the same environment has an ionic radius of 0.690 Å.[15] Thus an increase in *M*-S2 bond distances (Table A1.3) as *x* increases is consistent with Co and Ni sharing the same site. Also an increase in the size of the octahedra results in an increase in lattice parameters and cell volume as observed from the single crystal X-ray results (Table A1.1). The size of the octahedra in $Ni_{0.9}Mn_{0.1}Ga_2S_4$ can also be used to justify the substituting of Mn in the 1*b* site. An increase in *M*-S2 distance from the parent compound $NiGa_2S_4$ upon the addition of low concentrations of Mn (Table A1.3) is observed, consistent with the ionic radius of HS Mn^{2+} with CN = 6 (0.830 Å).[15] Photoemission studies on $Ni_{0.9}Mn_{0.1}Ga_2S_4$ confirm Mn is in the +2 state. In order for the compound to charge balance Mn must occupy the same site with Ni^{2+}.

Table A1.3 Selected Interatomic Distances (Å) for $Ni_{1-x}Co_xGa_2S_4$ (x = 0, 0.2, 0.3, 0.5) and $Ni_{0.9}Mn_{0.1}Ga_2S_4$

	$NiGa_2S_4$	**$Ni_{0.8}Co_{0.2}Ga_2S_4$**	**$Ni_{0.7}Co_{0.3}Ga_2S_4$**	**$Ni_{0.5}Co_{0.5}Ga_2S_4$**	**$Ni_{0.9}Mn_{0.1}Ga_2S_4$**
Ni octahedra					
*M**-S2 (x 6)	2.422(2)	2.4287(8)	2.4317(8)	2.4380(9)	2.4262(11)
Ga tetrahedra					
Ga2-S1 (x 3)	2.3138(19)	2.3142(8)	2.3107(8)	2.3101(9)	2.3223(12)
Ga2- S2	2.214(4)	2.2192(17)	2.2266(17)	2.2303(19)	2.2139(14)

*M** = x = 0, 0.2, 0.3, 0.5 for $Ni_{1-x}Co_x$; and $Ni_{0.9}Mn_{0.1}$

A1.4 References

(1) Anderson, P. W., *Mater. Res. Bull.* **1973,** *8*, 153-160.

(2) Ishida, K.; Morishita, M.; Yawata, K.; Fukuyama, H., *Phys. Rev. Lett.* **1997,** *79*, 3451.

(3) Nema, H.; Yamaguchi, A.; Hayakawa, T.; Ishimoto, H., *Phys. Rev. Lett.* **2009,** *102*, 075301-4.

(4) Ramirez, A. P.; Espinosa, G. P.; Cooper, A. S., *Phys. Rev. Lett.* **1990,** *64*, 2070.

(5) Coldea, R.; Tennant, D. A.; Tsvelik, A. M.; Tylczynski, Z., *Phys. Rev. Lett.* **2001,** *86*, 1335.

(6) Nakatsuji, S.; Nambu, Y.; Tonomura, H.; Sakai, O.; Jonas, S.; Broholm, C.; Tsunetsugu, H.; Qiu, Y.; Maeno, Y., *Science* **2005,** *309*, 1697-1700.

(7) Shimizu, Y.; Miyagawa, K.; Kanoda, K.; Maesato, M.; Saito, G., *Phys. Rev. Lett.* **2003,** *91*, 107001.

(8) Lutz, H. D.; Buchmeier, W.; Siwert, H., *Z. Anorg. Allg. Chem.* **1986,** *533*, 118-24.

(9) Nakatsuji, S.; Tonomura, H.; Onuma, K.; Nambu, Y.; Sakai, O.; Maeno, Y.; Macaluso, R. T.; Chan, J. Y., *Phys. Rev. Lett.* **2007,** *99*, 157203-4.

(10) Nambu, Y.; Nakatsuji, S.; Maeno, Y., *J. Magn. Magn. Mater.* **2007,** *310*, 1316-1318.

(11) Nambu, Y.; Nakatsuji, S.; Maeno, Y.; Okudzeto, E. K.; Chan, J. Y., *Phys. Rev. Lett.* **2008,** *101*, 207204-4.

(12) Dogguysmiri, L.; Dung, N. H.; Pardo, M. P., *Mater. Res. Bull.* **1980,** *15*, 861-866.

(13) Sheldrick, G. M. *SHELXL-97, Program for Refinement of Crystal Structures*, University of Göttingen: Göttingen, Germany, **1997**.

(14) Haeuseler, H.; Stork, H. J.; Cordes, W., *J. Solid State Chem.* **1990,** *87*, 15-19.

(15) Shannon, R. D., *Acta Cryst* **1976,** *A32*, 751-67.

APPENDIX 2 LETTERS OF PERMISSION FOR COPYRIGHTED MATERIAL

Title: CRYSTAL GROWTH AND THE SEARCH FOR HIGHLY CORRELATED INTERMETALLICS

Author: Evan Lyle Thomas, Jasmine N. Millican, Edem K. Okudzeto et al.

Publication: Comments on Inorganic Chemistry

Publisher: Taylor & Francis

Date: Jan 8, 2006

Copyright © 2006 Taylor & Francis

Logged in as:
Edem Okudzeto
Account #:
3000180849

LOGOUT

Thesis/Dissertation Reuse Request

Taylor & Francis is pleased to offer reuses of its content for a thesis or dissertation free of charge contingent on resubmission of permission request if work is published.

BACK CLOSE WINDOW

ELSEVIER LICENSE
TERMS AND CONDITIONS

May 26, 2009

This is a License Agreement between Edem K Okudzeto ("You") and Elsevier ("Elsevier") provided by Copyright Clearance Center ("CCC"). The license consists of your order details, the terms and conditions provided by Elsevier, and the payment terms and conditions.

All payments must be made in full to CCC. For payment instructions, please see information listed at the bottom of this form.

Supplier	Elsevier Limited The Boulevard,Langford Lane Kidlington,Oxford,OX5 1GB,UK
Registered Company Number	1982084
Customer name	Edem K Okudzeto
Customer address	Department of Chemistry Baton Rouge, LA 70803
License Number	2196640287779
License date	May 26, 2009
Licensed content publisher	Elsevier
Licensed content publication	Physica B: Condensed Matter
Licensed content title	Magnetic properties of the single crystal stannides $Ln_7Co_6Sn_{23}$ (Ln=Dy, Ho) and $Ln_5Co_6Sn_{18}$ (Ln=Er, Tm)
Licensed content author	Edem K. Okudzeto, Evan L. Thomas, Monica Moldovan, David P. Young and Julia Y. Chan
Licensed content date	1 April 2008
Volume number	
Issue number	
Pages	0
Type of Use	Thesis / Dissertation
Portion	Full article
Format	Both print and electronic
You are an author of the Elsevier article	Yes
Are you translating?	No
Order Reference Number	

Expected publication date	Jul 2009
Elsevier VAT number	GB 494 6272 12
Permissions price	0.00 USD
Value added tax 0.0%	0.00 USD
Total	0.00 USD

Terms and Conditions

INTRODUCTION

1. The publisher for this copyrighted material is Elsevier. By clicking "accept" in connection with completing this licensing transaction, you agree that the following terms and conditions apply to this transaction (along with the Billing and Payment terms and conditions established by Copyright Clearance Center, Inc. ("CCC"), at the time that you opened your Rightslink account and that are available at any time at http://myaccount.copyright.com).

GENERAL TERMS

2. Elsevier hereby grants you permission to reproduce the aforementioned material subject to the terms and conditions indicated.

3. Acknowledgement: If any part of the material to be used (for example, figures) has appeared in our publication with credit or acknowledgement to another source, permission must also be sought from that source. If such permission is not obtained then that material may not be included in your publication/copies. Suitable acknowledgement to the source must be made, either as a footnote or in a reference list at the end of your publication, as follows:

"Reprinted from Publication title, Vol /edition number, Author(s), Title of article / title of chapter, Pages No., Copyright (Year), with permission from Elsevier [OR APPLICABLE SOCIETY COPYRIGHT OWNER]." Also Lancet special credit - "Reprinted from The Lancet, Vol. number, Author(s), Title of article, Pages No., Copyright (Year), with permission from Elsevier."

4. Reproduction of this material is confined to the purpose and/or media for which permission is hereby given.

5. Altering/Modifying Material: Not Permitted. However figures and illustrations may be altered/adapted minimally to serve your work. Any other abbreviations, additions, deletions and/or any other alterations shall be made only with prior written authorization of Elsevier Ltd. (Please contact Elsevier at permissions@elsevier.com)

6. If the permission fee for the requested use of our material is waived in this instance, please be advised that your future requests for Elsevier materials may attract a fee.

7. Reservation of Rights: Publisher reserves all rights not specifically granted in the combination of (i) the license details provided by you and accepted in the course of this licensing transaction, (ii) these terms and conditions and (iii) CCC's Billing and Payment terms and conditions.

8. License Contingent Upon Payment: While you may exercise the rights licensed

immediately upon issuance of the license at the end of the licensing process for the transaction, provided that you have disclosed complete and accurate details of your proposed use, no license is finally effective unless and until full payment is received from you (either by publisher or by CCC) as provided in CCC's Billing and Payment terms and conditions. If full payment is not received on a timely basis, then any license preliminarily granted shall be deemed automatically revoked and shall be void as if never granted. Further, in the event that you breach any of these terms and conditions or any of CCC's Billing and Payment terms and conditions, the license is automatically revoked and shall be void as if never granted. Use of materials as described in a revoked license, as well as any use of the materials beyond the scope of an unrevoked license, may constitute copyright infringement and publisher reserves the right to take any and all action to protect its copyright in the materials.

9. Warranties: Publisher makes no representations or warranties with respect to the licensed material.

10. Indemnity: You hereby indemnify and agree to hold harmless publisher and CCC, and their respective officers, directors, employees and agents, from and against any and all claims arising out of your use of the licensed material other than as specifically authorized pursuant to this license.

11. No Transfer of License: This license is personal to you and may not be sublicensed, assigned, or transferred by you to any other person without publisher's written permission.

12. No Amendment Except in Writing: This license may not be amended except in a writing signed by both parties (or, in the case of publisher, by CCC on publisher's behalf).

13. Objection to Contrary Terms: Publisher hereby objects to any terms contained in any purchase order, acknowledgment, check endorsement or other writing prepared by you, which terms are inconsistent with these terms and conditions or CCC's Billing and Payment terms and conditions. These terms and conditions, together with CCC's Billing and Payment terms and conditions (which are incorporated herein), comprise the entire agreement between you and publisher (and CCC) concerning this licensing transaction. In the event of any conflict between your obligations established by these terms and conditions and those established by CCC's Billing and Payment terms and conditions, these terms and conditions shall control.

14. Revocation: Elsevier or Copyright Clearance Center may deny the permissions described in this License at their sole discretion, for any reason or no reason, with a full refund payable to you. Notice of such denial will be made using the contact information provided by you. Failure to receive such notice will not alter or invalidate the denial. In no event will Elsevier or Copyright Clearance Center be responsible or liable for any costs, expenses or damage incurred by you as a result of a denial of your permission request, other than a refund of the amount(s) paid by you to Elsevier and/or Copyright Clearance Center for denied permissions.

LIMITED LICENSE

The following terms and conditions apply to specific license types:

15. **Translation**: This permission is granted for non-exclusive world **English** rights only unless your license was granted for translation rights. If you licensed translation rights you may only translate this content into the languages you requested. A professional translator must perform all translations and reproduce the content word for word preserving the integrity of the article. If this license is to re-use 1 or 2 figures then permission is granted

for non-exclusive world rights in all languages.

16. **Website**: The following terms and conditions apply to electronic reserve and author websites:
Electronic reserve: If licensed material is to be posted to website, the web site is to be password-protected and made available only to bona fide students registered on a relevant course if:
This license was made in connection with a course,
This permission is granted for 1 year only. You may obtain a license for future website posting,
All content posted to the web site must maintain the copyright information line on the bottom of each image,
A hyper-text must be included to the Homepage of the journal from which you are licensing at http://www.sciencedirect.com/science/journal/xxxxx or, for books, to the Elsevier homepage at http://www.elsevier.com,
Central Storage: This license does not include permission for a scanned version of the material to be stored in a central repository such as that provided by Heron/XanEdu.

17. **Author website** for journals with the following additional clauses:

All content posted to the web site must maintain the copyright information line on the bottom of each image, and
The permission granted is limited to the personal version of your paper. You are not allowed to download and post the published electronic version of your article (whether PDF or HTML, proof or final version), nor may you scan the printed edition to create an electronic version,
A hyper-text must be included to the Homepage of the journal from which you are licensing at http://www.sciencedirect.com/science/journal/xxxxx,
Central Storage: This license does not include permission for a scanned version of the material to be stored in a central repository such as that provided by Heron/XanEdu.

18. **Author website** for books with the following additional clauses:
Authors are permitted to place a brief summary of their work online only.
A hyper-text must be included to the Elsevier homepage at http://www.elsevier.com.
All content posted to the web site must maintain the copyright information line on the bottom of each image
You are not allowed to download and post the published electronic version of your chapter, nor may you scan the printed edition to create an electronic version.
Central Storage: This license does not include permission for a scanned version of the material to be stored in a central repository such as that provided by Heron/XanEdu.

19. **Website** (regular and for author): A hyper-text must be included to the Homepage of the journal from which you are licensing at
http://www.sciencedirect.com/science/journal/xxxxx or, for books, to the Elsevier homepage at http://www.elsevier.com.

20. **Thesis/Dissertation**: If your license is for use in a thesis/dissertation your thesis may be submitted to your institution in either print or electronic form. Should your thesis be published commercially, please reapply for permission. These requirements include permission for the Library and Archives of Canada to supply single copies, on demand, of the complete thesis and include permission for UMI to supply single copies, on demand, of the complete thesis. Should your thesis be published commercially, please reapply for permission.

21. **Other conditions:** None

v1.5

Gratis licenses (referencing $0 in the Total field) are free. Please retain this printable license for your reference. No payment is required.

If you would like to pay for this license now, please remit this license along with your payment made payable to "COPYRIGHT CLEARANCE CENTER" otherwise you will be invoiced within 30 days of the license date. Payment should be in the form of a check or money order referencing your account number and this license number 2196640287779.
If you would prefer to pay for this license by credit card, please go to http://www.copyright.com/creditcard to download our credit card payment authorization form.

Make Payment To:
Copyright Clearance Center
Dept 001
P.O. Box 843006
Boston, MA 02284-3006

If you find copyrighted material related to this license will not be used and wish to cancel, please contact us referencing this license number 2196640287779 and noting the reason for cancellation.

Questions? customercare@copyright.com or +1-877-622-5543 (toll free in the US) or +1-978-646-2777.

ACS Publications High quality. High impact.

Title: Crystal Growth, Transport, and Magnetic Properties of YbCoGa5
Author: Edem K. Okudzeto et al.
Publication: Crystal Growth and Design
Publisher: American Chemical Society
Date: Apr 1, 2009

Order Completed

Thank you very much for your order.

This is a License Agreement between Edem K Okudzeto ("You") and American Chemical Society ("American Chemical Society"). The license consists of your order details, the terms and conditions provided by American Chemical Society, and the payment terms and conditions.

Get the printable license.

License Number	2239070384232
License date	Jul 30, 2009
Licensed content publisher	American Chemical Society
Licensed content publication	Crystal Growth and Design
Licensed content title	Crystal Growth, Transport, and Magnetic Properties of YbCoGa5
Licensed content author	Edem K. Okudzeto et al.
Licensed content date	Apr 1, 2009
Volume number	9
Issue number	4
Type of Use	Thesis/Dissertation
Are you the Author of original article?	Yes
Format	Print
Portion	Full article
Order reference number	
Title of the thesis / dissertation	Exploration of Ternary Intermetallic Materials Using Tin and Gallium Flux
Expected completion date	Dec 2009
Estimated size(pages)	114
Billing type	Invoice
Billing address	Department of Chemistry
	Louisiana State University
	Baton Rouge, LA 70803
	United States
Customer reference info	
Permissions price	0.00 USD

ORDER MORE... CLOSE WINDOW

VITA

Edem Kodzo Doe Okudzeto was born in November, 1978, in Accra, Ghana, to Sam and Pricilla Okudzeto. He has five older siblings Agnes Okudzeto-Ayekpa, Sena Okyere, Samuel Kwaku Okudzeto Jr, Eline Okudzeto-Nketia and Esine Okudzeto. He graduated from Akosombo International School in December 1997. Edem attended Morehouse College in Atlanta, Georgia, in the fall of 2000. While at Morehouse Edem was a member of various student organizations, where he held various leadership positions. He received a Bachelor of Science Degree in chemistry from Morehouse College on May 15, 2004.

In the fall of 2004, Edem began his graduate career at Louisiana State University, under the tutelage of Dr. Julia Y. Chan. While at Louisiana State University he attended and presented posters at several scientific meetings: the 62th Southwest Regional Meeting of the American Chemical Society in Houston, Texas (2006), the International Conference on Strongly Correlated Electron Systems in Houston, Texas (2007), the 235th ACS National Meeting & Exposition in New Orleans, Louisiana (2008), and the 25th Rare Earth Research Conference in Tuscaloosa, Alabama (2008). Edem received the Strongly Correlated Electron Systems Conference Young Investigator Award in 2007 and a Graduate student travel award in 2008. He served on the Chemistry Graduate Student Council (2005-2006) and was a Parliamentarian for the LSU chapter of NOBCChE (2007-2008). Edem also participated in the department's service learning program by performing chemistry demonstration for students in local schools.

Edem will graduate from Louisiana State University on December, 2009, with a Doctor of Philosophy degree in chemistry. He plans on attending law school after graduation.